

# LLE Review



## Quarterly Report



## About the Cover:

Holographic transmission gratings, like those shown on the front cover, have been used to control and diagnose the effective coherence of solid-state lasers at LLE for over a decade. Terrance Kessler, senior research engineer and group leader of Optics and Imaging Sciences at LLE, is shown demonstrating the spectral dispersion of one of the many holographic diffraction gratings used on the OMEGA laser system.



The holographic interferometer, shown in the photograph, is situated within a room only slightly larger than the 8-ft  $\times$  16-ft  $\times$  2-ft optical table on which it is located. The holographic recording plane, positioned at the center of the photo (cross on white disk), intercepts the two beams of the holographic interferometer and exposes the photosensitive polymers coated over a glass plate that has a diameter between 10 and 20 cm. Submicron grooves that are shaped are then formed over these glass plates. A smaller interferometer, positioned to the left in the photograph, is used for environmental sensing to establish the time periods over which gratings can be made to have spatially uniform diffraction efficiencies approaching unity.

This report was prepared as an account of work conducted by the Laboratory for Laser Energetics and sponsored by New York State Energy Research and Development Authority, the University of Rochester, the U.S. Department of Energy, and other agencies. Neither the above named sponsors, nor any of their employees, makes any warranty, expressed or implied, or assumes any legal liability or responsibility for the accuracy, completeness, or usefulness of any information, apparatus, product, or process disclosed, or represents that its use would not infringe privately owned rights. Reference herein to any specific commercial product, process, or service by trade name, mark, manufacturer, or otherwise, does not necessarily constitute or imply its endorsement, recommendation, or favoring by

the United States Government or any agency thereof or any other sponsor. Results reported in the LLE Review should not be taken as necessarily final results as they represent active research. The views and opinions of authors expressed herein do not necessarily state or reflect those of any of the above sponsoring entities.

The work described in this volume includes current research at the Laboratory for Laser Energetics, which is supported by New York State Energy Research and Development Authority, the University of Rochester, the U.S. Department of Energy Office of Inertial Confinement Fusion under Cooperative Agreement No. DE-FC03-92SF19460, and other agencies.

Printed in the United States of America  
Available from  
National Technical Information Services  
U.S. Department of Commerce  
5285 Port Royal Road  
Springfield, VA 22161

Price codes: Printed Copy A04  
Microfiche A01

For questions or comments, contact P. B. Radha, *Editor*,  
Laboratory for Laser Energetics, 250 East River Road,  
Rochester, NY 14623-1299, (716) 275-1453.

Worldwide-Web Home Page: <http://www.lle.rochester.edu/>

# LLE Review

## Quarterly Report



### Contents

In Brief .....	iii
OMEGA Cryogenic Target Designs.....	49
Imprint Reduction Using an Intensity Spike in OMEGA Cryogenic Targets .....	56
Measurement of Preheat due to Fast Electrons in Laser Implosions .....	63
Holographic Transmission Gratings for Spectral Dispersion .....	71
Laser Beam Smoothing Caused by the Small-Spatial-Scale <i>B</i> -Integral .....	78
Three-Dimensional Modeling of Capsule Implosions in OMEGA Tetrahedral Hohlraums .....	90
Nanoindentation Hardness of Particles Used in Magnetorheological Finishing (MRF).....	107
Publications and Conference Presentations	



## In Brief

This volume of the LLE Review, covering the period January–March 2000, includes a report on OMEGA cryogenic target designs for the soon-to-be-commissioned OMEGA Cryogenic Target Handling System. R. P. J. Town, J. A. Delettrez, R. Epstein, V. N. Goncharov, P. W. McKenty, P. B. Radha, and S. Skupsky use two-dimensional hydrodynamic simulations in conjunction with a stability analysis model to study the performance of OMEGA cryogenic capsules. They show that these targets are energy-scaled from the NIF ignition designs and have similar 1-D behavior and stability properties. This similarity will facilitate the extrapolation of cryogenic target studies on OMEGA to ignition targets on the NIF.

Additional research highlights reported in this issue are

- T. J. B. Collins and S. Skupsky describe the physics of a novel technique for laser-imprint reduction in OMEGA cryogenic capsules. Laser nonuniformities can imprint the target with a “seed” that can cause debilitating hydrodynamic instabilities. In their article, the authors show, using the two-dimensional hydrodynamics code *ORCHID*, that an initial spike in the laser pulse can reduce laser imprint by about a factor of 2 for typical target configurations and especially for the nonuniformity modes considered most dangerous for target performance. Further, they show that this modification to the laser pulse need not significantly degrade target performance and is accompanied by only a modest decrease in the one-dimensional neutron yield.
- Through a judicious choice of materials and target dimensions, B. Yaakobi, C. Stoeckl, T. R. Boehly, D. D. Meyerhofer, and W. Seka have experimentally inferred fast-electron preheat due to laser irradiation on OMEGA. Significant fast-electron preheat can substantially decrease the effectiveness of a direct-drive implosion. In this article, the authors report on their experiment in planar geometry. The results from this measurement will be used as a reference point to determine fast-electron preheat in ignition-relevant direct-drive spherical targets.
- T. J. Kessler, J. Barone, C. Kellogg, and H. Huang present results from their ongoing experimental and theoretical work relating to holographic grating design and fabrication. These high-diffraction-efficiency and high-wavefront-quality gratings are used on the OMEGA laser primarily for laser-beam smoothing and spectroscopy. The authors report that for the high-optical-quality gratings required on OMEGA, it is critical to control environmental factors including humidity, thermal gradients, and air turbulence during grating fabrication. Future work will involve improved modeling of these gratings and further experimental investigations.
- Experimental measurements of target irradiation nonuniformity in the absence of smoothing by spectral dispersion (SSD) have indicated lower-than-expected levels of nonuniformity. Shots without SSD are base-line measurements for OMEGA, and consequently modeling these shots provides for a more complete understanding of the target irradiation nonuniformity. In this article, J. A. Marozas, S. P. Regan, J. H. Kelly, D. D. Meyerhofer, W. Seka, and S. Skupsky compare numerical simulations of laser smoothing with these measurements. They identify intensity-dependent phase accumulations by the OMEGA laser (*B*-integral) as the mechanism for this observed smoothing. The authors conclude that they can successfully model these *B*-integral-related smoothing mechanisms and find them to be relatively minor compared to the dominant smoothing effect of SSD.

- J. D. Schnittman and R. S. Craxton describe their simulations of capsule implosions in tetrahedral hohlraum experiments carried out on OMEGA in a collaboration between LLE and Los Alamos National Laboratory. These hohlraums are particularly well suited to the OMEGA target chamber geometry and have been shown to provide an extremely uniform radiation drive. The authors use a three-dimensional (3-D) view-factor code with time-dependent radiation transport both in the hohlraum wall and as a perturbation on a spherically symmetric hydrodynamic implosion of the capsule. They also simulate x-ray images of the imploded core with a 3-D x-ray postprocessor and find close agreement with experiment on several quantities including radiation drive temperatures, fusion yields, and core deformation.
- Knowledge of the hardness of abrasive particles is a key to understanding the mechanisms of material removal in polishing of optical glass. A. B. Shorey, K. M. Kwong, K. M. Johnson, and S. D. Jacobs report on measurements of the nanohardness of magnetic and nonmagnetic particles used in the magnetorheological finishing (MRF) process. Their nanoindentation technique allows for the characterization of mechanical properties of small abrasive particles that is not possible through traditional microhardness measurement methods. With abrasive particle characterization now possible, subsequent experiments with different combinations of abrasive particles can provide information regarding removal mechanisms in MRF.

P. B. Radha  
*Editor*

## OMEGA Cryogenic Target Designs

The achievement of high-density implosions using ignition-relevant pulse shapes and cryogenic targets on OMEGA is an important milestone on the path to attaining direct-drive ignition at the National Ignition Facility (NIF). The OMEGA Cryogenic Target Handling System is undergoing final tests and will soon be commissioned for  $D_2$  implosion experiments. Cryogenic targets have also been designed for this system with the primary criterion of being *hydrodynamically equivalent* to the ignition capsule designs. In this context, the constraints placed on OMEGA cryogenic target designs include similar peak shell velocities, hot-spot convergence, in-flight aspect ratio, and stability properties as the NIF designs. NIF designs have been discussed previously in Ref 1. In this article, we report on the cryogenic OMEGA target design and compare its physical behavior with the  $\alpha = 3$  ignition NIF design.

The basis for the OMEGA designs is the NIF direct-drive  $\alpha = 3$  ignition design, which consists of a 340- $\mu\text{m}$  DT-ice layer encased in a thin ( $<3\text{-}\mu\text{m}$ ) plastic capsule of 1.69-mm outer radius. One-dimensional hydrodynamic scaling arguments<sup>2</sup> can then be used to guide the design of OMEGA cryogenic targets. The laser energy ( $E$ ) required to contribute to a given plasma thermal energy scales roughly as the radius of the capsule ( $R$ ) according to  $E \sim R^3$ . The NIF is designed to provide

1.5 MJ of energy; OMEGA is capable of delivering 30 kJ. Thus, the radius of an OMEGA capsule will be approximately 0.3 times the NIF design (see Fig. 82.1).

Figure 82.2 shows the power history for the NIF and OMEGA pulses. The NIF laser pulse irradiating the ignition design is a 9.25-ns shaped pulse consisting of a 10-TW, 4.25-ns foot rising to a 450-TW pulse for 2.5 ns. The corresponding laser pulse for the OMEGA design is determined by noting that the time ( $t$ ) or duration of the laser pulse scales as the confinement time and is roughly proportional to the radius of the target; therefore<sup>2</sup>  $t \sim R$ . The scaling of the peak power ( $P$ ) in the laser pulse can be obtained from the energy and time scaling; therefore,<sup>2</sup>  $P \sim R^2$ . Consequently, the length of the laser pulse shrinks from 9.25 ns in the  $\alpha = 3$  ignition target design to 2.5 ns for the OMEGA cryogenic target design. The peak power using  $P \sim R^2$  then scales to 32 TW. Processes other than hydrodynamics, such as radiation, thermal transport, and thermonuclear burn, do not scale in a simple manner between the ignition designs and the OMEGA cryogenic designs. We will show, however, that these energy-scaled targets possess similar 1-D behavior and instability growth as the ignition designs, thus meeting the requirement of hydrodynamic equivalence.

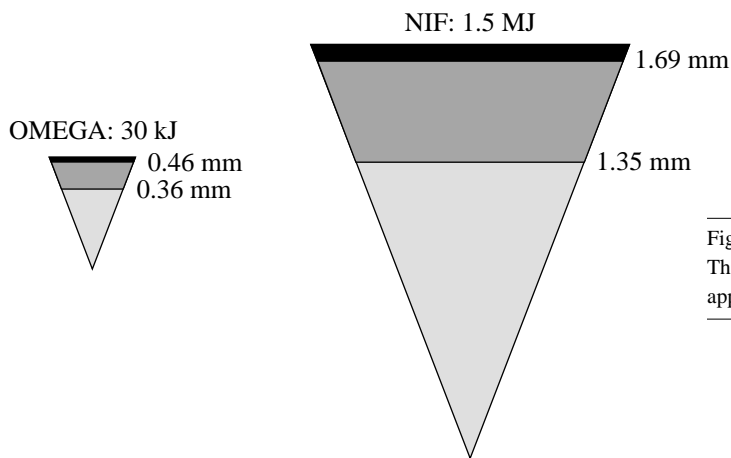


Figure 82.1  
The NIF and OMEGA capsule designs. The radius of the OMEGA design is approximately 0.3 times that of the NIF design.

TCS126

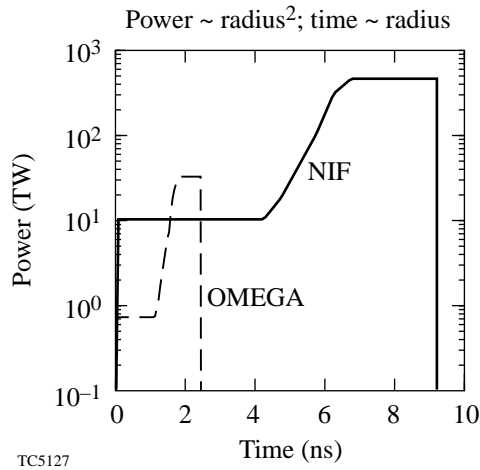


Figure 82.2  
The NIF and OMEGA pulse shapes.

The timing of *two* shocks is critical to determining the overall performance of the direct-drive ignition target design. The two distinct shocks in this design are launched into the target at the start of the laser pulse and during its rise to the main drive intensity. The position of the shocks in the target can be calculated from the radial logarithmic derivative of the pressure. Figure 82.3 is a contour map of this quantity [ $d(\ln P)/dr$ ] as a function of the Lagrangian coordinate and time for the ignition and the OMEGA design. Time has been normalized to the incident laser energy, with  $t = 1.0$  corresponding to the end of the laser pulse. This normalization will allow us to compare the two designs at the same stage of the implosion. The darker, more-intense regions represent a larger gradient in pressure and thus capture the position of the shocks. The OMEGA design shows similar shock-timing behavior as that of the ignition design for the first shock. The second shock, however, arrives slightly later in the OMEGA design than in the ignition design in normalized time units. This is a consequence of lower laser-energy absorption in the OMEGA design. Absorption in direct-drive designs is primarily via inverse bremsstrahlung, which depends on the density scale length. The NIF designs typically have scale lengths that are 2 to 3 times longer than OMEGA, which leads to an absorption fraction for the ignition design of 60% on the NIF and 40% on OMEGA.

At the time the first shock breaks out of the rear of the ice surface, a rarefaction wave travels back through the ice layer in the outward direction. This rarefaction wave results in a decreasing density gradient in the inward radial direction. The second shock, which is caused by the rise of the main pulse, then travels through this decreasing density gradient. This

serves to increase the adiabat ( $\alpha$ ) of the ice layer. Since the second shock in the OMEGA design arrives later (in normalized time units) than in the NIF design, the rear ice surface decompresses more than in the ignition design. Consequently, the OMEGA design has a slightly higher adiabat ( $\alpha = 3.2$ ) than the ignition design ( $\alpha = 3$ ).

The adiabat of the implosion is defined as the ratio of the pressure of the cold fuel to the Fermi degenerate pressure and is an important figure of merit for the overall performance of target designs. Lower adiabat implosions have higher one-dimensional performance since less laser energy is needed to

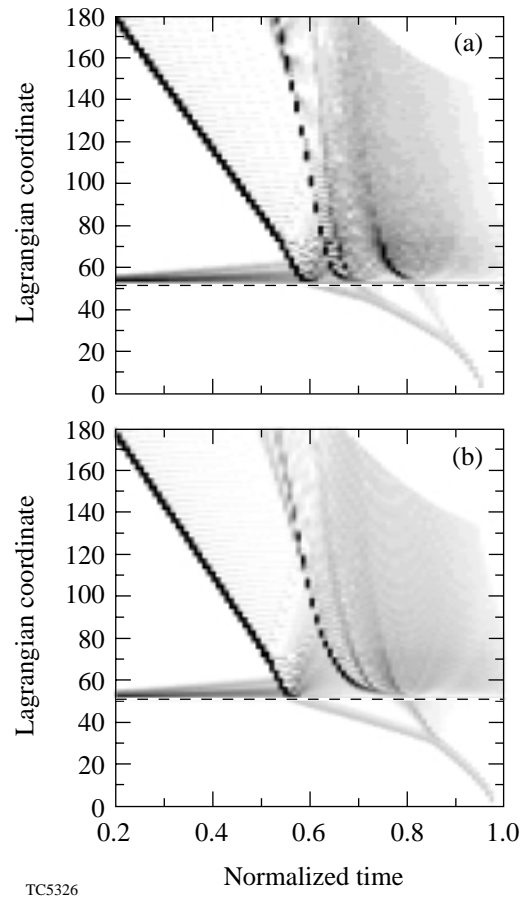
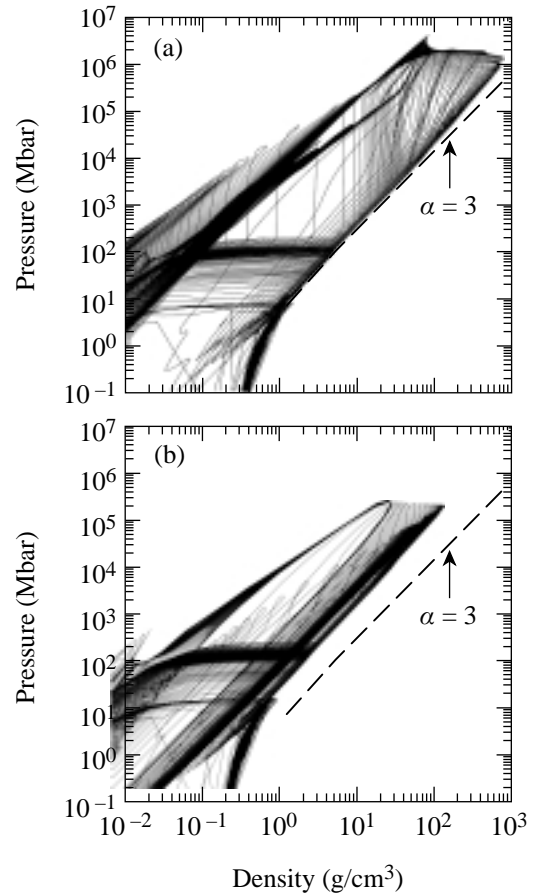


Figure 82.3  
Shock propagation as shown by a contour map of the logarithmic derivative of the pressure as a function of normalized time and Lagrangian coordinate for (a) the NIF and (b) the OMEGA designs. Time has been normalized to the incident laser energy, with  $t = 1.0$  corresponding to the end of the laser pulse. This allows the two designs to be compared at the same stage of the implosion. The darker shading indicates a larger pressure gradient and thus captures the position of the shocks. The OMEGA design shows similar timing for the first shock but a delayed second shock compared to the NIF design.

compress a cold fuel than a warm fuel. The ablation velocity, however, depends directly on the adiabat ( $\sim\alpha^{3/5}$ ); thus, the Rayleigh–Taylor (RT) growth rates decrease with the adiabat. Higher adiabat implosions, therefore, are more stable to the acceleration-phase RT instability. To ensure similar performance between the NIF and OMEGA cryogenic capsules, the cold fuel layer should have similar adiabats. Plotting the pressure-density trajectory of the Lagrangian cells used in the simulation will show the adiabatic history of target designs. Figure 82.4 is such a plot for both the NIF design and the OMEGA design; also shown is the  $\alpha=3$  adiabat line (dashed). The NIF design obviously accesses a larger portion of phase space than the OMEGA design. Only the extremely compressed and high-density region is inaccessible by the OMEGA design. Table 82.I, which lists other key one-dimensional parameters, indicates that the OMEGA and NIF designs have similar peak shell velocities, hot-spot convergence ratios, and in-flight aspect ratios. To compare an igniting and non-igniting target, we have defined the hot spot as the ratio of the initial outer radius to the radius that contains 90% of the yield at the time of peak neutron production when propagating burn has been switched off.

Implosion efficiency can be quantified in two ways: The *hydrodynamic efficiency* is defined as the ratio of the kinetic energy of the imploding target to the absorbed energy. The *coupling efficiency* is defined as the ratio of the kinetic energy of the imploding target to the incident energy. Although OMEGA has a similar hydrodynamic efficiency to the NIF, the reduced absorption fraction leads to a lower coupling efficiency.



TC5327

Figure 82.4 The density-pressure trajectories for each Lagrangian cell used in the simulations of (a) NIF and (b) OMEGA designs. Also shown (dashed line) is the  $\alpha=3$  adiabat line.

Table 82.I: Comparison of one-dimensional parameters between the NIF and OMEGA cryogenic target designs.

	NIF	OMEGA
Absorption fraction	60%	40%
Hydrodynamic efficiency	11.0%	11.5%
Coupling efficiency	7%	4.5%
Peak shell velocity (cm/s)	$4.0 \times 10^7$	$3.7 \times 10^7$
Hot-spot convergence ratio	28	20
In-flight aspect ratio	60	50
Peak areal density (mg/cm <sup>2</sup> )	1200	300
Neutron-averaged ion temperature (keV)	30	4
Neutron yield	$2.5 \times 10^{19}$	$1.8 \times 10^{14}$

The NIF design is expected to have different plasma physics issues compared to the OMEGA design. The density and velocity scale lengths at the tenth- and quarter-critical surfaces primarily determine the intensity threshold for plasma instabilities such as stimulated Raman scattering (SRS), stimulated Brillouin scattering (SBS), and two-plasmon decay (TPD). These instabilities in the ablating plasma can significantly influence laser absorption, the occurrence of hot electrons, and therefore the performance of the target. By comparing the actual intensity to the plasma instability thresholds, the susceptibility of the designs to plasma instabilities can be assessed. The quarter- and tenth-critical surfaces have similar intensities in both cases, which is not surprising since the laser power was scaled with the square of the radius of the pellet; the peak intensity as a result of overlapped beams at the quarter-critical surface is  $1.0 \times 10^{15} \text{ W/cm}^2$  and  $6.0 \times 10^{14} \text{ W/cm}^2$  at the tenth-critical surface for both designs. For the NIF the total overlapped intensity is well above the SBS threshold after about 6 ns; while the single-cluster intensity is comparable to the threshold. The intensity is always below the SRS threshold. As mentioned, OMEGA has shorter scale lengths than the NIF designs. During the rise to the peak of the laser pulse the scale length at the tenth-critical surface in the NIF design rapidly increases to approximately  $800 \mu\text{m}^{-1}$  and is typically three times larger than the OMEGA design. Therefore, we would expect the OMEGA design to be less susceptible to SRS and SBS than the NIF design. However, both designs are well above threshold for the TPD instability. The NIF design also has a larger volume than OMEGA for the nonlinearly saturated state of the TPD instability to generate hot electrons. Separate experiments have been conducted at LLE to study these plasma physics issues. In these experiments, NIF-scale-length plasmas have been generated using a laser pulse similar in intensity to the NIF pulse. Results to date<sup>3</sup> of the high-intensity drive portion of the NIF pulse show little evidence of SRS, suggesting that this instability will have an insignificant effect on the performance of the ignition design.

Hydrodynamic instabilities are the second source of deviations from one-dimensional hydrodynamic simulations. The RT instability can degrade target performance by breaking the spherical symmetry of the implosion. The RT instability occurs twice during the implosion: at the outer ablation surface as the shell accelerates inward and at the hot spot–main fuel layer interface as the capsule decelerates at the end of the implosion. Four sources of nonuniformity primarily seed the RT instability: (1) laser imprinting, (2) outside capsule finish, (3) drive asymmetry, and (4) inner-DT-ice roughness. An important component of the OMEGA campaign will be to experimentally

determine the maximum allowable levels of these sources of nonuniformities for the NIF laser and direct-drive ignition targets. OMEGA cryogenic targets must, therefore, have similar stability properties to the NIF designs to ensure that the extrapolation of these results to NIF targets will be valid.

Imprint levels are expected to be smaller on OMEGA than on the NIF. The level of laser imprint in both the NIF and OMEGA direct-drive targets can be quantified in terms of the imprint efficiency, which is defined as the ratio of the amplitude of the ablation surface nonuniformity to the percent of laser nonuniformity. We determine this quantity using two-dimensional (2-D) *ORCHID* simulations, each with a single-mode laser nonuniformity, for NIF and OMEGA designs. These *ORCHID* simulations included the following laser-smoothing techniques: (1) a phase-plate spectrum appropriate to the spot size, (2) a polarization-smoothing wedge, and (3) 2-D smoothing by spectral dispersion (SSD) at two UV bandwidths ( $0.5 \text{ THz}_{\text{UV}}$  and  $1 \text{ THz}_{\text{UV}}$ ). We find good agreement between the imprint efficiency calculated from *ORCHID* and that obtained from the analytic theory of Goncharov.<sup>4</sup> Using this analytic theory and *ORCHID* simulations, the mode spectrum due to imprint for the NIF and OMEGA designs at the start of the acceleration phase is shown in Fig. 82.5. In the NIF design, the laser has imprinted a surface nonuniformity equal to  $\sigma_{\text{rms}} = 480 \text{ \AA}$  (in modes  $\ell < 1000$ ). OMEGA has a corresponding imprinted nonuniformity of  $\sigma_{\text{rms}} = 290 \text{ \AA}$ . The cusps observed in the mode spectrum are a consequence of dynamic overpressure<sup>4</sup> that causes the imprinted mode to oscillate with a period proportional to the wavelength of the mode. The acceleration phase begins when the rarefaction wave from the rear surface reaches the ablation surface; therefore, the time

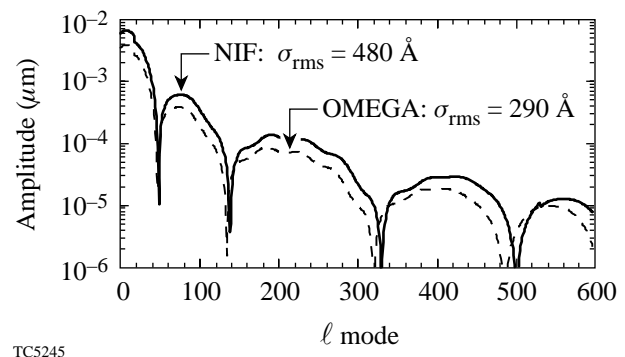


Figure 82.5

Modal spectrum of the surface amplitude due to imprint from a  $1\text{-THz}_{\text{UV}}$  2-D SSD smoothed laser for the NIF and OMEGA designs at the start of the acceleration phase.

when this phase begins is roughly proportional to the shell thickness. The cusps in the imprint spectrum will consequently occur for wavelengths that are at a minimum when the acceleration phase begins. For the NIF design, the period of oscillation is three times that of the OMEGA design; however, the acceleration phase begins approximately three times later than the OMEGA design, so the cusps occur at the same part of the  $\ell$ -mode spectrum for both designs. Scaling arguments can be invoked to determine the relation between imprint levels on OMEGA and NIF targets. Since the laser energy deposited at the critical surface is thermally conducted to the ablation surface, significant reductions in the level of imprint-induced nonuniformities can be obtained by thermal smoothing over this *stand-off* distance. Dimensional considerations suggest that imprint levels should vary as  $kD_c$  (where  $k$  is the perturbation wave number and  $D_c$  is the distance between the energy absorption region and the ablation surface). Imprint essentially ends when the laser decouples from the target, i.e., when  $kD_c \sim 1$ ; therefore, a longer wavelength should imprint less than a shorter wavelength. A given  $\ell$  mode on OMEGA has a wavelength that is approximately one-third of the same  $\ell$  mode on the NIF direct-drive target. Thus a single beam on OMEGA will imprint one-third as much as on the NIF for the same  $\ell$  mode. However, since NIF has approximately four times the number of overlapped beams, imprint for OMEGA design will be two-thirds that of the NIF design.

Next, we study the evolution of the shell during the acceleration phase of the implosion. The OMEGA designs have an overdense shell thickness that is approximately one-third the NIF-shell thickness, where the shell thickness is defined as the distance between the  $1/e$  points of the maximum density. If the two designs have the same initial seed and RT  $e$ -foldings during the acceleration phase, the OMEGA design's mix-width region will be a greater percentage of the overdense shell. Figure 82.6 shows the results of an instability post-

processor to 1-D hydrocode *LILAC* simulations. This post-processor uses a self-consistent model<sup>5</sup> to study the evolution of perturbations at the ablation front and the back surface of an accelerated spherical shell. The model includes the ablative Richtmyer–Meshkov (RM),<sup>6</sup> RT, and Bell–Plesset (BP) instabilities, and 3-D Haan saturation.<sup>7</sup> The model consists of two differential equations (describing the ablation- and inner-surface perturbations) obtained by solving the linearized conservation equations in the DT gas, the shell, and the blowoff plasma regions. The seeds for the nonuniformity processor were (1) the imprint caused by 1-THz<sub>UV</sub>, 2-D SSD; (2) an outer capsule roughness of 840 Å (in an  $\ell$ -mode spectrum taken from Weber<sup>8</sup>); and (3) an inner-ice-surface roughness of 2 μm [with a spectrum of the form  $\sigma \sim \ell^{-1.5}$  (Ref. 9)]. Figure 82.6 shows the overdense shell thickness and the mix width for the NIF and OMEGA designs. Both designs survive the acceleration phase, i.e., the mix width is less than the shell width; however, the NIF mix width is approximately 30% of the overdense shell, whereas the OMEGA design's mix width is almost 90% of the shell thickness. Thus the OMEGA design has a lower safety factor for survival through the acceleration phase than the  $\alpha = 3$  NIF design for a given level of laser and target nonuniformity.

During the implosion the outer-surface perturbation *feeds through* to the inner surface, which can then grow via the RT instability during the deceleration phase. The feedthrough for a given  $\ell$  mode scales approximately as  $kD_o$ , where  $D_o$  is the overdense shell thickness. Since the increase in shell thickness for the NIF target is compensated for by the smaller wavelength for the same  $\ell$  mode, the NIF and OMEGA designs are predicted to have similar amounts of feedthrough. Figure 82.7 shows the mode spectrum at the inner surface of the DT ice for both designs at the onset of the deceleration phase. The mode spectrum is heavily weighted toward the low  $\ell$  mode of the spectrum, with most of the power contained below  $\ell \sim 20$ . The higher level of imprint in the NIF design compared to OMEGA

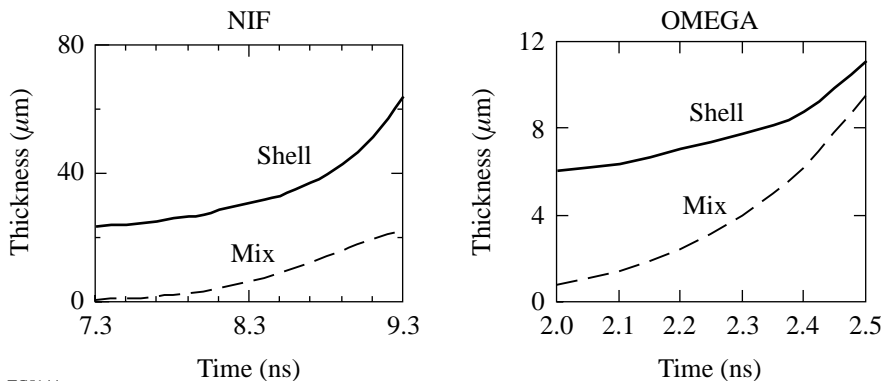
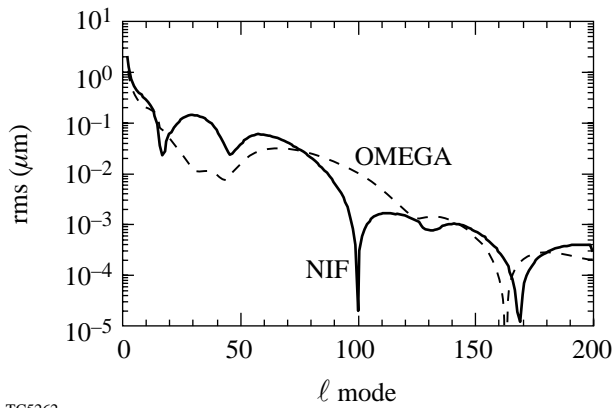


Figure 82.6 The overdense shell thickness and mix width for the NIF design and the OMEGA design during the acceleration phase. In both cases the overdense shell thickness is larger than the mix width, which implies that both designs will survive the acceleration phase.

TC5144

has led to a higher amount of feedthrough in the range at which imprint dominates ( $10 < \ell < 100$ ). For low  $\ell$  modes ( $\ell < 10$ ), where the effect of the inner ice surface is dominant, the mode amplitudes are comparable in both cases. The instability postprocessor cannot self-consistently determine the degradation in target yield for a given initial nonuniformity level. We therefore use a limited number of *ORCHID* simulations to determine the effect of these levels of inner-ice distortions at the start of the deceleration phase (predicted by the instability postprocessor) on the overall target performance.



TC5262

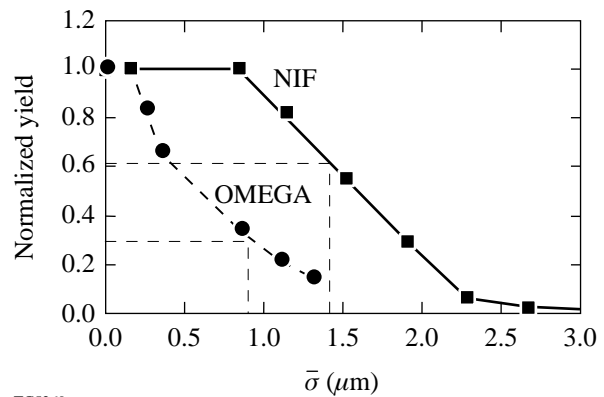
Figure 82.7  
The mode spectrum of the NIF (solid line) and OMEGA (dashed line) designs at the onset of the deceleration phase.

The *ORCHID* simulations are initialized at the start of the laser pulse with perturbations on the rear inner ice surface only (the outer surface and laser are assumed to be perfect). As we have seen above, most of the power on the rear surface at the onset of deceleration is concentrated in the low- $\ell$ -mode part of the spectrum, so the *ORCHID* calculations contain only modes up to  $\ell = 50$  (in contrast, the postprocessor calculations take into account modes up to  $\ell = 1000$ ). Various initial spectra of the form  $\sigma \sim \ell^{-\beta}$  were simulated to take into account the four seed terms.<sup>9</sup> The *ORCHID* calculations simulate the implosion through peak compression and burn. The spectra at the start of the deceleration phase obtained from the *ORCHID* simulations are compared to the spectra obtained from the instability postprocessor. This comparison is used to relate the postprocessor analysis to the full 2-D *ORCHID* simulations and obtain the yield for a given level of laser and target nonuniformity. It has been shown previously<sup>9</sup> that the  $\alpha = 3$

NIF target gain can be written as a function of  $\bar{\sigma}$ , where

$$\bar{\sigma}^2 = 0.06 \sigma_{\ell < 10}^2 + \sigma_{\ell \geq 10}^2;$$

$\sigma_{\ell < 10}^2$  and  $\sigma_{\ell \geq 10}^2$  are the rms nonuniformity of modes below and above 10, respectively. The instability postprocessor gives  $\bar{\sigma}$  at the onset of the deceleration phase for different initial conditions (laser imprint and surface roughness.) By comparing the amplitude and mode spectrum it is possible to relate the reduction in target performance for a given initial nonuniformity. For the  $\alpha = 3$  NIF design the instability analysis with an initial  $1 \mu\text{m}$  of inner ice nonuniformity,  $840\text{-\AA}$  outer surface roughness, and  $1\text{-THz}_{\text{UV}}$ , 2-D SSD illumination, the resulting  $\bar{\sigma}$  is  $1.3 \mu\text{m}$ . As we have already seen, the OMEGA design imprints less than the NIF design. Power balance and inner-ice-surface roughness are likely to be similar for both laser configurations. We use the same characterization of the nonuniformity in the deceleration phase for the non-igniting OMEGA target to obtain the neutron yield as a function of  $\bar{\sigma}$ . For the OMEGA design the instability analysis with the same initial conditions as the NIF capsule leads to a  $\bar{\sigma}$  of  $0.9 \mu\text{m}$ . Figure 82.8 shows the normalized (to 1-D) yield as a function of the deceleration nonuniformity parameter  $\bar{\sigma}$ . The OMEGA design has a larger reduction in yield for a given level of  $\bar{\sigma}$  than the NIF design. This can be attributed to the OMEGA design's smaller hot-spot radius compared to that of the NIF design, which makes the OMEGA hot spot more easily disrupted by the penetration of cold spikes from the main fuel layer. For the same initial conditions, however, the value of  $\bar{\sigma}$  is different between the



TC5269

Figure 82.8  
The yield, normalized to the 1-D result, as a function of  $\bar{\sigma}$ , the total nonuniformity at the start of the deceleration phase.

two designs. For the case outlined above, the NIF has a  $\bar{\sigma}$  of  $1.3 \mu\text{m}$ , which leads to a reduction to 60% of 1-D yield (giving a gain of 28), whereas the OMEGA design has a  $\bar{\sigma}$  of  $0.9 \mu\text{m}$  for the same conditions, which leads to a yield of 30% of 1-D.

This article has described the current target designs for the soon-to-be-commissioned OMEGA Cryogenic Target Handling System. These designs are energy scaled from the direct-drive ignition designs for the NIF with a major goal of experimentally studying the various sources of nonuniformity and their influence on target performance. The OMEGA and the NIF designs have been shown to have similar 1-D behavior and stability properties, which will facilitate the extrapolation of the cryogenic target studies on OMEGA to NIF targets. The smaller hot spot in the OMEGA design implies, however, that OMEGA cryogenic targets will be more sensitive to instability growth than the NIF direct-drive ignition targets. Our stability analyses are consistent with this observation and predict that with 1-THz<sub>UV</sub>, 2-D SSD, and  $1 \mu\text{m}$  of inner-ice-surface roughness we should obtain approximately 30% of the 1-D yield from the OMEGA cryogenic targets. Using the same analysis tools and similar target and laser uniformity levels, we predict that the  $\alpha=3$  direct-drive ignition design will give a gain of 28 on the NIF, a reduction to 60% of the 1-D yield.

#### ACKNOWLEDGMENT

This work was supported by the U.S. Department of Energy Office of Inertial Confinement Fusion under Cooperative Agreement No. DE-FC03-92SF19460, the University of Rochester, and the New York State Energy Research and Development Authority. The support of DOE does not constitute an endorsement by DOE of the views expressed in this article.

#### REFERENCES

1. Laboratory for Laser Energetics LLE Review **79**, 121, NTIS document No. DOE/SF/19460-317 (1999). Copies may be obtained from the National Technical Information Service, Springfield, VA 22161.
2. K. A. Brueckner and S. Jorna, *Rev. Mod. Phys.* **46**, 325 (1974).
3. S. P. Regan, D. K. Bradley, A. V. Chirokikh, R. S. Craxton, D. D. Meyerhofer, W. Seka, R. W. Short, A. Simon, R. P. J. Town, B. Yaakobi, J. J. Carol III, and R. P. Drake, *Phys. Plasmas* **6**, 2072 (1999).
4. V. N. Goncharov, S. Skupsky, T. R. Boehly, J. P. Knauer, P. McKenty, V. A. Smalyuk, R. P. J. Town, O. V. Gotchev, R. Betti, and D. D. Meyerhofer, *Phys. Plasmas* **7**, 2062 (2000).
5. V. N. Goncharov, "Self-Consistent Stability Analysis of Ablation Fronts in Inertial Confinement Fusion," Ph.D thesis, University of Rochester, 1998.
6. V. N. Goncharov, *Phys. Rev. Lett.* **82**, 2091 (1999).
7. S. W. Haan, *Phys. Rev. A* **39**, 5812 (1989).
8. S. V. Weber, S. G. Glendinning, D. H. Kalantar, M. H. Key, B. A. Remington, J. E. Rothenberg, E. Wolfrum, C. P. Verdon, and J. P. Knauer, *Phys. Plasmas* **4**, 1978 (1997).
9. V. N. Goncharov, S. Skupsky, P. W. McKenty, J. A. Delettrez, R. P. J. Town, and C. Cherfils-Clerouin, "Stability Analysis of Directly Driven OMEGA and NIF Capsules," to be published in the *Proceedings of the 1999 Inertial Fusion Sciences and Applications Conference*, Bordeaux, France, 12–17 September 1999; also Laboratory for Laser Energetics LLE Review **81**, 1, NTIS document No. DOE/SF/19460-335 (1999). Copies of the LLE Review may be obtained from the National Technical Information Service, Springfield, VA 22161.

---

## Imprint Reduction Using an Intensity Spike in OMEGA Cryogenic Targets

The primary obstacle to the successful implosion of an inertial confinement fusion target is hydrodynamic instability, which can cause the target to disintegrate and prevent it from reaching the high densities and temperatures required for ignition. The imploding target is primarily subject to the Rayleigh–Taylor (RT) instability, seeded by surface nonuniformity and by laser illumination nonuniformity, which can imprint itself on the target surface. Efforts to reduce laser imprint have employed primarily smoothing mechanisms such as smoothing by spectral dispersion (SSD),<sup>1</sup> distributed polarization rotators (DPR's),<sup>2</sup> and distributed phase plates (DPP's).<sup>3</sup> We present here a novel technique to further reduce imprint in OMEGA cryogenic (cryo) targets by a relatively simple modification to the standard pulse shape.

As reported elsewhere in this volume (p. 49), the base-line OMEGA cryogenic targets consist of a shell of deuterium–tritium (DT) ice surrounding a DT vapor region. For target fabrication, the DT ice must be surrounded by a thin (1–4  $\mu\text{m}$ ) layer of plastic (CH) or polyimide. This layer increases, however, the amount of imprint by introducing an additional period of RT growth near the start of the laser pulse.<sup>4</sup> Figure 82.9 shows the growth of laser imprint (i.e., the amplitude  $\eta$  of the outer-surface modulation) for a DT shell coated with 3  $\mu\text{m}$  of CH, compared with the imprint that would result from a pure-DT shell. For this example, the target was illuminated with a 5% laser nonuniformity and a 50- $\mu\text{m}$  nonuniformity wavelength. (To isolate the effect of laser nonuniformity, an initially smooth target surface was used in these simulations.) The qualitative features of the imprint are the same for both cases shown in Fig. 82.9. Initially, the imprint growth, which is roughly linear in time, results from the nonuniform shock, which is launched at the onset of laser irradiation. The imprint amplitude reaches a peak, representing the first quarter-cycle of the oscillations caused by dynamic overpressure.<sup>4</sup> (For some wavelengths of nonuniformity, half the period of oscillation is less than the foot-pulse duration, and the outer-surface amplitude reverses phase.) The amplitude grows exponentially, after about 1.5 ns, as the whole shell begins to accelerate and RT growth sets in. During the drive pulse, the target with

the 3- $\mu\text{m}$  CH shell has an imprint amplitude about twice that of the pure-DT shell. The increase in amplitude is initiated very early in the imprint process (within the first few hundred picoseconds for OMEGA targets), when a jump in the amplitude is produced by a brief acceleration of the CH shell, with resulting RT growth. The novel technique presented here significantly reduces this jump in amplitude and thereby reduces the imprint for the CH shell to approximately the level of the pure-DT shell.

The mechanism that produces the early, brief acceleration of the CH shell is illustrated in Fig. 82.10 by three plots of the density as a function of radius, at successive times early in the simulation. The onset of irradiation sends a shock into the CH layer. When the shock reaches the interface between the DT and the CH, a faster shock is sent into the less-dense DT, and a rarefaction wave (RW) returns to the outer surface through the CH layer. The RW accelerates the CH, while decreasing its pressure and density. While the outer surface is accelerated by the RW, it is subject to the RT instability.

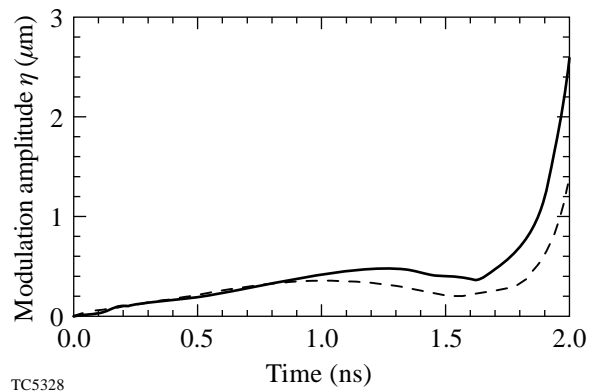


Figure 82.9

The amplitude of outer-surface modulations due to imprint, for an initially smooth target, driven by illumination with a 5%, 50- $\mu\text{m}$  nonuniformity. The solid curve represents a target with a 3- $\mu\text{m}$  CH layer surrounding a 72- $\mu\text{m}$  DT ice shell, while the dashed curve represents 84  $\mu\text{m}$  of DT, which gives the same total shell mass.

As the RW moves through the CH, it lowers the pressure from the post-shock CH pressure to the post-shock DT pressure; however, the laser irradiation imposes a pressure at the outer surface given by the ablation pressure. As a result, after the RW has crossed the outer surface, a weak *adjustment* shock is sent back into the target, which increases its pressure to the ablation pressure. This second shock is launched first at the trough of the surface perturbation, then later at the peak. This discrepancy in the time for the shock to be launched causes a decrease in the rate of amplitude growth  $\dot{\eta}$ .

The early-time growth due to the RW acceleration has the standard RT scaling and is greater for shorter wavelengths. For a given spherical harmonic with mode number  $\ell$ , the corresponding wavelength for an OMEGA target is approximately three times smaller than for a NIF target, and as a result, the early-time growth is greater.

We have found a relatively simple way to reduce the increased imprint caused by the CH overcoat: By introducing a brief, high-intensity spike at the start of the foot pulse (see Fig. 82.11), the effects of the early-time acceleration of the CH shell can be drastically reduced. Figure 82.12 shows the degree of imprint (given by the outer-surface modulation amplitude) for identical targets, which have pulses with and without this intensity spike, for a 50- $\mu\text{m}$  illumination perturbation. The spike, which is 50 ps in duration and has an intensity ratio with

the foot of 6:1, reduces the imprint by  $\sim 2$  at this wavelength. As seen, targets irradiated with an initial intensity spike experience a shorter period of early RT growth, which begins earlier in time, than those irradiated by the standard pulse. As a result, the RT growth starts with a lower amplitude and terminates earlier.

The intensity spike launches a stronger shock than the canonical foot-pulse shock. This results in a larger shock velocity, a greater amount of compression, and a thinner post-shock CH layer. Thus, the shock reaches the CH–DT interface earlier, and the rarefaction wave returns more quickly because of the thinner post-shock CH layer. (A stronger shock also leads to a greater post-shock temperature and higher sound speed, so that the RW travels more quickly.) This decreases not only the arrival time of the rarefaction wave but also its extent since the width of the RW grows linearly in time. As shown in Appendix A, the duration of the RT growth due to the RW is proportional to  $d/(\xi c_s)$ , where  $d$  is the width of the CH layer,  $\xi$  is the amount of shock compression, and  $c_s$  is the post-shock sound speed. As this dependence suggests, both of these factors lead to less early-time RT growth and less imprint.

For OMEGA cryo targets, the most-unstable modes are commonly taken to have spherical-harmonic mode numbers in the range  $20 \leq \ell \leq 75$  (corresponding to illumination nonuniformity wavelengths of  $40 \mu\text{m} \leq \lambda \leq 140 \mu\text{m}$ ). RT

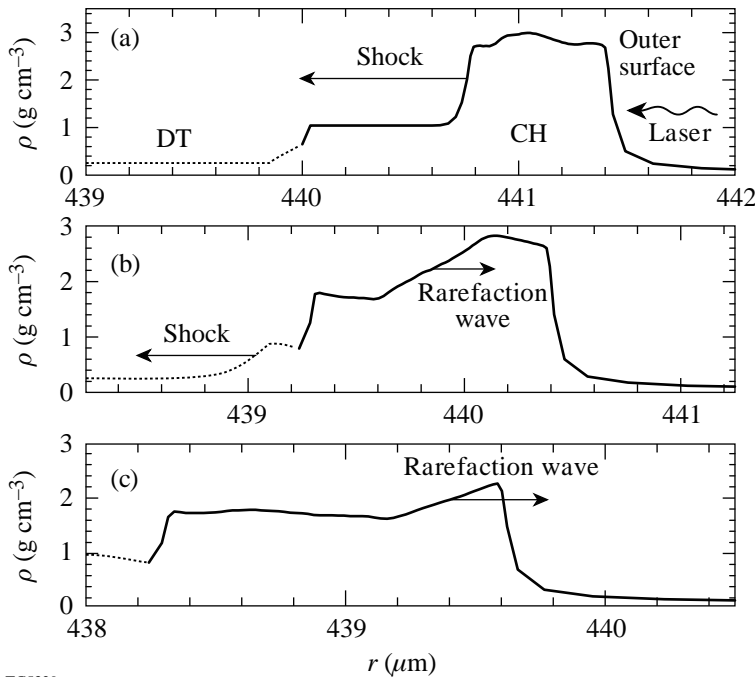
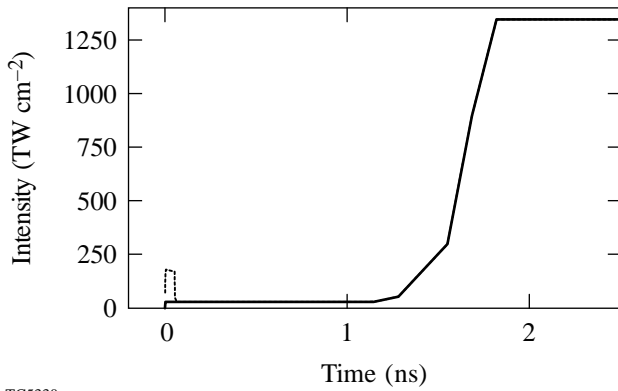


Figure 82.10  
The density profile at the outer edge of the target shell is shown at three consecutive times early in the implosion. Panel (a) shows the propagation of the foot-pulse shock through the thin outer CH layer. Panel (b) shows the return of the rarefaction wave from the CH/DT interface through the shocked CH to the outer surface of the target. Panel (c) shows the density while the rarefaction wave is accelerating the outer surface to the post-shock speed of the shocked DT. The CH layer is shown with a solid line, and the DT ice is represented by a dotted line.

TC5329

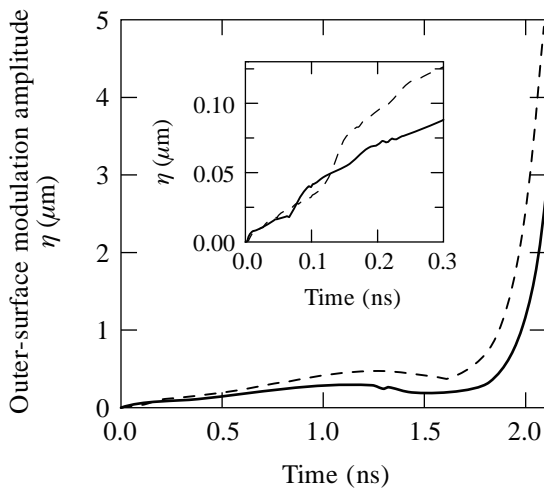
growth is greater for shorter wavelengths. Figure 82.13 shows pairs of simulations, with (solid) and without (dashed) the intensity spike, for two wavelengths, demonstrating this wavelength dependence.

A direct measure of the magnitude of imprint was suggested in Ref. 5 by Weber *et al.* They evaluate the degree of imprint by calculating, for a given illumination nonuniformity of wave number  $k$ , the *equivalent surface finish*  $\varepsilon(k)$ , defined as the



TC5330

Figure 82.11  
The pulse shape of an OMEGA cryogenic target, with (dotted) and without (solid) the initial intensity spike.



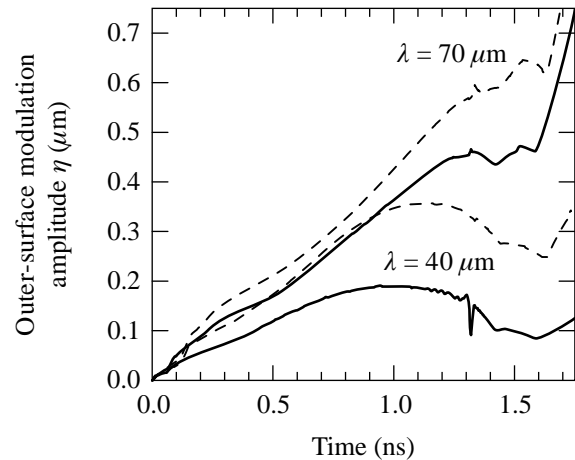
TC5331

Figure 82.12  
The amplitude  $\eta$  of the outer-surface modulation is shown for a 50- $\mu\text{m}$ -wavelength illumination perturbation, for targets using a 3- $\mu\text{m}$  overcoat layer of CH. The simulation using the standard cryo laser pulse is shown by a dashed line, while the simulation that used an initial intensity spike is shown by a solid line. The spike reduces the imprint by a factor of  $\sim 2$  at this wavelength. The early-time behavior is shown in the inset.

magnitude of initial surface nonuniformity  $\eta_{\text{surface}}(k, t = 0)$  necessary, in the absence of illumination nonuniformity, to produce the same outer-surface modulation amplitude  $\eta_{\text{surface}}(k, t)$  during the drive pulse:

$$\varepsilon(k) \equiv \frac{\eta_{\text{imprint}}(k, t)}{\eta_{\text{surface}}(k, t)} \eta_{\text{surface}}(k, t = 0). \quad (1)$$

Figure 82.14 shows the equivalent surface finish as a function of mode number  $\ell$  for simulations with and without the intensity spike, compared with that of an all-DT target with the standard pulse. In all cases (except for the short-wavelength, all-DT simulations, not shown in the figure), the spike reduces imprint. The equivalent surface finish was computed using the growth formula of Betti *et al.*,<sup>6</sup> where the ablation velocity, density scale length, and acceleration were taken from the all-DT, no-spike simulation, with coefficients  $\alpha = 0.94$  and  $\beta = 2.6$  during DT ablation and  $\alpha = 1.0$  and  $\beta = 1.7$  during CH ablation. We have also found that the thicker the outer CH layer, the greater the imprint reduction. The reduction in equivalent surface finish is large enough that even a target with a 3- $\mu\text{m}$  outer CH layer has the same equivalent surface finish as an all-DT target. This is also shown in Table 82.II, which lists the equivalent surface finish, averaged over mode number  $\ell$ , for a range of CH-layer thicknesses.



TC5332

Figure 82.13  
The outer-surface modulation amplitude  $\eta$ , for an initially smooth target, for a range of illumination nonuniformity wavelengths  $\lambda$ . Simulations are of targets with a 3- $\mu\text{m}$  outer layer of CH. Pulses with (without) the intensity spike are shown with solid (dashed) lines.

The initial intensity spike reduces imprint primarily by reducing the early-time RT growth resulting from the CH layer that overcoats the DT shell. Even for a single-layer target, however, the period of increased intensity further reduces imprint by increasing the size of the plasma atmosphere around the target. The laser energy is deposited primarily outside the critical surface in the target's corona, where the plasma frequency equals the laser light's frequency. This energy is conducted thermally to the ablation surface. Modeling the conduction zone has shown that the pressure perturbation decreases exponentially with distance from the critical surface,<sup>7</sup> so

$$\tilde{p}_a/p_a \sim (\tilde{I}/I) \exp(-fkD_c),$$

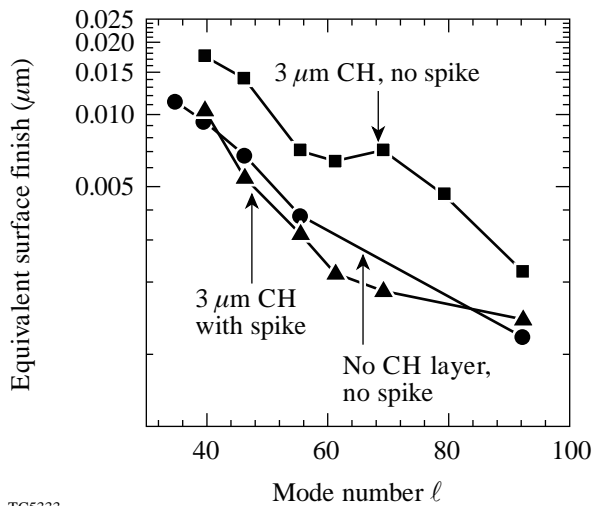
where  $D_c$  is the distance between the critical and ablation surfaces, or *smoothing distance*,  $p_a$  is the ablation pressure,  $\tilde{p}_a$  is its modulation amplitude,  $I$  is the laser intensity,  $\tilde{I}$  its modulation amplitude, and  $f$  is of order unity. The smoothing distance increases linearly in time, so  $D_c \sim V_c t$ , where  $V_c$  is the velocity of the critical surface with respect to the ablation surface. Greater laser intensity results in a more rapid growth of the conduction zone and a larger  $V_c$ . Analytical modeling of the conduction zone<sup>8</sup> shows a scaling of  $D_c \sim I^{4/3}$ . Once  $kD_c \sim 1$ , at the *decoupling time*, the laser nonuniformities are

decoupled from the target surface, and the ablation pressure is essentially uniform.

Because the degree of thermal smoothing is greater for higher laser intensities, the initial intensity spike also reduces imprint by increasing the smoothing distance. A series of simulations were performed for different wavelengths, with and without an intensity spike, of a target consisting of a shell of 84  $\mu\text{m}$  of DT ice. This shell width was chosen so the total shell mass would be comparable to that of the simulations with

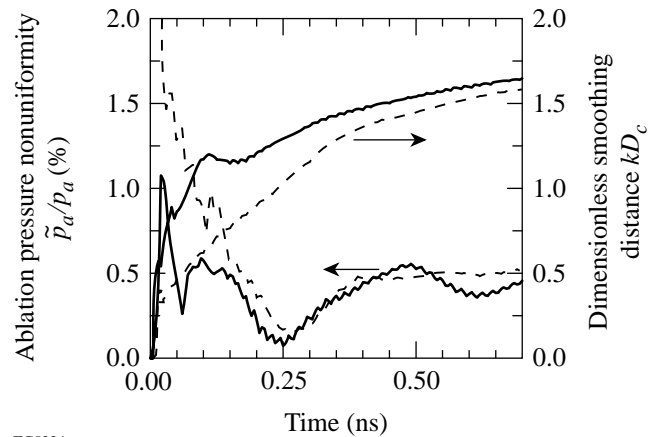
Table 82.II: The approximate reduction factor in equivalent surface finish, averaged over mode number  $\ell$ ,  $\langle \epsilon/\epsilon_{\text{spike}} \rangle_\ell$ , is shown for various thicknesses  $d$  (in  $\mu\text{m}$ ) of the outer CH layer. Also shown is  $\langle \epsilon_{\text{spike}}/\epsilon_{\text{DT}} \rangle_\ell$ , the approximate average over mode number of the ratio of equivalent surface finish for a simulation with an intensity spike and  $d$  microns of CH, to that of an all-DT target, without the intensity spike.

$d$ ( $\mu\text{m}$ )	$\langle \epsilon/\epsilon_{\text{spike}} \rangle_\ell$	$\langle \epsilon_{\text{spike}}/\epsilon_{\text{DT}} \rangle_\ell$
0	1.2	2.40
1	1.7	0.80
2	1.9	1.00
3	2.7	0.76



TC5333

Figure 82.14 The equivalent surface finish for a series of mode numbers  $\ell$ , for simulations with a 3- $\mu\text{m}$  outer CH layer, with and without an initial intensity spike, and for a pure-DT target without an intensity spike.



TC5334

Figure 82.15 The ablation pressure nonuniformity  $\tilde{p}_a/p_a$  and dimensionless smoothing distance  $kD_c$  for simulations with (solid) and without (dashed) an initial intensity spike. For these simulations,  $\lambda = 50 \mu\text{m}$ . The smoothing distance is taken to be the distance from the ablation surface to the critical surface. The curves showing  $\tilde{p}_a/p_a$  have been smoothed numerically to reduce the noise due to finite simulation resolution.

a 3- $\mu\text{m}$  CH layer, which have 72  $\mu\text{m}$  of DT. Consider first the simulation with  $\lambda = 50 \mu\text{m}$ : From the slope of  $\eta(t)$  in Fig. 82.15, which shows the ablation pressure nonuniformity  $\tilde{p}_a/p_a$  and dimensionless smoothing distance  $kD_c$  for simulations with (solid) and without (dashed) an initial intensity spike, we see that for the standard pulse shape,  $V_c \sim 35 \mu\text{m ns}^{-1}$  (ignoring the zero-time offset). This means that the decoupling time  $t_c \sim 230$  ps. Figure 82.15 also shows that, for  $t \geq t_c$ , the ablation pressure nonuniformity  $\tilde{p}_a/p_a$  has decreased to its asymptotic foot-pulse value of  $\sim 0.4\%$ . By contrast, the simulation (represented by the solid line) with the spike has a decoupling velocity, during the first 100 ps, of  $V_c \approx 90 \mu\text{m ns}^{-1}$ , and a correspondingly smaller decoupling time and ablation-pressure nonuniformity. In this case, the decoupling speed  $V_c$  decreases at  $t \sim 100$  ps because of the decrease in the laser intensity. The outer-surface modulation amplitude is shown in Fig. 82.16 (solid curves for pulse shapes including the intensity spike). As described above,  $\eta$  initially grows linearly. For example, the 50- $\mu\text{m}$  simulation without the spike has a perturbed shock speed of  $\tilde{v}_s \approx 0.7 \mu\text{m ns}^{-1}$ , which produces a linear growth rate of  $\dot{\eta} = 0.52 \mu\text{m ns}^{-1}$  (see Appendix A). This is comparable to the growth rate shown in Fig. 82.16.

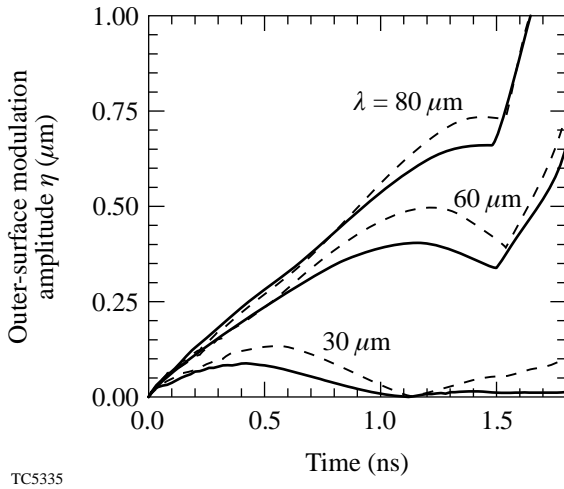


Figure 82.16  
The amplitude of the outer-surface modulation for various illumination nonuniformity wavelengths, for targets without a CH overcoat. Dashed curves represent the standard OMEGA cryogenic pulse shape, while the solid curves represent pulses with an initial intensity spike.

To facilitate modeling, an intensity spike with a sharp rise and fall was used for the simulations described above. A realistic pulse will have a finite rise and fall time. Replacing the square spike profile with a Gaussian profile preserves the essential features and imprint reduction described above: For

$\lambda = 50 \mu\text{m}$ , and a 5% laser nonuniformity amplitude, the equivalent surface finish for a 50-ps, 180-TW  $\text{cm}^{-2}$  spike is 0.0032  $\mu\text{m}$ , while for a 50-ps FWHM Gaussian spike with a peak intensity of 200 TW  $\text{cm}^{-2}$  (which delivers roughly the same energy), it is 0.003  $\mu\text{m}$ . (This is to be compared with an equivalent surface finish of 0.007  $\mu\text{m}$  without the intensity spike.) For a longer, less-intense spike of 100 ps and 120 TW  $\text{cm}^{-2}$ , the equivalent surface finish is 0.00055  $\mu\text{m}$ , while for a 100-ps FWHM Gaussian spike with a peak intensity of 140 TW  $\text{cm}^{-2}$ , it is 0.001  $\mu\text{m}$ .

The performance of an OMEGA target is reflected by the neutron yield  $Y$  that it produces. For an OMEGA cryo target, the drive-pulse shock must be launched sufficiently after the weaker foot-pulse shock so that they break out of the main fuel layer at about the same time. A change in the initial intensity changes the shock speed, potentially altering the shock timing. The fractional neutron yield (relative to the yield with no spike) for a range of intensity spike durations ( $dt$ ) and intensities ( $I$ ) is shown in Fig. 82.17. As this figure shows, the greater the  $I$  or  $dt$ , the lower the yield. However, because the foot pulse does not maintain the intensity used in the spike, the shock is unsupported and, after the duration of the spike, evolves into a decaying  $N$ -wave.<sup>9</sup> The true measure of the disruption caused by the spike is the energy it delivers to the target,  $I dt$ , as shown by the contours of constant  $Y$  in Fig. 82.17. Based on the 1-D

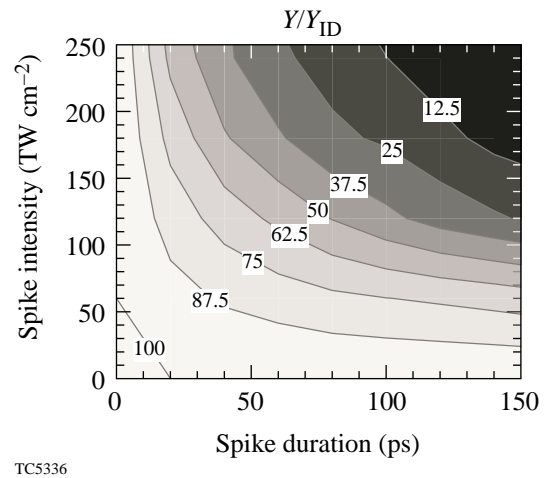


Figure 82.17  
Neutron yield as a fraction of the yield with no intensity spike, plotted in terms of the spike duration  $dt$  and intensity  $I$ . A spike intensity of less than the foot-pulse intensity, or duration of zero, indicates that the spike is absent. Operating on the 80% contour line will reduce imprint by about a factor of 2. Much of the reduction in yield can be recovered by shortening the foot pulse. Yields were calculated with *LILAC*.

simulations, the yield  $Y(I, dt)$  is of the same order as that of the canonical cryo target for a wide range of spike intensities and durations. In addition, because  $I dt \ll I_{\text{foot}} dt_{\text{foot}}$ , the fuel adiabat  $\alpha$  and the RT growth factor are not significantly changed by the spike. The main effect of the intensity spike is to alter the shock timing. For the example of a 100-ps spike with twice the foot-pulse intensity (i.e.,  $60 \text{ TW cm}^{-2}$ ), the imprint reduction is approximately a factor of 2 and the decrease in 1-D yield is only 20%. Much of the reduction in yield shown in Fig. 82.17 may be recovered by slightly shortening the duration of the foot pulse.

In summary, the presence of an initial intensity spike at the start of the foot pulse in an OMEGA cryogenic target reduces imprint by about a factor of 2 for typical target configurations. This imprint reduction comes at the cost of only a modest decrease in yield, most of which can be recovered by a small reduction in pulse length. Furthermore, this reduction in imprint occurs for those wavelengths of illumination nonuniformity considered to be the most dangerous for target performance.

#### ACKNOWLEDGMENT

One of the authors (TJBC) would like to thank V. Goncharov and P. B. Radha for many useful discussions. This work was supported by the U.S. Department of Energy Office of Inertial Confinement Fusion under Cooperative Agreement No. DE-FC03-92SF19460, the University of Rochester, and the New York State Energy Research and Development Authority. The support of DOE does not constitute an endorsement by DOE of the views expressed in this article.

#### Appendix A: Rarefaction-Wave Rayleigh–Taylor Growth

The RT growth due to the early-time RW acceleration was first discussed in the context of feedout by Betti *et al.*<sup>10</sup> A simple estimate of the early-time RT growth for NIF targets was performed by Goncharov *et al.*<sup>11</sup> using scaling laws. In this appendix we approximate the period of RT growth due to the RW return from the DT/CH interface in OMEGA cryo targets. As discussed above, when the foot shock reaches the interface between the CH and the DT ice, it behaves as if it has reached a contact discontinuity. At this point it proceeds as a stronger shock into the DT and sends a rarefaction wave outward toward the outer surface, communicating the new post-shock conditions. When the RW crosses the outer surface, it is accelerated to the post-shock speed of the DT.

This process is shown in Fig. 82.18, an  $r-t$  diagram for a simulation with a  $72\text{-}\mu\text{m}$  shell of DT ice, surrounded by  $3\text{-}\mu\text{m}$  of CH, and the standard OMEGA cryo pulse shape (see Fig. 82.11). (This DT-shell width was chosen so the shell would have the same total mass as that of the all-DT simula-

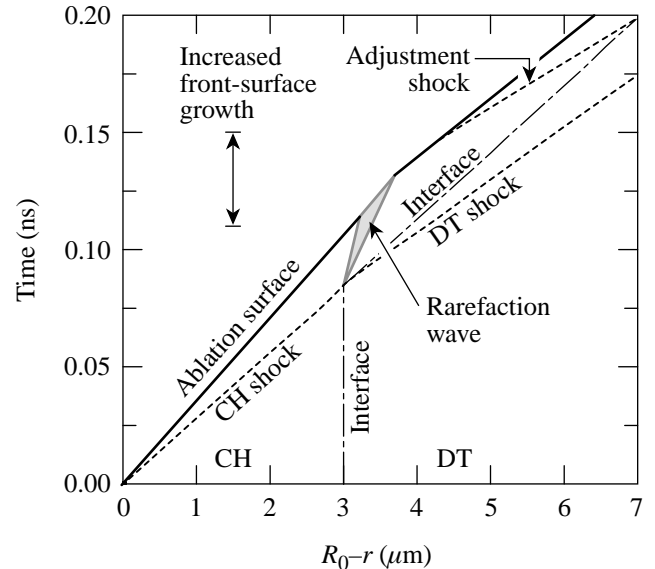
tions.) The duration of the RT growth may be estimated as follows: the RW is launched from the point  $(r_0, t_0)$ , where  $r_0 = R_0 - d$  ( $d = 3\text{-}\mu\text{m}$  being the width of the CH layer) and  $t_0 = r_0/v_s$  ( $v_s$  being the shock speed). The outer edge of the RW travels at the post-CH-shock sound speed, while the inner edge travels with a velocity of  $v_{\text{RW}}$ , given in Ref. 9 as

$$v_{\text{RW}} = -c_s + \frac{1}{2} [(\gamma + 1)V - (\gamma - 1)u]. \quad (\text{A1})$$

Here  $V$  is the post-DT-shock speed,  $\gamma$  is the ratio of specific heats, and  $u = (1 - \xi^{-1})v_s$  is the post-shock speed, where  $\xi$  is the degree of shock compression and a strong shock is assumed. The intersection  $(r_1, t_1)$  of the ablation front, which travels at speed  $u$ , and the outer edge of the RW wave is given by

$$r_1 = R_0 - d(1 - \xi^{-1})(1 + \xi^{-1}M_{\text{CH}}), \quad (\text{A2})$$

$$t_1 = \frac{d}{v_s}(1 + \xi^{-1}M_{\text{CH}}), \quad (\text{A3})$$



TC5337

Figure 82.18  
An  $r-t$  diagram for an OMEGA cryo simulation with a  $50\text{-}\mu\text{m}$  illumination perturbation, and a target shell composed of  $72\text{-}\mu\text{m}$  of DT ice and  $3\text{-}\mu\text{m}$  of CH. Shock and interface trajectories are shown as functions of the time  $t$  and the distance  $R_0 - r$  from the initial outer radius  $R_0$ . Note that, when the foot-pulse shock reaches the DT/CH interface, the shock speed increases and a forward-swept rarefaction wave (shaded region) is launched. Because the post-DT-shock pressure is not equal to the ablation pressure, a second adjustment shock is sent into the shell. Shocks are represented by dashed lines, and the CH/DT interface by a dashed-dotted line.

where  $M_{\text{CH}}$  is the Mach number of the foot-pulse shock traveling through the CH. If we approximate the speed of the ablation front during its passage through the RW by the average between its speeds before and after,  $(u + V)/2$ , the duration  $\Delta t$  of the RW acceleration is given by

$$\Delta t \approx \frac{(\gamma + 1) [\xi M_{\text{DT}} - (\xi - 1) M_{\text{CH}}]}{\{2\xi - \gamma [\xi M_{\text{DT}} - (\xi - 1) M_{\text{CH}}]\}} \times \frac{d}{\xi c_s}, \quad (\text{A4})$$

where  $M_{\text{DT}} \equiv V/c_s$ . During this period, the ablation surface is subject to the RT instability. In addition, because the RW reaches the “trough” of the outer-surface perturbation first, the period of acceleration is extended by a period of approximately  $\Delta t' = 2|\eta(t_1)|/c_s$ . For uniform laser illumination, the outer radius of the target is given, during the foot pulse (and before foot-pulse shock breakout), by  $R(t) = R(0) - ut = R(0) - (1 - \xi^{-1})v_s t$ , where  $t$  is the time since the start of the laser pulse and  $u$  is the post-shock speed. Perturbing this equation for  $R(t)$ , we find that an initially smooth target will develop a surface modulation given by

$$\eta(t) = (1 - \xi^{-1}) \tilde{v}_s t, \quad (\text{A5})$$

where  $\tilde{v}_s$  is the modulation amplitude of the shock speed, assuming a strong shock. Inserting Eq. (A5) into the expression for  $\Delta t'$  yields

$$\Delta t' \approx 2 \frac{d}{c_s} (1 - \xi^{-1}) (1 + M_{\text{CH}} \xi^{-1}) \frac{\tilde{M}_{\text{CH}}}{M_{\text{CH}}}, \quad (\text{A6})$$

where  $\tilde{M}_{\text{CH}} \equiv \tilde{v}_s/c_s$ . The RT growth factor due to the RW is given approximately by

$$G_{\text{RW}} \approx e^{\sqrt{(V-u)k(\Delta t + \Delta t')}}. \quad (\text{A7})$$

After the early period of growth, the outer-surface modulation continues to grow at a constant rate. As the RW propagates, it lowers the pressure and density of the shocked CH; however, as mentioned above, the laser imposes a pressure equal to the

ablation pressure at the outer surface. Thus when the RW reaches the outer surface, a second, *adjustment* shock is launched into the CH to increase the pressure in the shell. As this shock is launched,  $\dot{\eta}$  is decreased to approximately the value it had before the RW return. The inset in Fig. 82.12 shows the period of initial linear growth, followed by the early-time RT growth. There is a subsequent decrease in the linear growth rate because the adjustment shock is launched from the trough of the surface perturbation before the peak. The outer surface undergoes slightly more than one quarter of a period of an oscillation before the drive pulse begins, followed by RT growth.

## REFERENCES

1. S. Skupsky, R. W. Short, T. Kessler, R. S. Craxton, S. Letzring, and J. M. Soures, *J. Appl. Phys.* **66**, 3456 (1989).
2. T. R. Boehly, V. A. Smalyuk, D. D. Meyerhofer, J. P. Knauer, D. K. Bradley, C. P. Verdon, and D. Kalantar, in *Laser Interaction and Related Plasma Phenomena*, edited by G. H. Miley and E. M. Campbell (American Institute of Physics, New York, 1997), Vol. 406, pp. 122–129.
3. Y. Lin, T. J. Kessler, and G. N. Lawrence, *Opt. Lett.* **20**, 764 (1995).
4. Laboratory for Laser Energetics LLE Review **80**, 185, NTIS document No. DOE/SF/19460-321 (1999). Copies may be obtained from the National Technical Information Service, Springfield, VA 22161.
5. S. V. Weber, S. G. Glendinning, D. H. Kalantar, M. H. Key, B. A. Remington, J. E. Rothenberg, E. Wolfrum, C. P. Verdon, and J. P. Knauer, *Phys. Plasmas* **4**, 1978 (1997).
6. R. Betti, V. N. Goncharov, R. L. McCrory, P. Sorotokin, and C. P. Verdon, *Phys. Plasmas* **3**, 2122 (1996).
7. K. A. Brueckner and S. Jorna, *Rev. Mod. Phys.* **46**, 325 (1974).
8. W. M. Manheimer, D. G. Colombant, and J. H. Gardner, *Phys. Fluids* **25**, 1644 (1982).
9. G. B. Whitham, *Linear and Nonlinear Waves*, Pure and Applied Mathematics (Wiley, New York, 1974).
10. R. Betti, V. Lobatchev, and R. L. McCrory, *Phys. Rev. Lett.* **81**, 5560 (1998).
11. V. N. Goncharov, S. Skupsky, T. R. Boehly, J. P. Knauer, P. McKenty, V. A. Smalyuk, R. P. J. Town, O. V. Gotchev, R. Betti, and D. D. Meyerhofer, *Phys. Plasmas* **7**, 2062 (2000).

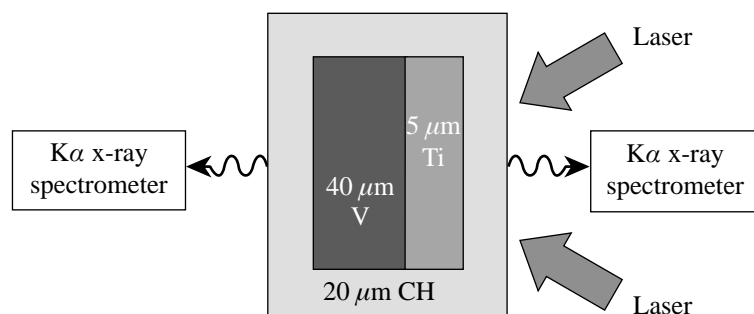
# Measurement of Preheat due to Fast Electrons in Laser Implosions

## Introduction

Fast electrons due to the two-plasmon-decay (2PD) instability have been measured in previous laser-interaction experiments.<sup>1,2</sup> The main impact of these electrons in laser-fusion experiments is the possible preheat that can reduce the implosion's effectiveness. The preheat caused by these electrons is studied by measuring the  $K\alpha$  line emission from high-Z layers in a flat-target geometry on the OMEGA<sup>3</sup> laser system. The  $K\alpha$  emission is directly related to the preheat level;<sup>4,5</sup> for sufficiently high fast-electron temperatures ( $T_{\text{fast}}$ ) the relationship between the  $K\alpha$  intensity and the preheat level is independent of  $T_{\text{fast}}$ . The preheat due to fast electrons in UV laser irradiation is relatively small and is usually masked by the preheat due to radiation. To overcome this problem, a target containing titanium (Ti) and vanadium (V) layers was designed so that when irradiated from the Ti side, most of the Ti- $K\alpha$  is excited by radiation, whereas most of the V- $K\alpha$  is excited by the fast electrons. As seen below, the thick Ti and V layers required for the  $K\alpha$  measurement precluded conducting this experiment in spherical geometry. We show, however, that such measurements can be used as a reference point for hard x-ray continuum detectors, which can then be used to determine the preheat in undoped spherical targets. The  $K\alpha$  measurements can conveniently be used as a reference point because in the case of x-ray continuum measurements  $T_{\text{fast}}$  must be known to determine the preheat level even at high temperatures.

## Flat-Target Experimental Configuration

The configuration for the flat-target experiment is shown in Fig. 82.19. Ten OMEGA beams of 1-ns square pulse duration and 4.85-kJ total energy are overlapped to yield a target irradiance of  $1.5 \times 10^{15} \text{ W/cm}^2$ . This value exceeds the irradiance in spherical implosion experiments on OMEGA, thus providing an upper limit on preheat in future experiments. The target consists of two main layers: 5- $\mu\text{m}$ -thick titanium and 40- $\mu\text{m}$ -thick vanadium. The 20- $\mu\text{m}$ -thick CH overcoat precludes any direct laser irradiation or heating of either metal, thus restricting laser interaction with the metals to preheat only. Indeed, the only lines seen in the measured spectra are the Ti- and V- $K\alpha$  lines. Two time-integrating x-ray spectrometers observe the spectrum emitted from the front side and the back side of the target. The purpose of the two-layer target is to ensure that most of the V- $K\alpha$  line is excited by fast electrons, not radiation. The Ti layer is thick enough to strongly absorb radiation above the Ti-K edge, thus minimizing the radiative excitation of  $K\alpha$  in the vanadium. To further increase the emission of the V- $K\alpha$  line due to fast electrons, the V-layer thickness should be made about equal to the range of fast electrons. Analysis of the  $K\alpha$  line intensities indicates, as seen below, a fast-electron temperature exceeding  $\sim 50 \text{ keV}$ . The range in vanadium can be well approximated<sup>6</sup> by the relation  $R(\text{g/cm}^2) = 9.4 \times 10^{-6} E^{5/3}$ , where  $E$  is the electron energy in keV. Thus the range of the fast electrons in vanadium is a few tens of microns. The  $(1/e)$  attenuation length of the V- $K\alpha$  line



E10228b

Figure 82.19

Experimental configuration for measuring fast-electron preheat. Ten incident laser beams are absorbed in the CH layer. Radiation excites the Ti- $K\alpha$  line, but most of it is absorbed before reaching the vanadium layer. On the other hand, fast electrons can penetrate the vanadium layer and excite the V- $K\alpha$  line.

in vanadium, however, is  $\sim 18 \mu\text{m}$ ; thus the vanadium layer should not be significantly thicker than  $\sim 18 \mu\text{m}$ , hence the choice of  $\sim 40 \mu\text{m}$ . Vanadium was chosen because the  $K\alpha$  lines of Ti and V are close enough to be simultaneously observed in the spectrum. Also, the back-layer material should have the higher  $Z$  of the two; otherwise, radiation of energy between the Ti- $K$  edge (4.96 keV) and the V- $K$  edge (5.46 keV) will be transmitted through the front layer and will strongly contribute to  $K\alpha$  emission in the back layer, contrary to the main goal of the experiment. Two crystal spectrometers viewed the emitted spectrum from the front and back of the target. The crystal in the front spectrometer was Ge(1,1,1); the one in the back was ADP(1,0,1).

Figure 82.20 shows the observed spectra from the front side and the back side of the target for shot 18167.  $K\alpha$  lines of Ti and V are seen, as well as the continuum emitted from the interaction region in the CH coating. The absolute energy in the  $K\alpha$  lines, which is required to determine preheat, is based on the following calibrations: (a) for the Ge crystal, a calibration performed at LLE<sup>7</sup> that agrees very well with the Darwin–Prins model,<sup>8</sup> (b) for the ADP crystal, two consistent calibrations,<sup>9,10</sup> and (c) for the DEF film, published calibration,<sup>11</sup> for which the film processing procedure was closely followed here. It should be further noted that both crystal calibrations change very little over the energy range of primary interest here,  $\sim 4.5$  to 5 keV. The target is viewed through a 25- $\mu\text{m}$ -

wide slit, which provides a one-dimensional image of the target at each wavelength, from which the space-integrated emission is computed. The space-integrated emission is larger than the measured emission by approximately the factor  $d/[d(1+M^{-1})]$ , where  $D$  is the FWHM of the emission region,  $d$  is the slit width, and  $M$  is the magnification. The following three sections deal with the analysis of the flat-target experimental results.

### Analysis of $K\alpha$ Emission

To analyze the measured  $K\alpha$  lines we first calculate their excitation due to radiation alone. We use the measured continuum intensity (Fig. 82.20) that is emitted by the laser-interaction region in the CH and transport it through the Ti and V layers (absorption in the CH is negligibly small). Only radiation above the Ti- $K$  edge (4.96 keV) must be included to calculate the excitation of either  $K\alpha$  line. Using the known opacity of cold Ti or V per unit areal density,  $\tau(E)$ , we solve the radiation transport equation for the spectral intensity  $I(x,E)$  into  $2\pi$  solid angle:

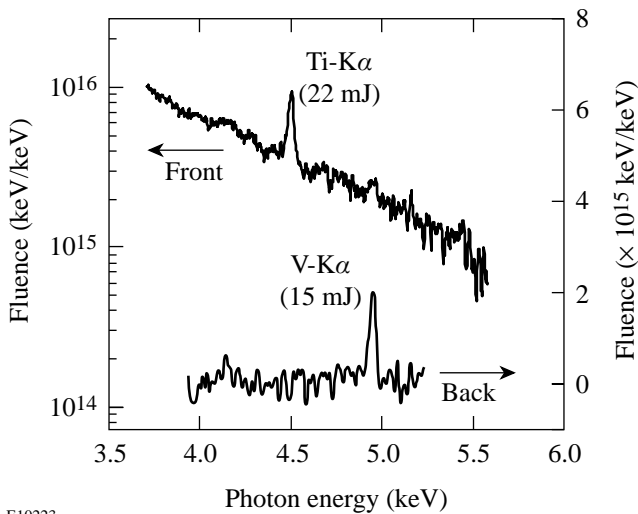
$$dI(x,E)/dx = -\tau(E)\rho I(x,E), \quad (1)$$

from which the local emission of Ti- $K\alpha$  is calculated according to

$$I(\text{Ti} - K\alpha) = E(K\alpha)\omega_K(\text{Ti})$$

$$\int_{E_K}^{\infty} I(x,E) \{1 - \exp[-\tau(\text{Ti})\rho\Delta x]\} dE/E, \quad (2)$$

and likewise for the V layer. Here  $\omega_K = 0.22$  is the fluorescence yield<sup>12</sup> of Ti, and  $E(K\alpha) = 4.508$  keV is the photon energy of the Ti- $K\alpha$  line; for V,  $\omega_K = 0.25$  and  $E(K\alpha) = 4.952$  keV. Using the normal density of the metal ( $\rho$ ) is justified since in plane geometry the areal density  $\rho\Delta x$  does not change when compression or expansion takes place. Also, shock arrival for most of the vanadium occurs after the laser pulse; thus, the preheating has been completed. The cold-metal opacity can be used since, as shown below, the degree of ionization due to the preheat is small (on average, two electrons per atom). Also, when removing the outer ( $M$ -shell) electrons, the  $K$  edge shifts very slightly to higher energies, but the absorption cross section at a given photon energy changes insignificantly.<sup>13</sup> The resulting spatial profiles of  $K\alpha$  emission, plotted in Fig. 82.21, show that some radiation survives

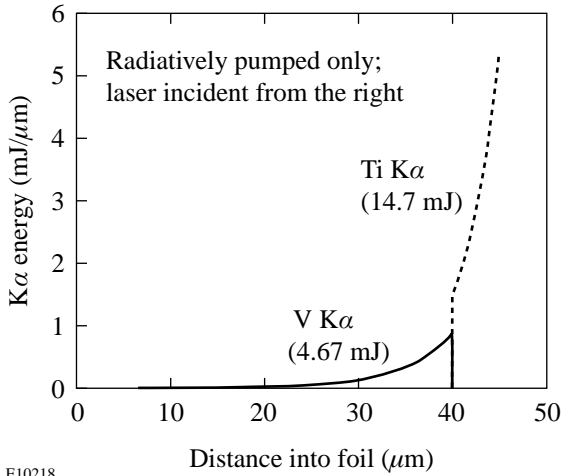


E10223

Figure 82.20

Time-integrated spectra emitted from the front and back of the target shown in Fig. 82.19. The measured line-intensity ratios are used to prove that the intensity of the V- $K\alpha$  line (observed from the back) is mostly due to fast electrons.

absorption in the titanium and excites V-K $\alpha$  near the V-Ti interface. The contribution of the observed K $\alpha$  lines is finally obtained by performing a radiation transport calculation of the K $\alpha$  line in both directions (exiting the target on the Ti side and on the V side, respectively). We now show that the results of these calculations disagree with the experiment, indicating that radiation alone cannot explain the measured intensity ratios, without the inclusion of fast-electron excitation of K $\alpha$ . For these considerations we use only line-intensity ratios, so the conclusion is independent of the accuracy in absolute calibration. Table 82.III compares the measured K $\alpha$  line-intensity ratios with the prediction of the radiative model, where front designates observation on the Ti (or laser side) and back designates observation on the V side of the target. The first measured ratio, V (back)/Ti (front), is much higher than predicted by the radiative model because fast electrons increase the V-K $\alpha$  intensity more than that of the Ti-K $\alpha$  intensity (because of the larger thickness of the former). Also, fast electrons excite V-K $\alpha$  throughout the vanadium layer rather than only near the V-Ti interface, thus reducing its attenuation when exiting on the V side. The same combination of effects explains the disagreement of the second ratio, V (back)/Ti (back). The third ratio, V (back)/V (front), is sensitive only to the spatial distribution of V-K $\alpha$  emission rather than to its origin. The disagreement in this case indicates that the V-K $\alpha$  line is emitted deeper into the vanadium and thus is attenuated less toward the back side, indicating again the contribution from long-range fast electrons.



E10218

Figure 82.21

Calculated spatial profiles of K $\alpha$  line emissions due only to radiation in the target of Fig. 82.19. The measured radiation from the interaction region (Fig. 82.20) was used as input.

Table 82.III: Comparison of radiative-model predictions and measurements.

K $\alpha$ -Line-Intensity Ratios	Radiative-Model Predictions	Measurements (Shot 18167)
V (back)/Ti (front)	0.05	~0.7
V (back)/Ti (back)	0.37	>>1
V (back)/V (front)	0.25	~5

We next analyze quantitatively the contribution of fast electrons to the K $\alpha$  line emission and show that the V-K $\alpha$  line viewed from the back is indeed excited mostly by fast electrons. We assume that the energies of fast electrons have a Maxwellian distribution (this assumption is based on 2-D simulations of the two-plasmon-decay instability<sup>14</sup>); the temperature and total energy of the fast electrons are considered free parameters in the calculation. A multigroup transport simulation of the electrons streaming through the Ti and V layers is performed, using the Bethe-Bloch slowing-down formula<sup>15</sup>

$$(-dE/dx)_{\text{coll}} = (2\pi e^4 N_a Z/E_0) \ln(1.16 E_0/\langle E_i \rangle), \quad (3)$$

where  $N_a$  is the atomic density,  $E_0$  the energy of the projectile electron, and  $\langle E_i \rangle$  the effective ionization energy.  $\langle E_i \rangle$  is determined by fitting Eq. (3) to experiments<sup>16</sup> using beam interaction with foil targets. For Ti,  $\langle E_i \rangle \sim 215$  eV, and for V,  $\langle E_i \rangle \sim 220$  eV. The validity of using this formula is discussed in Appendix A. The production of K $\alpha$  is calculated by the rate

$$dE(K\alpha)/dx = \sigma_K(E_v)(\rho/M_a)\omega_K(\text{Ti})E_K, \quad (4)$$

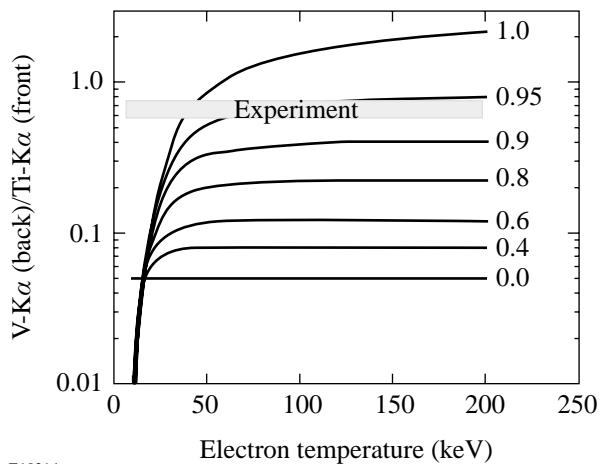
where the cross section is given by<sup>17</sup>

$$\sigma_K = (\pi e^4/E_v E_K) Z_K b_K \ln(c_K E_v/E_K), \quad (5)$$

where  $E_v$  is the photon energy,  $\rho$  is the mass density,  $M_a$  is the atomic mass,  $Z_K$  is the number of electrons in the  $K$  shell, and  $b_K$  and  $c_K$  are constants that change slowly with  $Z$ . By fitting Eq. (5) to detailed calculations,  $b_K$  and  $c_K$  have been determined for a wide range of elements. Even though Eq. (5) is nonrelativistic, the fitting was done for electron energies up to  $\sim 30$  times the  $K$ -edge energy, or  $\sim 160$  keV. Having determined thus the spatial distribution of K $\alpha$  line emission due to electrons, we transport the line intensity in both directions (as above) to calculate the contribution to the observed K $\alpha$  lines.

We finally add up the contributions from radiation and fast electrons and compare the calculated and measured  $K\alpha$  lines. As noted above, the calculated contribution of electrons depends on two free parameters (their temperature and total energy), whereas the contribution of radiation is calculated directly from the observed spectrum.

Figure 82.22 shows the results of the calculations for the ratio V (back)/Ti (front) as a function of the assumed electron temperature. The parameter for each curve is related to the assumed total energy in fast electrons. It is expressed as the fractional contribution of fast electrons to the V- $K\alpha$  (back) emission intensity. The experimental value of the V- $K\alpha$ (back)/Ti- $K\alpha$  (front) ratio,  $0.7\pm 0.1$ , is shown as a gray band in Fig. 82.22. The line marked 0.0 corresponds to removing the fast-electron component, whereas the curve marked 1.0 corresponds to removing the radiation component. In the limit of very high fast-electron temperatures (where the production of  $K\alpha$  lines by fast electrons is uniform over the target volume) the latter curve approaches the value  $\sim 2.3$ . This is smaller than the ratio 8 of V and Ti thicknesses because of the larger attenuation of the back-emergent V- $K\alpha$  line as compared with the front-emergent Ti- $K\alpha$  line. At low temperatures the electrons barely penetrate the Ti layer, and the V- $K\alpha$  line drops sharply. Comparing the curves in Fig. 82.22 with the experimental value indicates that *the electron temperature is higher*



E10214

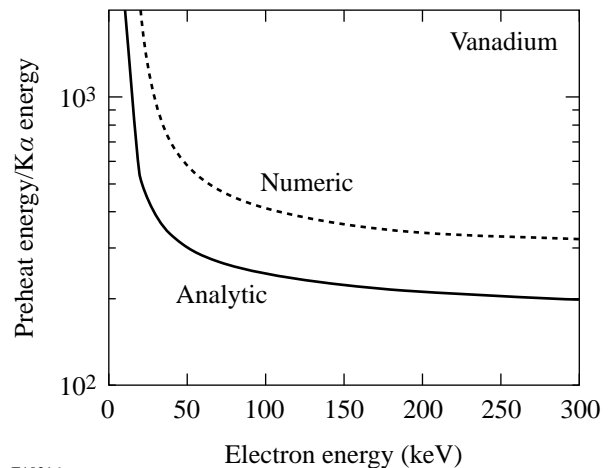
Figure 82.22

Calculated and measured ratio of V- $K\alpha$  observed from the back to Ti- $K\alpha$  observed from the front of the target due to both radiation and fast electrons. The parameter for each curve is the fraction of the V- $K\alpha$  line that is excited by electrons. Comparison with the experimental value of this ratio shows that (a) the V- $K\alpha$  line is excited almost exclusively by fast electrons, and (b) the temperature of fast electrons is  $\geq 50$  keV.

than  $\sim 50$  keV. For lower electron temperatures the V- $K\alpha$  line cannot be excited appreciably, and any excitation will be close to the Ti-V interface and be severely attenuated toward the back. Additional determinations of the fast-electron temperature will be described in the following sections. The primary conclusion from Fig. 82.22 is that *almost all of the intensity of the V- $K\alpha$  line (viewed from the back) is due to electron excitation*. This observable will now be used to estimate the preheat due to fast electrons.

### Determination of Electron Preheat from $K\alpha$ Measurements

In this section we discuss the determination of preheat level by fast electrons, using the  $K\alpha$  emission from the vanadium layer; preheat level as determined by hard x-ray emission will be the subject of the subsequent section. By dividing Eq. (3) by Eq. (4) we obtain the ratio of preheat to electron production of  $K\alpha$  lines. The result for V is shown as the curve marked *analytic* in Fig. 82.23. This curve tacitly assumes that the fast electrons are mono-energetic and the target is much thinner than the attenuation length. To remove these assumptions, we used the multigroup transport simulation described above to calculate the attenuation and  $K\alpha$  production of a Maxwellian distribution of electrons moving through the actual target used in this experiment. This calculation accounts for the distortion of the original Maxwellian distribution during transport



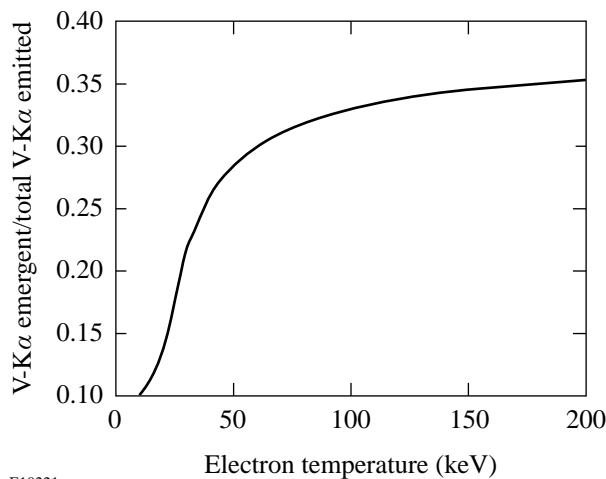
E10216

Figure 82.23

Determination of preheat from the measured V- $K\alpha$  intensity (after correction for transport, using Fig. 82.24). The analytic curve is the ratio of the relevant rates per cm propagation, while the numeric curve is the result of multigroup calculation for an initially Maxwellian distribution transported through the target of Fig. 82.19; for the latter case the abscissa values refer to the temperature of the fast electrons.

through the foil. The ratio of the space-integrated preheat and  $K\alpha$  production is shown by the curve marked *numeric* in Fig. 82.23; the abscissa for this curve is now the temperature rather than the energy of the fast electrons. The numeric curve is higher than the analytic curve because the slowing-down gradually brings the electrons to energies where the preheat is more effective. Finally, by multiplying the measured  $K\alpha$  energy (in absolute magnitude) by the appropriate value of the numeric curve, the preheat energy deposited in the target can be determined. As seen in Fig. 82.23,  $T_{\text{fast}}$  need not be known accurately to determine the preheat, as long as it is higher than  $\sim 50$  keV; Fig. 82.22 indicates that this was indeed the case here. It should be noted that the  $K\alpha$  intensity for this curve refers to the total local emission of  $K\alpha$ , which must be deduced from the observed  $K\alpha$ . The relation between the two depends on the spatial distribution of  $K\alpha$ , which in turn depends on  $T_{\text{fast}}$ . Also, the  $K\alpha$  intensity for this curve refers to the fraction of  $K\alpha$  that is excited solely by electrons.

Starting with the 15-mJ observed energy of V- $K\alpha$  (back), we estimate the total local V- $K\alpha$  emission. In Fig. 82.24 we show the relationship between the two as a function of  $T_{\text{fast}}$ . For  $T_{\text{fast}}$  higher than  $\sim 50$  keV the ratio is  $\sim 0.35$ , yielding 39 mJ for the total emission of V- $K\alpha$ . From Fig. 82.23 this corresponds to a preheat in the V of  $\sim 12$  J. For the total Ti-V target the preheat is  $\sim 14$  J (an increase of approximately the ratio of thicknesses  $45 \mu\text{m}/40 \mu\text{m}$ ); thus the preheat energy is about 0.3% of the incident laser energy.



E10221

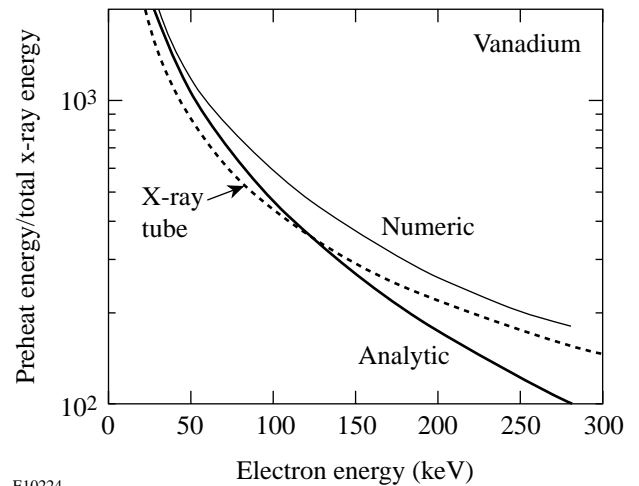
Figure 82.24  
Calculated ratio of V- $K\alpha$  energy emergent from the back of the target to the total volume emission of V- $K\alpha$ . The former quantity is the one measured, whereas the latter is used to derive the preheat.

### Determination of Electron Preheat from Hard X-Ray Measurements

In undoped targets, with no emission of  $K\alpha$  lines, preheat levels can be determined by measuring the spectrum of hard x-ray continuum. We show here that the spectrum-integrated x-ray continuum is directly related to the preheat deposited in the target, with no need to know the trajectories of the fast electrons in and around the target or the energy lost to the acceleration of ions. The loss rate due to bremsstrahlung is given by the Heitler relativistic formula<sup>18</sup>

$$\begin{aligned} (-dE/dx)_{\text{rad}} = N_a Z^2 \alpha (e^2/mc^2)^2 (E_0 + mc^2) \\ \times \left\{ 4 \ln \left[ 2(E_0 + mc^2)/mc^2 \right] - 4/3 \right\}, \quad (6) \end{aligned}$$

where  $N_a$  is the atomic density,  $\alpha$  is the fine-structure constant, and  $E_0$  is the energy of the projectile electron. It should be noted that, unlike for the collision loss rate, the relativistic formula yields considerably higher values than the classical formula (by a factor of  $\sim 2$  at 100 keV). Dividing Eq. (3) by Eq. (6) gives the ratio of preheat energy to radiation energy, shown by the curve marked *analytic* in Fig. 82.25. As in the equivalent case of  $K\alpha$  energy (Fig. 82.23) we use a multi-group electron transport calculation applied to the target in



E10224

Figure 82.25  
Determination of preheat from the spectrum-integrated hard x-ray emission. The analytic curve is the ratio of the relevant rates per cm propagation, while the numeric curve is the result of multigroup calculation for an initially Maxwellian distribution transported through the target of Fig. 82.19; for the latter case the abscissa values refer to the temperature of the fast electrons. The curve marked *x-ray tube* is the inverse of the empirical x-ray efficiency of a vanadium x-ray tube of an applied voltage  $E$ .

Fig. 82.19. The electrons are assumed to have a Maxwellian distribution of energies (rather than the same energy); the attenuation and distortion of the distribution during transport through the thick target are accounted for, and the ratio of space-integrated preheat and radiation is calculated. The result is marked *numeric* in Fig. 82.25, and for this curve the abscissa designates the temperature rather than the energy of the fast electrons. As in Fig. 82.23, the numeric curve is higher than the analytic curve; this is simply due to the rise of the curves in Fig. 82.25 for lower energies.

We can gain additional confidence in the curves in Fig. 82.25 by comparing them with the efficiency data of an x-ray tube with a vanadium anode. The input power that accelerates the electrons in the tube is converted mainly to heating the anode (equivalent to preheat in our case), with a fraction converted to x rays, mostly continuum. The power of x-ray continuum emission is given by<sup>19</sup>  $P = K(Z) \times Z \times I \times V^2$ , where  $V$  and  $I$  are the accelerating voltage and the tube current, respectively, and  $K$  depends weakly on  $Z$ . Thus, the ratio of preheat to radiation is  $\varepsilon = [Z \times V \times K(Z)]^{-1}$ . For vanadium, the empirical value<sup>19</sup> of  $K$  is  $\sim 1.1 \times 10^{-6} \text{ keV}^{-1}$ , resulting in the curve marked *x-ray tube* in Fig. 82.25 ( $V$  is the electron energy). Good agreement with the theoretical curves is seen.

#### ACKNOWLEDGMENT

Useful discussions with R. W. Short are gratefully acknowledged. This work was supported by the U.S. Department of Energy Office of Inertial Confinement Fusion under Cooperative Agreement No. DE-FC03-92SF19460, the University of Rochester, and the New York State Energy Research and Development Authority. The support of DOE does not constitute an endorsement by DOE of the views expressed in this article.

#### Appendix A: Slowing-Down Formulas for Partly Ionized Vanadium

The Bethe–Bloch slowing-down equation [Eq. (3)] applies to charged particles interacting with a cold, un-ionized target. In our case the vanadium layer is heated by fast electrons (and also by a shock wave) and is partly ionized. We examine here the required modifications to Eq. (3). We start by estimating the degree of ionization in the vanadium, based on the total target preheat energy estimated above. The total preheat derived from the  $K\alpha$  lines was 14 J. Dividing this energy by the preheated volume (given by the product of the focal-spot area and the target thickness), we derive a preheat per atom of  $E_a \sim 100$  eV. We estimate the temperature and average ionization consistent with  $E_a$  by solving the Saha equations of vanadium charge states and calculating  $E_a$  and  $\langle Z \rangle$  from

$$E_a = (3/2)[\langle Z \rangle + 1]kT_e + \sum_Z N_Z E_i(Z), \quad (\text{A1})$$

$$\langle Z \rangle = \sum_Z Z N_Z,$$

where  $N_Z$  is the relative population and  $E_i(Z)$  is the ionization energy of charge state  $Z$ . For any chosen value of the mass density  $\rho$  we find the  $N_e$  and  $T_e$  values that satisfy two conditions: (a) the calculated value of  $E_a$  from Eq. (A1) equals 100 eV and (b) the value of  $\langle Z \rangle$  calculated from Eq. (A1) agrees with  $N_e M_a / \rho$  ( $M_a$  is the atom mass). There is a unique solution consistent with both  $\rho$  and  $E_a$ . For mass densities in the range of 0.1 to 10 times the solid density of V, the resulting temperature varies from 18 to 43 eV and  $\langle Z \rangle$  varies from 1.4 to 2.6; therefore, only about 10% of the V and Ti electrons are ionized, whereas the rest remain bound. In calculating the slowing-down of the projectile electrons we must add the contributions of the bound electrons and the plasma (as shown below, the two are not totally independent). In justifying the approximations adopted below, we shall assume as typical parameter values an electron projectile energy of 50 keV moving through a solid-density vanadium plasma of temperature  $T_e = 30$  eV. Equation (3) plus the equations in this Appendix are valid for electrons that are fast but not highly relativistic. This means that the projectile electron velocity  $v$  must be much higher than a typical electron velocity in the medium but the relativistic quantity  $\gamma$  should not be much greater than 1. For a 50-keV-projectile electron, the velocity  $v_0 = 0.98 \times 10^{10}$  cm/s and  $\gamma \sim 1.1$ . For our case, the fully relativistic formula [Eq. (3) in Ref. 15] differs very little from Eq. (3) above; even at an electron projectile of 250 keV the two differ by only 1.5%. On the other hand,  $v_0$  is much larger than the thermal electron velocity in the medium ( $\sim 4 \times 10^8$  cm/s) and larger than the Fermi velocity

$$(3\pi^2 N_e)^{1/3} / (\hbar/m) \sim 2 \times 10^8 \text{ cm/s.}$$

The slowing-down of electrons due to a plasma can be divided into two contributions: binary collisions and collective collisions (i.e., excitation of plasma waves). In the kinetic formulations of the problem the division between the two regimes is marked by an impact parameter that is smaller or larger than the Debye length  $L_D$ . In the continuum (or dielectric) formulations of the problem the division is marked by a density-modulation wave number  $k$  that is larger or smaller than  $k_D = 1/L_D$ . The effect of plasma ions is negligible for the

high projectile velocities considered here.<sup>20</sup> The addition of the two electron collision terms for high projectile velocities yields<sup>20</sup>

$$(-dE/dx)_{\text{free}} = (2\pi e^4 N_{e,\text{free}}/E_0) \ln(1.52 E_0/\hbar\omega_p), \quad (\text{A2})$$

where  $\omega_p^2 = 4\pi e^2 N_{e,\text{free}}/m$ . It should be noted that the Debye length has cancelled out. This is because the argument of the logarithm in the binary-collision term is  $(L_D/1.47 b_{\text{min}})$ , where  $b$  is the impact parameter, whereas in the collective-collision term it is  $(1.123 v_0/\omega_p L_D)$ , where  $v_0$  is the projectile velocity; thus, by adding the two terms, the Debye length cancels out. This is an indication that the result is independent of the degree of degeneracy, which was also shown directly by Maynard and Deutsch.<sup>21</sup> For small degeneracy and high projectile velocity ( $v_0 \gg v_F$ ) the logarithm in Eq. (A2) is the first term in a series expansion where the second term is given by

$$(kT_e/E_F) \left[ I_{3/2}(\alpha)/I_{1/2}(\alpha) \right] (v_F/v_0)^2, \quad (\text{A3})$$

$I_{3/2}(\alpha)$  and  $I_{1/2}(\alpha)$  being the Fermi integrals. For our case  $(kT_e/E_F) \left[ I_{3/2}(\alpha)/I_{1/2}(\alpha) \right] \sim 1$ , but  $(v_F/v_0)^2 \sim 1.5 \times 10^{-3}$ , making the correction negligible. Likewise Yan *et al.*<sup>22</sup> have shown that when calculating the slowing-down for  $v_0/v_F \gg 1$ , the following effects can be neglected: electron degeneracy, strongly coupled plasma [in which case the random phase approximation implied in Eq. (A2) is invalid], and projectile collisions. In the derivation of Eq. (A3) the substitution  $b_{\text{min}} = \hbar/mv_0$  was made. This is the quantum limit (derived from the uncertainty principle) and is the relevant one for our case since it is a factor of  $\sim 58$  larger than the classical limit given by  $b_{\text{min}} = e^2/mv_0^2$ .

Before adding the relative contributions of free and bound electrons to the projectile slowing-down we modify Eq. (3) because of the Coulomb screening of the bound electrons by the free electrons.<sup>23</sup> In the derivation of Eq. (3) the maximum impact parameter is given by  $b_{\text{max}} \sim \hbar v_0/\langle E_i \rangle$ , where  $\langle E_i \rangle$  is the average ionization energy; however, for our typical values  $b_{\text{max}} \sim 2.5 \text{ \AA}$ , whereas the Debye length (calculated using  $N_{\text{free}}$ ) is  $\sim 1.5 \text{ \AA}$ . Therefore, we have to replace  $b_{\text{max}}$  by  $L_D$ , and Eq. (3) then becomes

$$(-dE/dx)_{\text{bound}} = (2\pi e^4 N_a Z/E_0) \times \ln \left[ (2E_0 kT_e)^{1/2} / \hbar\omega_p \right]. \quad (\text{A4})$$

Here  $\omega_p$  is given again in terms of the density of free electrons. It should be noted that the polarization of the vanadium ions by the projectile electrons and its effect on the slowing-down are significant only for  $\gamma \gg 1$  and can be ignored here.<sup>20</sup> The total slowing-down is given by the sum of Eqs. (A2) and (A4). For the typical conditions considered here the logarithm in Eq. (A2) equals  $\sim 8.2$ , and the logarithm in Eq. (A4) equals  $\sim 4.5$ . Since only  $\sim 10\%$  of the V electrons are free, the former must be multiplied by 0.1, yielding  $\sim 0.8$ . Finally, the sum  $4.5 + 0.8 = 5.3$  should be compared with the value of the logarithm in Eq. (3), which was used above to calculate the preheat, namely  $\sim 5.4$ . Therefore, the modified slowing-down formulation yields results that are essentially the same as those of Eq. (3), so the modifications to Eq. (3) can be neglected.

## REFERENCES

1. N. A. Ebrahim *et al.*, Phys. Rev. Lett. **45**, 1179 (1980); D. M. Villeneuve, R. L. Keck, B. B. Afeyan, W. Seka, and E. A. Williams, Phys. Fluids **27**, 721 (1984).
2. H. Figueroa *et al.*, Phys. Fluids **27**, 1887 (1984); T. A. Peyser *et al.*, Phys. Fluids B **3**, 1479 (1991).
3. T. R. Boehly, R. S. Craxton, T. H. Hinterman, J. H. Kelly, T. J. Kessler, S. A. Kumpan, S. A. Letzring, R. L. McCrory, S. F. B. Morse, W. Seka, S. Skupsky, J. M. Soures, and C. P. Verdon, Rev. Sci. Instrum. **66**, 508 (1995).
4. B. Yaakobi, I. Pelah, and J. Hoose, Phys. Rev. Lett. **37**, 836 (1976); J. D. Hares *et al.*, Phys. Rev. Lett. **42**, 1216 (1979).
5. A. Hauer, W. Priedhorsky, and D. van Hulsteyn, Appl. Opt. **20**, 3477 (1981).
6. M. J. Berger and S. M. Seltzer, Tables of Energy Losses and Ranges of Electrons and Positrons, NASA Document SP-3012, Washington, DC (1964).
7. See National Technical Information Service No. DE83015439 (A. J. Burek and B. Yaakobi, Final Report to the National Bureau of Standards Contract NB81NAHA2032, Appendix A, 1983). Copies may be ordered from the National Technical Information Service, Springfield, VA 22161.
8. B. L. Henke, E. M. Gullikson, and J. C. Davis, At. Data Nucl. Data Tables **54**, 181 (1993).
9. J. V. Gilfrich, D. B. Brown, and P. G. Burkhalter, Appl. Spectrosc. **29**, 322 (1975).
10. P. G. Burkhalter *et al.*, in *X-Ray Calibration: Techniques, Sources, and Detectors*, edited by P. Lee and P. D. Rockett (SPIE, Bellingham, WA, 1986), Vol. 689, pp. 121–127.
11. B. L. Henke *et al.*, J. Opt. Soc. Am. B **3**, 1540 (1986).
12. W. Bambynek *et al.*, Rev. Mod. Phys. **44**, 716 (1972).

13. D. J. Botto, J. McEnnan, and R. H. Pratt, *Phys. Rev. A* **18**, 580 (1978).
14. A. B. Langdon, B. F. Lasinski, and W. L. Kruer, *Phys. Rev. Lett.* **43**, 133 (1979).
15. G. Knop and W. Paul, in *Alpha-, Beta- and Gamma-Ray Spectroscopy*, 1st ed., edited by K. Siegbahn (North-Holland, Amsterdam, 1965), Chap. 1, Vol. 1, p. 12.
16. C. J. Bakker and E. Sergrè, *Phys. Rev.* **81**, 489 (1951); H. H. Andersen and J. F. Ziegler, *Hydrogen Stopping Powers and Ranges in All Elements, The Stopping and Ranges of Ions in Matter*, Vol. 3 (Pergamon Press, New York, 1977).
17. C. J. Powell, *Rev. Mod. Phys.* **48**, 33 (1976).
18. W. Heitler, *The Quantum Theory of Radiation*, 2nd ed., The International Series of Monographs on Physics (Oxford University Press, London, 1947).
19. N. A. Dyson, *X-Rays in Atomic and Nuclear Physics*, 2nd ed. (Cambridge University Press, Cambridge, England, 1990), p. 47.
20. J. D. Jackson, *Classical Electrodynamics*, 2nd ed. (Wiley, New York, 1962), Chap. 13.6.
21. G. Maynard and C. Deutsch, *Phys. Rev. A* **26**, 665 (1982).
22. X.-Z. Yan *et al.*, *Phys. Rev. A* **32**, 1785 (1985).
23. T. A. Mehlhorn, *J. Appl. Phys.* **52**, 6522 (1981).

---

# Holographic Transmission Gratings for Spectral Dispersion

## Introduction

Over the last 12 years, holographic transmission diffraction gratings have been employed within solid-state laser systems to provide angular spectral dispersion (ASD) for laser beam smoothing. The dispersive property of diffraction gratings provides a versatile means to control the spatial and temporal characteristics of high-bandwidth laser light. Recent research has shown that holographic transmission gratings can possess not only high diffraction efficiency and high damage threshold but also high wavefront quality.

In general, spatial or temporal information that is encoded onto a propagating laser beam can be transferred between time and space by means of the lateral time delay associated with a grating's ASD. At LLE, the ASD from a grating is used to carry out laser beam smoothing involving broadband laser operation.<sup>1</sup> At other laser-fusion facilities, holographic diffraction gratings are being developed for broadband frequency conversion to achieve ultra-uniform levels of irradiation uniformity on solid-state laser systems. In addition, several novel pulse compression, pulse expansion, and pulse shaping schemes, involving highly dispersive holographic gratings, have been extensively developed at many laboratories, including LLE.

This article reviews the latest results from our experimental research in holographic-grating fabrication. The performance of recently fabricated holographic gratings is described in terms of diffraction efficiency and wavefront quality. In addition, several important applications of the holographic transmission grating, such as laser beam smoothing on the OMEGA laser system, are reviewed.

## Theoretical Modeling

A periodic thickness variation, or surface relief, formed along one dimension of a photosensitive material, such as photoresist, can deflect an incident laser beam by way of diffraction, as shown in Fig. 82.26. A periodic refractive-index variation within a flat film of material can also act as a diffraction grating. Photorefractive polymers have recently

been modulated to form efficient gratings; however, this will be the subject of a future article. The type of holographic transmission grating that is based on surface relief of a transparent material diffracts light according to the same diffraction-grating equation as pertains to the volume holograms, reflection gratings, and conventionally ruled gratings. The grating equation

$$d[\sin(\theta_d) - \sin(\theta_i)] = m\lambda \quad (1)$$

is used to calculate the angle of diffraction ( $\theta_d$ ) for a wavelength  $\lambda$  when the angle of incidence ( $\theta_i$ ) of the laser beam and the groove spacing  $d$  of the grating are given. This calculation can be performed for any order of diffraction  $m$ ; however, only the first order of diffraction is important for the majority of applications.

The ASD of the grating is defined as the rate of change of the diffraction angle with respect to change in wavelength. The ASD is a measure of the angular spreading of the spectral components of light and is calculated using Eq. (2):

$$\Gamma = m/d \cdot \cos(\theta_d). \quad (2)$$

When used in the symmetric-angle configuration, the angle of the incident laser beam is equal to the angle of the primary diffracted beam, i.e.,  $(\theta_d) = -(\theta_i)$ , where the angles are defined with respect to the plane of the photoresist layer. For this symmetric case, where the lateral magnification between the input beam and the output beam is unity, and  $m$  represents the first order of diffraction, the expressions for the grating equation and angular dispersion become

$$2d \cdot \sin(\theta) = \lambda \quad (3)$$

and

$$\Gamma = 2 \cdot \tan(\theta)/\lambda, \quad (4)$$

respectively. These fundamental grating equations are used to design optical systems with a desired amount of ASD.

An optimum grating design couples as much light as possible to the diffracted laser beam. Figure 82.26 also shows the various paths that can be taken by an incident laser beam. The energy coupled to all additional beam paths is minimized to obtain the highest possible diffraction efficiency, defined as the ratio of the powers of the primary diffracted beam to the incident laser beam. However, even small amounts of energy recirculating within the substrate can cause undesirable temporal modulation. In practice, the grating substrate contains a wedge between the first and second surfaces to prevent secondary beams from propagating coincident with the primary diffracted laser beam.

The diffraction characteristics of the gratings, shown in Fig. 82.26, have been the subject of much research. Several rigorous electromagnetic theories,<sup>2</sup> each based on Maxwell's equations with appropriate boundary conditions, are available to calculate the performance of a diffraction grating. Numerical solutions have been obtained for gratings of arbitrary profiles by the integral-equation and differential-equation methods. The integral method<sup>3</sup> is capable of treating both metallic and dielectric gratings and is often used to benchmark further progress in grating modeling. It has been used with

limited success, however, in modeling deep multilayered gratings that approach a height-to-width ratio near 2 to 1.

Previously, the differential method involved either an orthogonal-mode expansion or a coupled-wave expansion, each containing a large system of equations that were difficult to manage computationally. An improved differential method, however, involving a nonorthogonal coordinate system, was shown to accurately model deep, multilayered, metal and/or dielectric gratings.<sup>4</sup> Most recently, major enhancements were made to this method to allow transmitted orders as well as reflected orders.<sup>5</sup>

The modeling results shown in this article were obtained with a code based on the integral method. Since our experimental results have sometimes exceeded the predicted values for diffraction efficiency from this code, as will be addressed later in this article, an alternate code based on the more recent differential method will be examined in the near future.

### Grating Fabrication

The fabrication of holographic diffraction gratings involves an interferometric exposure of a photosensitive material called photoresist.<sup>6</sup> The holographic interferometer, shown in Fig. 82.27, consists of a laser source, beam-conditioning optics, and two beamlines that intersect at the final recording

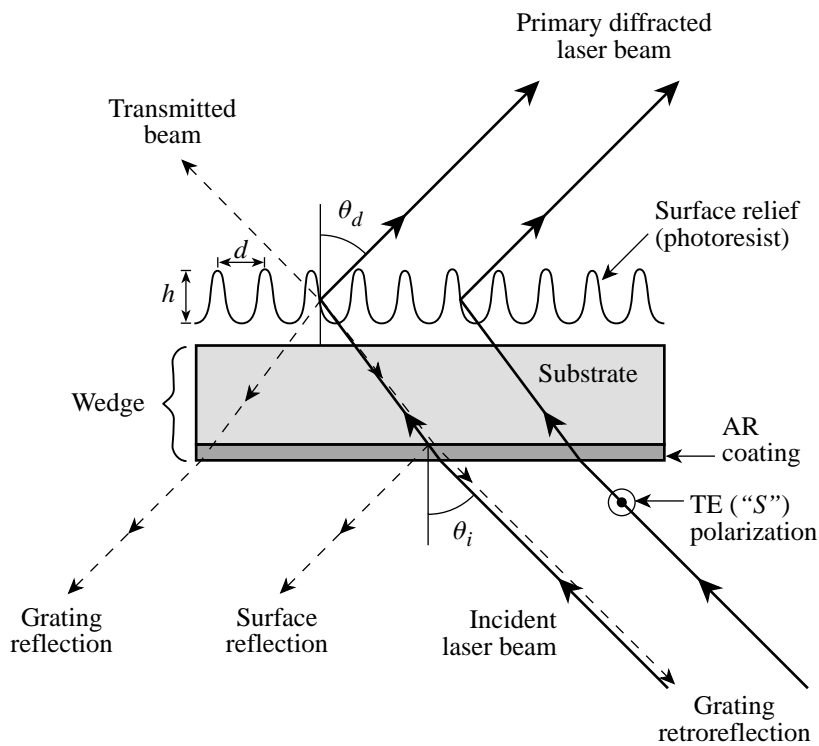


Figure 82.26

A holographic transmission grating, patterned in photoresist, consists of a periodic thickness variation, or surface relief, along one dimension of a material. When used in the symmetric-angle configuration, the angle of the incident laser beam is equal to the angle of the primary diffracted beam, with respect to the plane of the photoresist layer. The energy coupled to all additional beam paths is minimized to obtain the highest-possible diffraction efficiency, defined as the ratio of the powers of the primary diffracted beam to the incident laser beam.

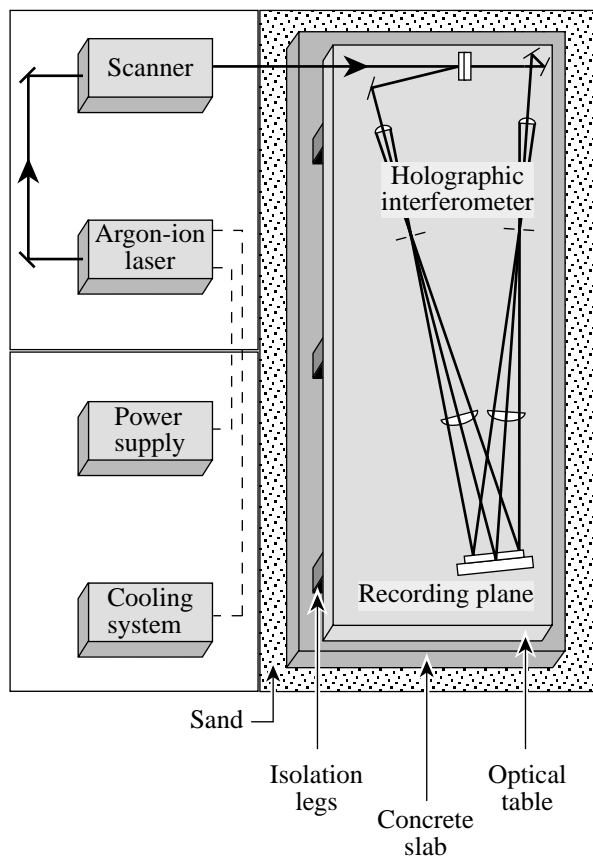
plane. It is used to produce highly visible and stable interference fringes. The laser source is a Spectra-Physics argon-ion laser equipped with an intracavity etalon, narrow-band cavity mirrors, and electronic feedback control to maintain beam power, beam centering, and a single longitudinal mode at the  $\lambda = 364\text{-nm}$  spectral line. Prior to being split into two separate beam paths, the laser beam is raster scanned over the entrance pupils of the two arms of the interferometer. As shown in Fig. 82.28, rotation of a glass cylinder causes a displacement of an incident laser beam without a corresponding change to the laser beam propagation direction. The irradiance at every

point within the clear aperture is the superposition of an array of supergaussian beams, resulting in two-dimensional uniformity. This displacement scanning technique increases the exposure uniformity far beyond that of the laser beam itself.<sup>7</sup> With careful chemical processing, fringe exposure results in deep grooves over the entire clear aperture of the grating.

After exiting the laser scanner, the laser beam is split so that the two arms of the interferometer impose equal amounts of increased path length to an incident beam when the beam is angularly deviated prior to the split. This is the same criterion that was established for the Michelson interferometer,<sup>8</sup> which used an incoherent white-light source. This principle is extended to coherent laser light to achieve stable interference fringes during two-dimensional scanning of the laser beam. To further ensure fringe stability, a 2-ft  $\times$  8-ft  $\times$  16-ft optical table is pneumatically isolated from building vibrations by six pressurized support legs located on a 2-ft-thick concrete slab. This support system rests on a 3-ft mound of dry sand. To isolate the system from sources of acoustic energy, thermal energy, and air turbulence, the interferometer is located in a "room within a room" environment. Furthermore, the laser power supply and cooling system, the laser resonator and scanner, and the holographic interferometer are located in three separate rooms to minimize the transfer of vibrations, heat, and air turbulence.

In practice, however, it has been found that the holographic system performs optimally only after the room air conditioning has been shut down for between 5 to 20 h, depending on the time of the year. The exact time interval appears to depend on the relationship between the temperature of the ground and the temperature of the air supplied by the building's air-conditioning system. Fringe visibility is continuously monitored prior to a series of holographic exposures. The fringe contrast must remain stable for a period of time exceeding the actual duration of the scan. Otherwise, changes in contrast will map directly to low-efficiency regions of the diffraction grating. Extensive testing has revealed that the success or failure of holographic-grating fabrication does not generally depend on the extent of nearby building or ground activity.

A scanning electron microscope (SEM) is used to characterize the surface relief of the holographic gratings. The size and shape of the grooves are shown in Fig. 82.29. In Fig. 82.29(a), close-up examination of the photoresist surface-relief grating shows a groove shape corresponding to 80% diffraction efficiency, where efficiency is defined as the ratio of the diffracted to incident laser power. Although the surface-



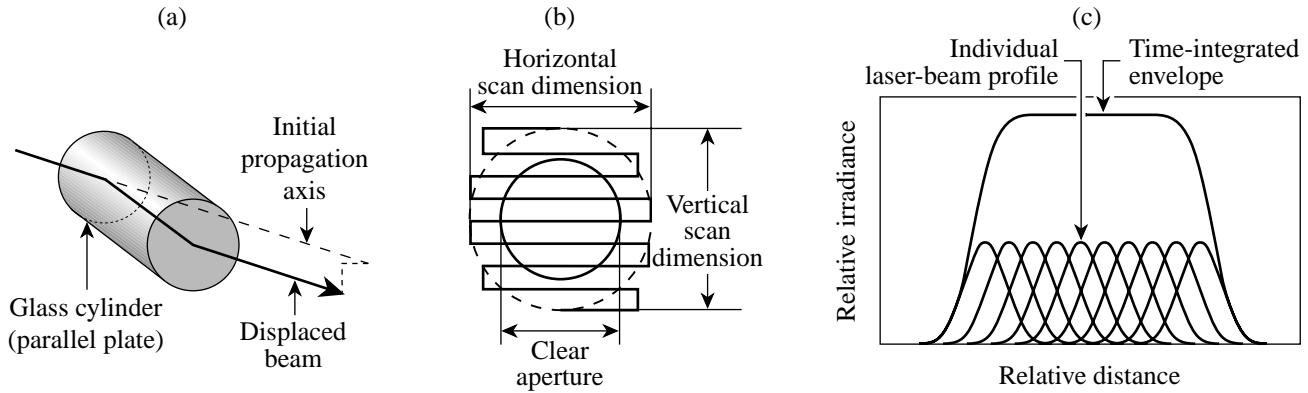
E10348

Figure 82.27

The holographic system consists of a laser source, a laser scanner, and an interferometer with two beamlines that intersect at the final recording plane. It produces high-contrast interference fringes. Fringe stability is achieved through a vibration isolation system containing a 2-ft-thick, 8-ft  $\times$  16-ft optical table, pneumatically floating on six legs and supported by a 2-ft-thick concrete slab, all resting on a foundation of dry sand. The laser power supply and cooling system, the laser resonator and scanner, and the holographic interferometer are located in three separate rooms to minimize the transfer of vibrations, heat, and atmospheric turbulence.

relief profile is not strictly sinusoidal, the etched volume is only slightly larger than the remaining photoresist volume. The SEM in Fig. 82.29(b) shows that the etched volume is much wider than the remaining photoresist volume for a diffraction grating exhibiting over 95% efficiency. The crests of the grooves are straight and rigid when fabricated in controlled laboratory conditions. The SEM in Fig. 82.29(c) reveals the problem associated with uncontrolled humidity in the vicinity of grating fabrication. In the presence of an excessively humid

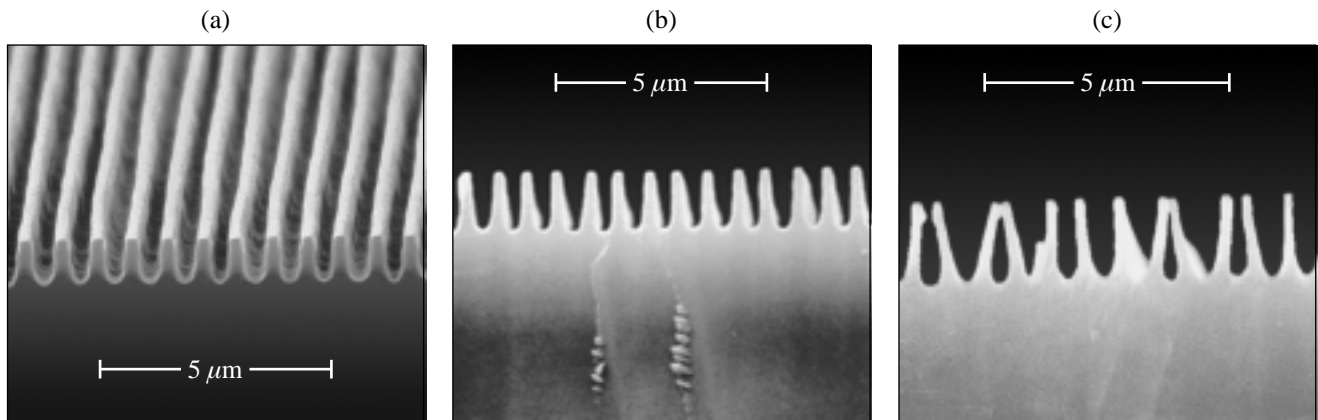
environment, thin walls of photoresist are deformed by capillary attraction from water accumulated within the grooves. It has been observed that groove deformation is accompanied by an increased amount of scatter when probed by a beam of laser light. This is because a distribution of groove deformations acts as a diffuser, scattering light over a broad angular spectrum. Although the mechanical fragility of photoresist structures has long been known, this represents the first time that a specific groove deformation has been associated with the onset



E10349

Figure 82.28

Laser-beam scanning is used to increase the time-integrated irradiation uniformity at the recording plane. (a) A tilted glass cylinder displaces an incident laser beam without angular deflection. (b) The laser beam is raster scanned over the entrance pupils of the two arms of the interferometer. (c) The recording-plane irradiance is the superposition of an array of supergaussian beams. The resulting irradiance is substantially more uniform than the laser beam itself.



E10350

Figure 82.29

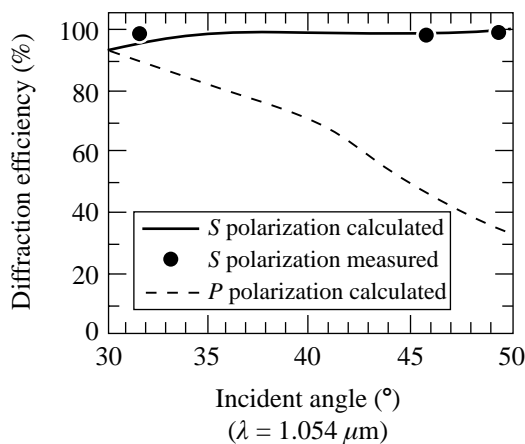
The scanning electron microscope (SEM) provides close-up examination of photoresist gratings. Figure 82.29(a) shows the groove profile corresponding to 80% diffraction efficiency, where efficiency is defined as the ratio of the diffracted to incident laser power. Figure 82.29(b) shows that the etched volume is much wider than the remaining photoresist volume for a diffraction grating exhibiting over 95% efficiency. The crests of the grooves are straight and rigid when fabricated in controlled laboratory conditions. The SEM of Fig. 82.29(c) reveals the problem associated with uncontrolled humidity in the vicinity of grating fabrication. Thin walls of photoresist are deformed by capillary attraction from water accumulated within the grooves. Groove deformation is accompanied by an increased amount of laser light scatter.

of scatter loss. As a result of this understanding, careful washing and drying procedures are used to fabricate super-sinusoidal groove shapes.

### Grating Performance

Holographic transmission gratings possess deep grooves that, when properly shaped, result in near-unity diffraction efficiency for a wide range of groove spacing. Within the holography laboratory at LLE, transmission gratings have been designed and fabricated for use at three different symmetric angles. At the symmetric angle, the incident and diffracted beams have equal angles with respect to the normal to the grating. Theoretical calculations of the diffraction efficiency, shown in Fig. 82.30, predict that performance decreases for gratings with larger groove spacing, i.e., a smaller symmetric angle. Experimental results for these three different symmetric angles indicate, however, that diffraction efficiency can be maintained at a level higher than the integral-equation method predicts. Experimental results for symmetric angles (groove spacings) of  $31.7^\circ$  ( $1.00\ \mu\text{m}$ ),  $46^\circ$  ( $0.73\ \mu\text{m}$ ), and  $49.5^\circ$  ( $0.69\ \mu\text{m}$ ) show that high diffraction efficiency is possible over this entire range of angles.

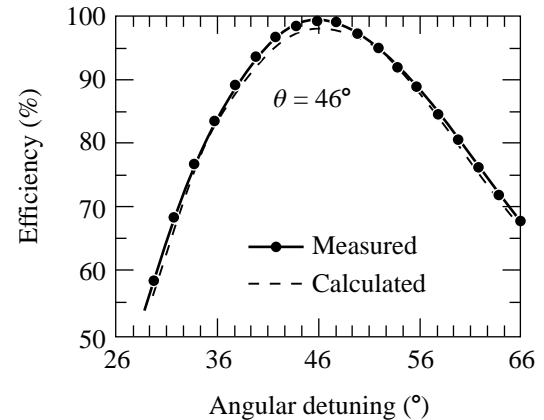
Theoretical and experimental results show that a super-sinusoidal phase grating can exhibit high efficiency. As shown in Fig. 82.31, the diffraction efficiency of a super-sinusoidal



E10351

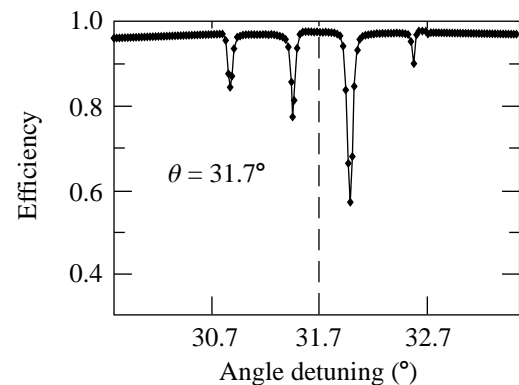
Figure 82.30  
Holographic transmission gratings possess deep grooves that, when properly shaped, result in near-unity diffraction efficiency for a wide range of groove spacing. Theoretical calculations of the diffraction efficiency predict that performance decreases for gratings with a symmetric angle decreasing toward  $30^\circ$ . Experimental results for symmetric angles (groove spacings) of  $31.7^\circ$  ( $1.00\ \mu\text{m}$ ),  $46^\circ$  ( $0.73\ \mu\text{m}$ ), and  $49.5^\circ$  ( $0.69\ \mu\text{m}$ ) show that diffraction efficiency can be maintained over this whole range of angles.

phase grating decreases slowly and monotonically as it is detuned in angle. This curve represents a grating designed for a symmetric angle of  $46^\circ$ ; however, similar performance is obtained for a wide range of angles. As shown in Fig. 82.32, it has been observed that holographic gratings with larger groove spacing, such as the  $31.7^\circ$  grating, exhibit an efficiency profile that drops rapidly at several specific angles when detuned from



E10352

Figure 82.31  
Theoretical and experimental results show that the diffraction efficiency of a typical surface-relief transmission grating decreases slowly and monotonically as it is detuned in angle about the peak efficiency, where the incident and diffracted angles are equal. The curves represent a grating designed for a symmetric angle equaling  $46^\circ$ ; however, similar performance is obtained for a wide range of angles.



E10353

Figure 82.32  
Holographic gratings with larger groove spacing, such as the  $31.7^\circ$  grating, exhibit an efficiency profile that rapidly drops at several specific angles when detuned from the symmetric angle. Except for these narrow regions in angle, the measured diffraction efficiency exceeds theoretical predictions. It is observed that the thickness of the photoresist affects the extent to which laser light travels within the photoresist waveguide before being coupled out along the  $m = -1$  diffraction order.

the symmetric angle. Except for these narrow regions in angle, the measured efficiency exceeds theoretical predictions. A preliminary investigation of this effect revealed that the thickness of the photoresist affects the extent to which laser light propagates down the photoresist waveguide before being coupled out along the first diffraction order. This waveguide-coupling phenomenon has been correlated to the rapid efficiency drop at specific angles. Additional experimental investigation is needed to determine the maximum photoresist thickness allowed before waveguide modes can exist. It has been experimentally determined that efficient use of the  $31.7^\circ$  grating within the OMEGA laser system requires that an alignment error of less than 10 min of arc be maintained between the laser beam and the grating.

Gratings used within the OMEGA laser *must* possess high optical quality, including both high phase-front quality and minimum phase noise. Holographic phase-front errors, due to optical aberrations within the interferometer, can be measured by analyzing interferograms from both the diffracted beam (minus one order) and the transmitted beam (zero order), individually. The wavefront quality of the diffracted beam, however, is what is important for most applications. Better than one-tenth wave performance is achieved over the clear aperture of a grating used for the OMEGA laser system, as shown in Fig. 82.33(a). Cross sections of the wavefront error are shown in Fig. 82.33(b). This error originates from the two telescopes within the interferometer. The difference in curvature between the two cross sections indicates the presence of astigmatism, the aberration which causes the tangential (hori-

zontal) and sagittal (vertical) planes to focus at different planes. In practice, interferometer alignment is repeated until the measured wavefront error is minimized. In addition, small-scale imperfections are reduced by using high-quality optics and coatings within the interferometer, and by carrying out the photoresist deposition in a well-maintained clean-room laboratory.

### Laser Applications

The primary applications of holographic diffraction gratings at LLE involve laser-beam smoothing and spectroscopy. Several sets of gratings, with angular dispersions of between 120 to 220  $\mu\text{rad}$  per angstrom, are now available for one of OMEGA's driver lines for the purpose of laser beam smoothing. Also, high-resolution spectrometers, composed of one or more holographic gratings, are used to characterize the modulation index of phase modulators for broadband beam smoothing. In addition, it is possible that two large-aperture gratings, used in series with a focusing lens, can provide sufficient ASD to fully resolve the individual line structure from a sinusoidally driven modulator. It is important to note that by having holographic gratings incorporated into the driver line of OMEGA, each of the OMEGA beamlines is a potential spectrometer for diagnosis of the laser bandwidth.

A wide variety of additional applications exist for high-efficiency, high-damage-threshold, holographic diffraction gratings. For example, holographic gratings can be used to carry out broadband frequency conversion to achieve ultra-uniform levels of irradiation uniformity on solid-state laser

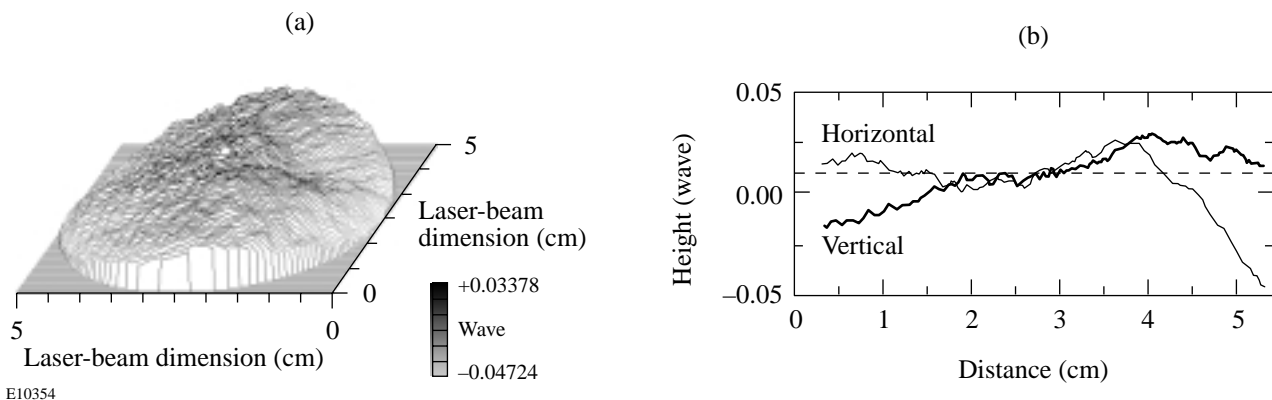


Figure 82.33

(a) Better than one-tenth wave performance is achieved over the clear aperture of a  $31.7^\circ$  grating used in the OMEGA laser system. (b) Cross sections of the wavefront indicate that the largest low-frequency aberration is astigmatism. This error originates from the two telescopes within the interferometer. High-quality optics and mounts can provide similar wavefront quality for large-aperture gratings.

systems. In addition, several novel pulse-compression and pulse-expansion schemes include holographic gratings in their optical design. Advanced pulse-shaping schemes also involve highly dispersive holographic gratings, which provide compactness, high damage threshold, and high diffraction efficiency. Holographic transmission gratings are used within compact spectrometers, fiber-optic couplers, laser scanners, and various semiconductor lasers. Additional applications of high-power, high-dispersion transmission gratings involve their function as a spectral filter. These gratings provide excellent Fourier-blocking capability for small-signal-gain detection and for the suppression of amplified stimulated emission in amplifier chains. It is anticipated that many new applications will be found for holographic transmission gratings when the gratings become more widely available.

### Conclusion

Holographic transmission gratings that possess high diffraction efficiency, high wavefront quality, and high damage threshold have been designed, fabricated, and characterized for use within high-power, solid-state laser systems. Holography research has resulted in diffraction gratings that exhibit near-unity efficiency over a wide range of groove spacing. A novel interferometric technique that incorporates laser beam scanning is now routinely used to obtain uniform grating irradiation while maintaining stable, high-contrast, interference fringes. Over 100 gratings, covering a wide range of groove spacing, have been manufactured with this interferometric exposure technique. Several sets of gratings, with different amounts of angular dispersion, are available for one of the driver lines of the OMEGA laser. Numerous applications exist for these high-efficiency, high-damage-threshold holographic gratings. Laser beam smoothing and spectroscopic techniques, many of which have been invented and developed at LLE, incorporate these gratings. High-efficiency and high-wavefront-quality gratings are now in use within the beam-smoothing driver line of the OMEGA laser system. The current research thrust involves an experimental and theoretical investigation of the gratings that exhibit diffraction efficiency that exceeds code predictions and also exhibit waveguide coupling of laser light.

### ACKNOWLEDGMENT

This work was supported by the U.S. Department of Energy Office of Inertial Confinement Fusion under Cooperative Agreement No. DE-FC03-92SF19460, the University of Rochester, and the New York State Energy Research and Development Authority. The support of DOE does not constitute an endorsement by DOE of the views expressed in this article.

### REFERENCES:

1. Laboratory for Laser Energetics LLE Review **37**, 40, NTIS document No. DOE/DP/40200-83 (1988). Copies may be obtained from the National Technical Information Service, Springfield, VA 22161.
2. R. Petit, ed. *A Tutorial Introduction*, Electromagnetic Theory of Gratings (Springer-Verlag, Berlin, 1980).
3. D. Maystre, *J. Opt. Soc. Am.* **68**, 490 (1978).
4. J. Chandezon *et al.*, *J. Opt. Soc. Am.* **72**, 839 (1982).
5. L. Li, "DELTA: A Computer Program for Multilayer-Coated Gratings in Conical Mountings," computer manual (1999).
6. Laboratory for Laser Energetics LLE Review **50**, 61, NTIS document No. DOE/DP/40200-197 (1992). Copies may be obtained from the National Technical Information Service, Springfield, VA 22161.
7. J. J. Armstrong and T. J. Kessler, in *Laser Coherence Control: Technology and Applications*, edited by H. T. Powell and T. J. Kessler (SPIE, Bellingham, WA, 1993), Vol. 1870, pp. 47-52.
8. A. A. Michelson, *Am. J. Sci.* **22**, 120 (1881).

---

# Laser Beam Smoothing Caused by the Small-Spatial-Scale $B$ -Integral

## Introduction

Target irradiation uniformity is an important aspect of the direct-drive approach to inertial confinement fusion (ICF),<sup>1,2</sup> where the capsule is directly irradiated by a symmetrically arranged cluster of high-intensity, ultraviolet (UV) laser beams. Nonuniformity in laser irradiation seeds the Rayleigh–Taylor hydrodynamic instability, which consequently degrades target performance.<sup>3,4</sup> Various techniques are employed on the OMEGA<sup>5</sup> laser to improve the on-target irradiation uniformity to reduce laser imprint: two-dimensional smoothing by spectral dispersion (2-D SSD),<sup>6–8</sup> distributed phase plates (DPP's),<sup>9,10</sup> polarization smoothing (DPR's),<sup>5,11,12</sup> and multiple-beam overlap. A complete understanding of the laser focal-spot dynamics is essential to ICF performance, and it provides valuable feedback as a laser diagnostic tool. In Ref. 13, the smoothing rate of 2-D SSD on OMEGA was investigated both experimentally and numerically. Excellent agreement between the experimental results and the corresponding simulations was found for all 2-D SSD cases and for low-energy shots without applied frequency modulation (FM) (i.e., without SSD). Laser beam smoothing of high-power glass lasers caused by small-spatial-scale and whole-beam  $B$ -integral effects with DPP's and no applied FM is examined in this article.

In the absence of externally applied FM, the beam can acquire bandwidth because of the time-dependent  $B$ -integral (Ref. 14, p. 385) acquired in the laser chain. The phase difference between a wave traveling in a vacuum and a wave propagating a distance  $L$  in a nonlinear medium in the  $z$  direction can be expressed as

$$\Delta\phi = \frac{2\pi(n_0 - 1)L}{\lambda_0} + \phi_B(z),$$

where  $\lambda_0$  is the vacuum wavelength,  $n_0$  is the linear index of refraction, and  $B$  is the intensity dependent phase given by

$$\phi_B(z) = \frac{2\pi}{\lambda} \int_0^L \gamma I(z) dz,$$

where  $\gamma$  is the nonlinear constant of the medium and  $I(z)$  is the intensity (compare Ref. 15). In the event that the  $B$ -integral is nonuniform in space and time, it will cause the speckle pattern produced by the DPP to move in the target plane, similar to the effect of SSD. In the absence of a smoothing mechanism such as SSD, the nonuniformity of the measured far fields with DPP's is expected to have an rms value of 100%, reflecting the high contrast of the speckle pattern produced by the presumed coherent illumination of the DPP. Experimental far-field measurements, however, acquired on OMEGA with the ultraviolet-equivalent-target-plane (UVETP) diagnostic of high-energy shots without applied FM yielded smoothed far fields with overall nonuniformity ranging from 62% to 88%.<sup>13</sup> The nonuniformity decreases approximately linearly with increasing average intensity. The amount of smoothing provided by  $B$ -integral effects alone is not sufficient for direct-drive ICF.<sup>7</sup> However, shots without applied FM are base-line measurements for the high-intensity SSD shots and are therefore studied in this article.

The dominant smoothing mechanism in pulses without externally applied FM is attributed to the small-spatial-scale  $B$ -integral variation, which possesses sufficient temporal bandwidth and beam divergence to affect OMEGA target spherical-harmonic modes as small as  $\ell \sim 40$  or wavelengths as long as  $\lambda_{\text{mode}} \sim 80 \mu\text{m}$  ( $\ell$  modes are related to wavelength by  $\ell \equiv 2\pi r/\lambda_{\text{mode}}$ , where  $r=0.5 \text{ mm}$  is the target radius). The small-spatial-scale  $B$ -integral results from intensity nonuniformities as the laser beam propagates through a nonlinear medium, such as amplifier glass, and produces amplitude and phase modulations in the beam (see Ref. 14, p. 381). This effect introduces time-dependent phase variations across the beam, which results in some smoothing of the speckle structure when the beam, without externally applied FM, passes through a DPP and is focused onto the target. The whole-beam  $B$ -integral affects smoothing to a smaller degree and is produced as the whole beam self-focuses (see Ref. 14, p. 380). The *RAINBOW* code (compare Ref. 15, p. 229) calculates the whole-beam  $B$ -integral for the pulse shapes used on OMEGA as a function of radius and time. It is shown later in the **Laser Beam**

**Smoothing** section that the whole-beam  $B$ -integral produces only a small portion of the observed smoothing because of its small temporal bandwidth coupled to the fact that its imposed laser divergence does not change substantially over time. As a result, the spatiotemporal evolution of the whole-beam  $B$ -integral is not sufficient to cause rapid movement of the speckle pattern in the far field. The whole-beam  $B$ -integral changes the on-target focal-spot diameter and shape by a small amount.

The transverse spatial-intensity profile of the near field evolves slowly in time from a center-peaked beam to an edge-peaked beam as a result of gain saturation effects. The highest far-field spatial frequencies produced by coherent illumination of the DPP are caused by the interference from the outer edges of the beam. Consequently, as the effective beam radius increases in time, the energy in the highest spatial frequencies increases. The effective radius of the fluence accurately yields the overall high-frequency cutoff.

The code *Waasikwa*<sup>\*</sup> was developed to simulate the planar, time-integrated far fields produced by the OMEGA laser, which allows a direct comparison of the calculations to the images acquired by the UVETP diagnostic. *Waasikwa* is a general-purpose simulation program that has the capability to model far fields under a variety of near-field conditions: arbitrary spatial envelopes that possess an arbitrary temporal envelope at any transverse point; whole-beam and small-spatial-scale  $B$ -integral near-field phase; 2-D SSD; arbitrary static phase aberrations; DPR's; the inherent bandpass characteristic of frequency conversion; and multiple-beam overlap. *Waasikwa* utilizes the continuous DPP employed on OMEGA. In addition, it can be configured to run within a shared-memory model as a multiprocessing task on a parallel machine such as the SGI Origin 2000.<sup>16</sup>

The following sections describe far-field simulation and analysis, experimental results, simulation results, and conclusions.

### Far-Field Simulation and Analysis

*Waasikwa* calculates the far-field fluence using

$$F(x_{\text{ff}}, y_{\text{ff}}) \equiv \int_{\text{pulse duration}} I_{\text{ff}}(x_{\text{ff}}, y_{\text{ff}}, t) dt, \quad (1)$$

<sup>\*</sup>An Anishinaabe word meaning "polishes it" as in smoothing a rough surface. Resource: J. Nichols and E. Nyholm, eds. *Ojibwewi-ikidowinan and Ojibwe Word Resource Book*, Occasional Publications in Minnesota Anthropology, No. 7 (Minnesota Archaeological Society, St. Paul, MN, 1979).

where  $I_{\text{ff}}(x_{\text{ff}}, y_{\text{ff}}, t)$  represents the instantaneous far-field intensity. The evolution of the far-field intensity is calculated by taking the modulus squared of a two-dimensional spatial Fourier transform of the UV near field (compare Goodman, Ref. 17, p. 83),

$$I_{\text{ff}}(x_{\text{ff}}, y_{\text{ff}}, t) \equiv \left| \iint_{\text{space}} E(x, y, t) e^{-i \frac{2\pi}{\lambda_{\text{UV}} f_{\Omega}} (x_{\text{ff}} x + y_{\text{ff}} y)} dx dy \right|^2, \quad (2)$$

where  $E(x, y, t)$  represents the complex-valued UV electric field strength in the near field and  $(x, y)$  and  $(x_{\text{ff}}, y_{\text{ff}})$  are the near- and far-field coordinate systems, respectively;  $\lambda_{\text{UV}} = 351$  nm is the UV vacuum wavelength; and  $f_{\Omega} = 180$  cm is the focal length of the OMEGA focusing lens. The spatiotemporal evolution of the complex-valued UV electric field can be expressed as

$$E(x, y, t) \equiv E_0(x, y, t) e^{i\phi_B(x, y, t)} e^{i\phi_{\text{DPP}}(x, y)}, \quad (3)$$

where  $E_0(x, y, t)$  defines the electric field envelope of the pulsed beam;  $\phi_B(x, y, t)$  represents the combined phase contributions of the whole-beam and small-spatial-scale intensity-dependent  $B$ -integral; and  $\phi_{\text{DPP}}(x, y)$  is the static DPP phase-plate contribution whose mapping to the far field depends on its design. During OMEGA laser shots, the near fields of the 1- to 3-ns square pulses evolve from a center-peaked to an edge-peaked spatial-intensity profile. The near field of a 100-ps pulse, however, remains center peaked for the duration of the pulse. The spatiotemporal evolutions of both the Gaussian and square pulses are calculated with *RAINBOW* and are used as inputs to the *Waasikwa* simulations. The equivalent near-field radius and pulse width are useful for calculating the average intensity and are defined as (see discussion of equivalent widths in Ref. 18, p. 148)

$$r_{\text{eq}} \equiv \frac{1}{F_{\text{nf}}(0)} \int_0^{\infty} F_{\text{nf}}(r) dr \quad (4)$$

and

$$t_{\text{eq}} \equiv \frac{1}{P(t_c)} \int_0^{\infty} P(t) dt, \quad (5)$$

respectively, where the near-field fluence is defined by

$$F_{\text{nf}}(r) \equiv \int_{\forall t} |E_0(r, t)|^2 dt,$$

the near-field power is defined by

$$P(t) \equiv 2\pi \int_0^{\infty} r |E_0(r, t)|^2 dr,$$

and the pulse centroid is given by

$$t_c = \frac{\int_{-\infty}^{\infty} tP(t) dt}{\int_{-\infty}^{\infty} P(t) dt}.$$

It has been assumed that, for these calculations, the beam profile is azimuthally symmetric so that the spatial energy centroid is always located at  $r = 0$ . The equivalent widths permit a comparison of the shorter, 100-ps pulses (which have a center-peaked beam profile and a Gaussian pulse shape) to the longer pulses (which are, on the average, nearly square in space and time).

The 2-D power spectral density (2-D power spectrum or simply the 2-D psd) is derived from either the measured or simulated far-field fluences by taking the modulus squared of the 2-D spatial Fourier transform, namely,

$$\text{PSD}(k_{x_{\text{ff}}}, k_{y_{\text{ff}}}) \equiv \left| \iint_{\forall \text{ far field}} F(x_{\text{ff}}, y_{\text{ff}}) e^{-i(k_{x_{\text{ff}}} x_{\text{ff}} + k_{y_{\text{ff}}} y_{\text{ff}})} dx_{\text{ff}} dy_{\text{ff}} \right|^2, \quad (6)$$

where  $F(x_{\text{ff}}, y_{\text{ff}})$  represents the far-field fluence as defined by Eq. (1),  $(x_{\text{ff}}, y_{\text{ff}})$  is the far-field coordinate system, and  $(k_{x_{\text{ff}}}, k_{y_{\text{ff}}})$  is the far field's spatial-frequency coordinate system. The azimuthal sum at each radial wave number of the 2-D power spectrum defines the 1-D power spectral density (1-D power spectrum or simply the 1-D psd) and is given by

$$\text{psd}(k_{\text{ff}}) \equiv \oint \text{PSD}(k_{x_{\text{ff}}}, k_{y_{\text{ff}}}) k_{\text{ff}} d\theta, \quad (7)$$

where the transformation into polar coordinates is defined as  $k_{\text{ff}} \equiv \sqrt{k_{x_{\text{ff}}}^2 + k_{y_{\text{ff}}}^2}$  and  $\tan \theta \equiv k_{y_{\text{ff}}}/k_{x_{\text{ff}}}$ . The single-beam irradiation nonuniformity  $\sigma_{\text{rms}}$  is defined as the square root of the ratio of the speckle power [e.g., the high frequencies  $k_{\text{ff}} \geq 0.04$  (rad/ $\mu\text{m}$ ) at the OMEGA target plane or  $\ell$  modes with  $\ell \geq 20$ ] to the envelope power of the far-field spot [i.e., the low frequencies  $k_{\text{ff}} < 0.04$  (rad/ $\mu\text{m}$ )]. The envelope/speckle dividing-line wave number of 0.04 (rad/ $\mu\text{m}$ ) represents the lowest spatial frequency that is smoothed by 2-D SSD, as discussed in Ref. 13. A finite entrance pupil imposes a limitation on the spatial-frequency bandwidth of an optical system (compare the intensity-impulse response or point-spread function of a diffraction-limited system with a circular exit-pupil function in Ref. 17, p. 110). On OMEGA, the highest spatial frequency of the laser speckle (or interference pattern) is limited by the finite diameter of the serrated apodizer, regardless of the beam profile. The OMEGA entrance pupil is defined by the diameter of the serrated aperture, which is located near the end of the laser driver section on OMEGA. The entrance pupil is imaged to the end of OMEGA and sets the final exit pupil to a full-system diameter  $D_{\Omega} = 27.5$  cm. Consequently, the power spectrum possesses an absolute cutoff wave number that corresponds to the  $f$ -number limited spatial frequency

$$k_{\text{cut}_{\text{ff}}} = \frac{2\pi}{1.22} \frac{D_{\Omega}}{\lambda_{\text{UV}} f_{\Omega}} = 2.24 \left[ \frac{\text{rad}}{\mu\text{m}} \right]$$

and corresponds to  $\lambda_{\text{mode}_{\text{cut}}} = 280 \mu\text{m}$ .

Experimental constraints restrict the analysis to the central portion of the laser beam. Consequently, data windowing must be employed to accurately analyze the PSD of the data. Otherwise, when the 2-D PSD is calculated, the result contains Fourier artifacts of the cropping function convolved with the desired underlying power spectrum of the far field. A 2-D generalization of the common Hamming (the Hamming function does not go to zero like the similar Hanning function)<sup>19</sup> windowing function is employed:

$$\begin{aligned} & \text{SQHamming}(x_{\text{ff}}, y_{\text{ff}}) \\ & \equiv \text{Hamming}(x_{\text{ff}}) \cdot \text{Hamming}(y_{\text{ff}}). \end{aligned} \quad (8)$$

## Experimental Results

A full description of the CCD-based UVETP diagnostic can be found in Ref. 13. An example of an acquired image of a 300-J, 3.5-ns shot with no applied FM is presented in

Fig. 82.34, where a lineout through the center of the beam is overplotted to show the highly modulated intensity. The laser-beam focus is centered nominally on the photodetector, and a 584- $\mu\text{m}$  central portion of the whole 950- $\mu\text{m}$  far-field spot (defined as the 95% enclosed energy contour) is captured on a  $1024 \times 1024$ -pixel grid. However, experimental variances of the far-field centroid require that the image be cropped to guarantee a consistent area for all shot data; a  $720 \times 720$ -pixel portion around the far-field centroid yields a  $411 \times 411\text{-}\mu\text{m}^2$  area of the original image for analysis.

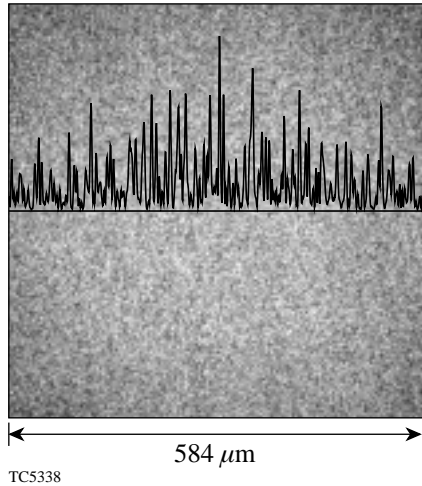


Figure 82.34

UVETP sampled far-field spot demonstrating the 46 $\times$ , high-magnification setup. The image represents a 300-J, 3.5-ns square laser pulse without applied FM. As demonstrated with the single-pixel lineout through the center of the beam, the spot possesses a highly modulated intensity profile. The laser beam focus is centered nominally on the photodetector, and a 584- $\mu\text{m}$  central portion of the whole 950- $\mu\text{m}$  far-field spot (defined as the 95% enclosed energy contour) is captured on a  $1024 \times 1024$ -pixel grid.

*Waasikwa*' simulations use a different scale that samples the majority of the far-field spot to avoid aliasing effects from the Fourier transforms in Eq. (2). The far-field spot is calculated over a  $1024 \times 1024$ -pixel grid that spans a  $993 \times 993\text{-}\mu\text{m}^2$  area. The speckle structure is resolved by surrounding the DPP data (defined as a  $512 \times 512$ -pixel grid covering  $32.6 \times 32.6\text{-cm}^2$  area) with a zero buffer of 256 pixels on each side, forming a total near-field grid of  $1024 \times 1024$  pixels. For a direct comparison of power spectra, the simulated far fields are cropped to match the area of the cropped UVETP images so that they span  $424 \times 424$  pixels or a  $411 \times 411\text{-}\mu\text{m}^2$  area. Consequently, the power spectrum frequency spacing for either the measurement or simulation is equivalent, i.e.,  $dk_{\text{ff}} = 0.0153$  (rad/ $\mu\text{m}$ ), because the total sampled area of the

far field dictates the discrete Fourier domain spacing of the power spectrum.

The aforementioned configurations are used for all of the UVETP images and *Waasikwa*' simulations presented in this article. A 1-D power spectrum is calculated for each measured UVETP image and *Waasikwa*' simulation using the square Hamming window. The analysis results for all of the measured and simulated far fields discussed here are compiled in Table 82.IV.

The measured nonuniformity for the high- and low-energy shots without applied FM decreases approximately linearly with increasing average near-field intensity. This trend is illustrated in Fig. 82.35, where the average near-field intensity is given by

$$I_{\text{avg}} \equiv \frac{U_{\text{shot}}}{t_{\text{eq}} \cdot \pi \cdot r_{\text{eq}}^2}, \quad (9)$$

where  $U_{\text{shot}}$  is the measured shot energy, the equivalent radius  $r_{\text{eq}}$  was defined in Eq. (4), and the equivalent pulse width  $t_{\text{eq}}$  was defined in Eq. (5). These values are tabulated in Table 82.IV for different pulse widths and energies. When the average near-field intensity is increased, both the small-spatial-scale and whole-beam *B*-integrals grow (since the small-

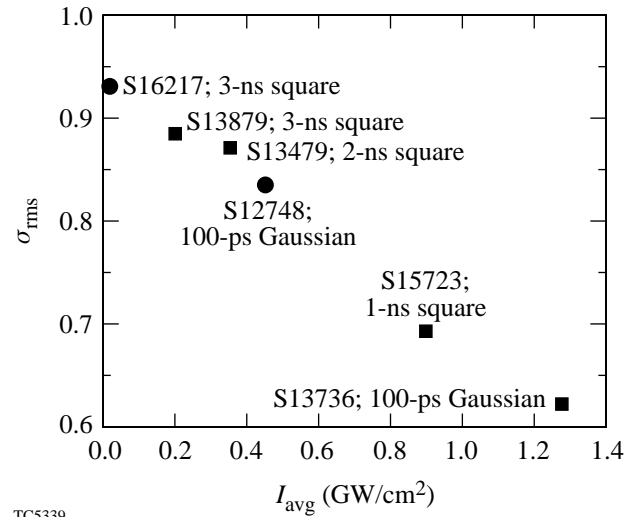


Figure 82.35

The nonuniformity as a function of average intensity for low- and high-energy versions of the pulse shapes. This figure illustrates the trend in the nonuniformity of UVETP images as a function of various pulse shapes and energies. The squares (■) represent the high-energy shots, and the circles (●) correspond to the low-energy counterparts. The points are labeled with the OMEGA shot numbers. Note the suppressed zero.

spatial-scale  $B$ -integral scales with the whole-beam  $B$ -integral), which in turn results in a lower measured value of  $\sigma_{\text{rms}}$ . For example, the peak whole-beam  $B$ -integral calculated for the 12.5-J, 100-ps Gaussian pulse increased from 4.64 rad to 9.99 rad (see Table 82.IV) when the energy of the 100-ps pulse was increased by a factor of 3, and the measured  $\sigma_{\text{rms}}$  decreased from 83.4% to 62.3%.

Power spectra of measured UVETP images are overplotted in Fig. 82.36 for three types of OMEGA shots without applied FM: a low-energy, 3-ns square pulse is overplotted with a high-energy, 100-ps Gaussian pulse in Fig. 82.36(a) and the same low-energy pulse is overplotted with a high-energy, 1-ns square pulse in Fig. 82.36(b). These spectra represent the three distinct types measured for no-FM pulses. The low-energy, 3-ns

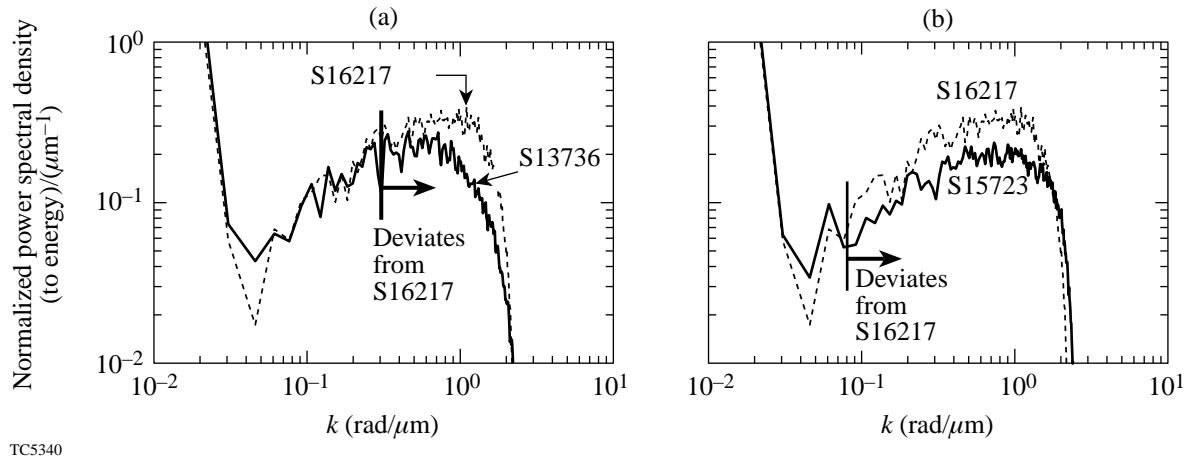


Figure 82.36

The 1-D power spectrum of UVETP images for (a) low-energy, 3-ns square (shot 16217; dashed line) and 100-ps Gaussian (shot 13736; solid black line) shots and (b) low-energy, 3-ns square (shot 16217; dashed line) and high-energy 1-ns square (shot 15723; solid black line). The low-energy shot was 5 J and represents the expected spectrum for shots without applied FM. The high-energy shots were 508 J and 40 J, respectively, and illustrate the smoothing effects of whole-beam and small-spatial-scale  $B$ -integrals in the regions indicated where the spectral power has been reduced relative to the low-energy shot.

Table 82.IV: Far-field analysis results from typical UVETP images and the *Waasikwa'* simulations that match the near-field conditions for a variety of pulse shapes and energies. A square-Hamming window shape was used. The UVETP image was cropped to span  $720 \times 720$  pixels and covers  $0.411 \times 0.411$  mm. The *Waasikwa'* simulation was cropped to match the area of the UVETP image so that it spans  $424 \times 424$  pixels. Note that this yields identical speckle-frequency spacing of  $dk_{\text{ff}} = 0.0153$  (rad/ $\mu\text{m}$ ) for the measurement and simulation.

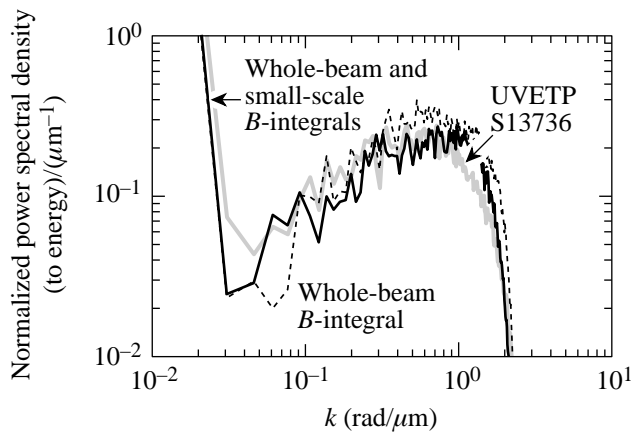
Shot Number	Nominal Pulse Width	Output-Pulse Shape	UV Beam Energy (J)	<i>RAINBOW</i> Calculated $r_{\text{eq}}$ (cm)	<i>RAINBOW</i> Calculated $t_{\text{eq}}$ (ns)	<i>RAINBOW</i> Peak Whole-Beam $B$ -Integral (radians)	UVETP $\sigma_{\text{rms}}$ (%)	<i>Waasikwa'</i> $\sigma_{\text{rms}}$ (%) Whole-Beam $B$ -Integral	<i>Waasikwa'</i> $\sigma_{\text{rms}}$ (%) Whole-Beam and Small-Spatial-Scale $B$ -Integrals
S12748	100 ps	Gaussian	12.5	7.76	0.126	4.64	83±0.5	96.3	94.1
S13736	100 ps	Gaussian	40	8.53	0.116	9.99	62±3	86.2	67.0
S15723	1 ns	square	508	12.6	0.964	20.0	69±5	95.2	69.9
S13479	2 ns	square	370	12.4	1.86	11.1	87±3	96.4	86.5
S16217	3 ns	square	6.6	7.09	2.98	0.970	93±1	98.0	98.9
S13879	3 ns	square	331	12.4	2.880	7.58	88±1	97.7	88.6

square shot without applied FM has a measured nonuniformity  $\sigma_{\text{rms}} = 93\%$  near the 100% modulation expected for a DPP without  $B$ -integral effects. The high-energy shots exhibit nonuniformity values  $\sigma_{\text{rms}}$  from 62% to 88%. The 1-D power spectra of the 100-ps Gaussian high-energy shot deviate from the theoretical low-energy case over the spatial-frequency range  $k_{\text{ff}} > 0.3(\text{rad}/\mu\text{m})$ , as seen in Fig. 82.36(a), which corresponds to  $\ell > 150$  and a full-angle near-field laser divergence of about  $12 \mu\text{rad}$ . This pulse has insufficient time to smooth lower spatial frequencies. Conversely, the 1-D power spectra of the high-energy, 1-ns square shot deviates over a larger spatial-frequency range  $k_{\text{ff}} > 0.08(\text{rad}/\mu\text{m})$  ( $\ell > 40$ ), as seen in Fig. 82.36(b), even though this pulse has a lower average intensity and higher nonuniformity. For both cases, the deviation from the low-energy spectrum becomes significant, i.e., a ratio greater than about  $\sqrt{2}$  for  $k_{\text{ff}} > 0.7 (\text{rad}/\mu\text{m})$  ( $\ell > 350$ ), which corresponds to a full-angle, near-field laser divergence of about  $4 \mu\text{rad}$ . The other two high-energy square pulses, given in Table 82.IV, exhibit power spectra characteristics similar to the 1-ns case except that the power spectra show less deviation from the low-energy spectrum.

A comparison of the power spectra for the experimental measurements and the simulations demonstrates the smoothing effect of the small-spatial-scale and whole-beam  $B$ -integrals. The details of the  $B$ -integral modeling are given in the **Laser Beam Smoothing** section. The power spectra of the UVETP images are shown in Fig. 82.37 through Fig. 82.40 (as

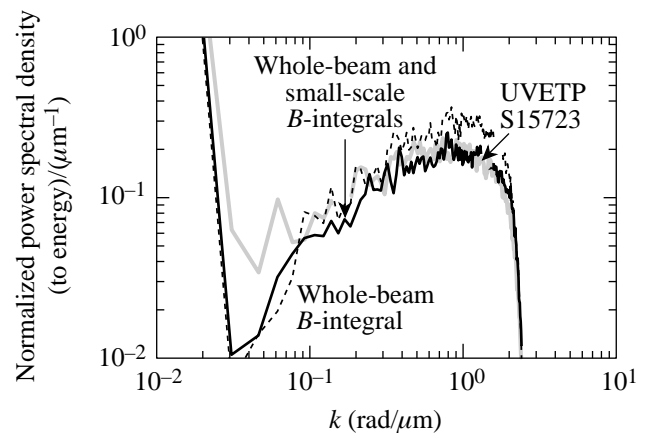
solid gray lines) for the 100-ps, 1-ns, 2-ns, and 3-ns pulses with no FM, respectively. The figures include the resultant 1-D power spectra from corresponding *Waasikwa* simulations that include only whole-beam  $B$ -integral and both small-spatial-scale and whole-beam  $B$ -integral effects. Each power spectrum is normalized to the spectral energy of the 1-D power spectrum. The measured  $\sigma_{\text{rms}}$  is the lowest for the 100-ps pulse at 62.3% and increases with increasing pulse length up to 88.4% for the 3-ns pulse. The values of the nonuniformity  $\sigma_{\text{rms}}$  for all the UVETP images are summarized in Table 82.IV. The UVETP diagnostic was configured with a Gaussian-like DPP, which is fabricated to produce a far-field spot with an  $N = 2.5$  super-Gaussian spatial-intensity envelope, for all of the shots except the 3-ns pulse. A higher-order DPP, which is fabricated to produce a far-field spot with an  $N = 6.5$  super-Gaussian spatial-intensity envelope, was installed for the 3-ns pulse. The spatial-intensity envelope of the far field determines the low-wave-number power spectrum but does not significantly affect the large-wave-number power spectrum. The data windowing occludes the low-wave-number power spectra differences between the two DPP designs.

Simulations of the power spectra demonstrate that temporally varying local phase distortions in the beam caused by small-spatial-scale and whole-beam  $B$ -integral effects in the laser decrease the nonuniformity to levels that match the experimental results in pulses with no applied FM. The theoretical predictions of the models that include both of the



TC5341

Figure 82.37 The 1-D power spectrum of a UVETP image of a 100-ps Gaussian pulse (shot 13736; solid gray line) and the corresponding *Waasikwa*’ simulation including only whole-beam  $B$ -integral effects (dashed line) and both small-spatial-scale and whole-beam  $B$ -integral effects (solid black line).



TC5342

Figure 82.38 The 1-D power spectrum of a UVETP image of a 1-ns square pulse (shot 15723; solid gray line) and the corresponding *Waasikwa*’ simulation including only whole-beam  $B$ -integral effects (dashed line) and both small-spatial-scale and whole-beam  $B$ -integral effects (solid black line).

*B*-integral effects are in excellent agreement with the measured power spectra for the 1-ns, 2-ns, and 3-ns square pulses over the range of  $k_{\text{ff}} > 0.1 \text{ rad}/\mu\text{m}$ . There is a slight discrepancy for the combined *B*-integral model due to excess smoothing over the range of  $0.1 < k_{\text{ff}} < 0.3 \text{ rad}/\mu\text{m}$ . The 100-ps Gaussian simulations are limited by the near-field measurements as described in the next section. The impact of the small-spatial-scale *B*-integral effects (solid black line) on the power spectrum is evident in Figs. 82.37–82.40, where the simulations (dashed line) that model the whole-beam *B*-integral effects but neglect the small-spatial-scale *B*-integral effects are shown. The effects of the whole-beam *B*-integral reduce the  $\sigma_{\text{rms}}$  to a level of 86.2% and 95.2% for the 100-ps and 1-ns high-energy pulses, respectively, which does not match the experimental results with  $\sigma_{\text{rms}} = 62\%$  for the 100-ps pulse and  $\sigma_{\text{rms}} = 69.3\%$  for the 1-ns pulse. The combined effects of the whole-beam and small-spatial-scale *B*-integrals, however, reduce the  $\sigma_{\text{rms}}$  to a level of 67.0% and 69.9% for the 100-ps and 1-ns high-energy pulses, respectively, which is comparable to the experimental values. The values of the nonuniformity  $\sigma_{\text{rms}}$  for all the *Waasikwa*' simulations are summarized in Table 82.IV.

### Laser Beam Smoothing

Smoothing in the far field occurs when the state of the transverse phase front of the near field, given by  $\phi(x,y,t)$ , changes as a function of time such that the spatial coherence is altered. For a particular instant in time, a state  $\phi(x,y,t)$  will produce a unique speckle pattern in accordance with the

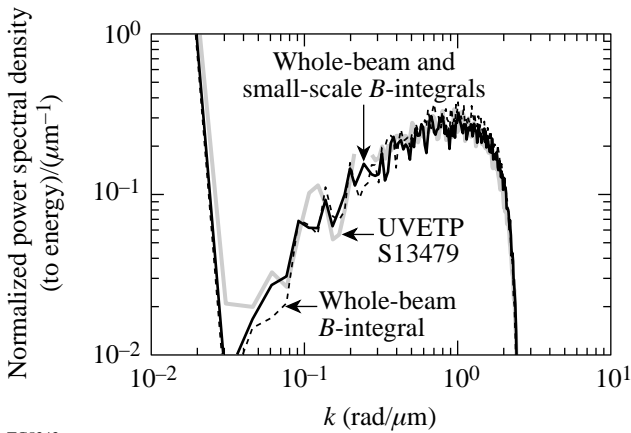
statistics of the DPP. If the state of  $\phi(x,y,t)$  changes in time over an interval  $\tau \equiv t_2 - t_1$  (where  $\tau$  is of the order of the coherence time for the pulse) such that a change in state  $\Delta\phi(x,y,\tau) \equiv \phi(x,y,t_2) - \phi(x,y,t_1)$  is nonconstant over the near field, the instantaneous far-field speckle pattern will change, resulting in time-integrated smoothing. Alternately, if the quantity  $\Delta\phi(x,y,\tau)$  is constant over the near field, during the time interval  $\tau$ , then no change in the far-field speckle pattern occurs regardless of how rapidly the state  $\phi(x,y,t)$  varies in space or time. For example, a nondispersed phase-modulated pulse can be represented by  $\phi(x,y,t) = \phi_1(x,y) + \phi_2(t)$ .

Time-integrated smoothing in the far field can be understood as a movement of the speckle structure or as a distinct change of the speckle structure as a function of time. If the change in state  $\Delta\phi(x,y,\tau)$  has a linear form, i.e.,

$$\Delta\phi(x,y,\tau) \equiv x(\partial\phi/\partial x) + y(\partial\phi/\partial y),$$

then the speckle pattern will appear to laterally shift in the far field by the amounts given by  $\Delta x_{\text{ff}} = f_{\Omega}(\partial\phi/\partial x)$  and  $\Delta y_{\text{ff}} = f_{\Omega}(\partial\phi/\partial y)$ . In the more general case, the phase-state  $\phi(x,y,t)$  can be Fourier decomposed into a set of modes as

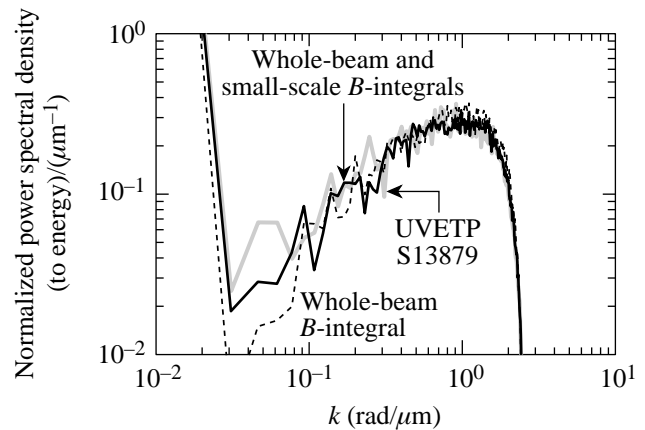
$$\phi(x,y,t) \equiv \frac{1}{4\pi^2} \iint_{\forall \text{spatial frequencies}} \tilde{\phi}(k_x, k_y, t) e^{+i(k_x x + k_y y)} dk_x dk_y, \quad (10)$$



TC5343

Figure 82.39

The 1-D power spectrum of a UVETP image of a 2-ns square pulse (shot 13479; solid gray line) and the corresponding *Waasikwa*' simulation including only whole-beam *B*-integral effects (dashed line) and both small-spatial-scale and whole-beam *B*-integral effects (solid black line).



TC5344

Figure 82.40

The 1-D power spectrum of a UVETP image of a 3-ns square pulse (shot 13879; solid gray line) and the corresponding *Waasikwa*' simulation including only whole-beam *B*-integral effects (dashed line) and both small-spatial-scale and whole-beam *B*-integral effects (solid black line).

where  $\tilde{\phi}(k_x, k_y, t)$  represents the complex spectral amplitudes of the Fourier kernel  $e^{+i(k_x x + k_y y)}$ . At each instant in time  $\phi(x, y, t) \in \mathbb{R}$ , which implies that the integral in Eq. (10) may be reduced to two times the real part of the integral over the upper half-plane that excludes the negative axis owing to the symmetry properties of the Fourier transform of real functions [i.e., the transform is Hermitian  $\tilde{\phi}(k_x, k_y, t) = \phi^*(-k_x, -k_y, t)$  (Ref. 18, p. 14)].

The smoothing effectiveness of an evolving phase state  $\phi(x, y, t)$  can be understood by examining the contribution of the term  $e^{i\phi(x, y, t)}$  to the far-field distribution. The instantaneous far-field speckle pattern is calculated by Eq. (2). The convolution theorem dictates that the result can be written as

$$I_{\text{ff}}(x_{\text{ff}}, y_{\text{ff}}, t) = \left| E_{\text{DPP}}(x_{\text{ff}}, y_{\text{ff}}, t) * E_{\phi}(x_{\text{ff}}, y_{\text{ff}}, t) \right|^2, \quad (11)$$

where the quantity  $E_{\text{DPP}}(x_{\text{ff}}, y_{\text{ff}}, t)$  represents the complex field of the speckle pattern caused by the combined effect of the current beam cross section and the DPP; the quantity  $E_{\phi}(x_{\text{ff}}, y_{\text{ff}}, t)$  represents the instantaneous complex far-field pattern caused by the phase state  $\phi(x, y, t)$ ; and the symbol  $*$  denotes the convolution operation. The extent of the far-field pattern  $E_{\phi}(x_{\text{ff}}, y_{\text{ff}}, t)$  determines the wavelengths that can be smoothed: the greater the area covered, the longer the wavelengths that the phase state  $\phi(x, y, t)$  can smooth. The far-field pattern  $E_{\phi}(x_{\text{ff}}, y_{\text{ff}}, t)$  must change over time to affect smoothing. Further, the pulse must be long enough to cover many coherence times: the longer the wavelength, the more smoothing time required.

$$\begin{aligned} \phi(x, y, t) \\ = 2 \left| \tilde{\phi}(k_x, k_y, t) \right| \sin \left( \angle \left\{ \tilde{\phi}(k_x, k_y, t) \right\} + k_x x + k_y y \right), \end{aligned} \quad (12)$$

where the term  $\left| \tilde{\phi}(k_x, k_y, t) \right|$  represents the magnitude of the Fourier component and the term  $\angle \left\{ \tilde{\phi}(k_x, k_y, t) \right\}$  represents the phase [where the operator  $\angle \left\{ e^{i\theta} \right\} = \theta$ ]. The term  $\left| \tilde{\phi}(k_x, k_y, t) \right|$  determines the amount of laser divergence, given approximately by

$$\Delta\theta \cong 2 \left[ \left| \tilde{\phi}(k_x, k_y, t) \right| + 1 \right] \sqrt{k_x^2 + k_y^2}.$$

If the quantity  $\left| \tilde{\phi}(k_x, k_y, t) \right| = \delta_m$ , where  $\delta_m$  is constant and  $\angle \left\{ \tilde{\phi}(k_x, k_y, t) \right\} = \omega_m t$ , then Eq. (12) is functionally identical to 1-D SSD.<sup>20</sup> In this scenario, the spectral components of  $E_{\phi}(x_{\text{ff}}, y_{\text{ff}}, t)$  in the far field have fixed amplitudes and a fixed

spacing (given by the well-known Bessel function expansion; see Ref. 20) but a varying relative phase. If the magnitude of the phase varies in time as  $\left| \tilde{\phi}(k_x, k_y, t) \right| = \delta_m(t)$  and if the phase term  $\angle \left\{ \tilde{\phi}(k_x, k_y, t) \right\}$  is constant, the spectral components of  $E_{\phi}(x_{\text{ff}}, y_{\text{ff}}, t)$  in the far field have a fixed spacing analogous to the SSD-like case but with a varying amplitude and a fixed relative phase. As the magnitude  $\delta_m(t)$  increases, the number of the spectral components increases and spreads out into the far field (this situation is directly analogous to what happens when the whole-beam  $B$ -integral modifies the phase magnitude where the Fourier component's wavelength is twice the beam diameter). A general case is constructed when both the magnitude and phase terms in Eq. (12) are allowed to vary with time. A stochastic model may also be employed where the magnitude and relative phase terms change in time of the order of the coherence time and obey a probability density function.

If more than one spectral mode is considered, a variety of complex smoothing mechanisms can be constructed. However, an arbitrary phase state that alters the spatial coherence over time and, in addition, is consistent with the observations cannot be selected. When considering a small number of Fourier components, the member with the greatest laser divergence can be assumed to dominate the remaining members since its laser divergence will be the strongest (see Ref. 21, p. 241 regarding transmission bandwidth). Otherwise, the total divergence of each member must be considered in terms of their combined effect as they convolve together in the far field and produce a greater spread and smooth longer wavelengths. To this end, the dominant mode will contribute a full-angle divergence of  $\Delta\theta \cong 2 \left[ \delta_m(t) + 1 \right] \sqrt{k_x^2 + k_y^2}$  and a temporal bandwidth  $\Delta\omega \cong \left[ \delta_m(t) + 1 \right] \omega_m$ , and the other modes will contribute significantly only if their respective spatial or temporal bandwidths are comparable to the dominant mode. The maximum far-field wavelength that can be smoothed is given by  $S_{\text{max}} = f_{\Omega} \Delta\theta$ . The situation is analogous to the small-spatial-scale  $B$ -integral when the Fourier components have a fixed phase relationship (i.e., they do not move across the near field) and the modulation depth (of each spectral component) changes as the pulse evolves.

### 1. Whole-Beam $B$ -Integral Modeling

The electric field and phase calculated by *RAINBOW* for a pulsed beam are in cylindrical coordinates, viz.  $(r, t)$ . Conversely, *Waasikwa*' models both transverse dimensions and time in rectangular cartesian coordinates, viz.  $(x, y, t)$ . Accordingly, a two-dimensional spline fit is performed at each time step to resample *RAINBOW* data into cartesian coordinates. The complex-valued electric field with no applied FM or DPP

that describes the UV near field is expressed in terms of the converted *RAINBOW* data as

$$E(x, y, t) \equiv E_{0_{rb}}(x, y, t) e^{i\phi_{B_{rb}}(x, y, t)}. \quad (13)$$

The phase term  $\phi_{B_{rb}}(x, y, t)$  calculated by *RAINBOW* represents the whole-beam *B*-integral that is an intensity-dependent phase accumulated during propagation within a nonlinear medium.

The phase state calculated by *RAINBOW* is roughly separable, i.e.,  $\phi_{B_{rb}}(x, y, t) \cong \delta_{B_{rb}}(t)\phi_{B_{rb}}(x, y)$ . The quantity  $\phi_{B_{rb}}(x, y)$  represents the initial beam shape that is injected into the laser chain, and the term  $\delta_{B_{rb}}(t)$  represents the initial pulse shape. This occurs because of self-phase modulation in the laser chain that is more severe in the first amplifiers where the local intensity is higher and prior to significant gain saturation that causes the intensity beam profile to change over time. In other words, even though the intensity envelope is altered after the whole laser chain, the phase modulation retains a shape very similar to that of the injected beam. (The form of the phase state is analogous to that discussed in the previous section, where the spatial portion of a mode is fixed and the modulation depth changes over time.) Therefore, the laser divergence causes the far field to expand as a function of time. This effect for a 100-ps Gaussian pulse is illustrated in

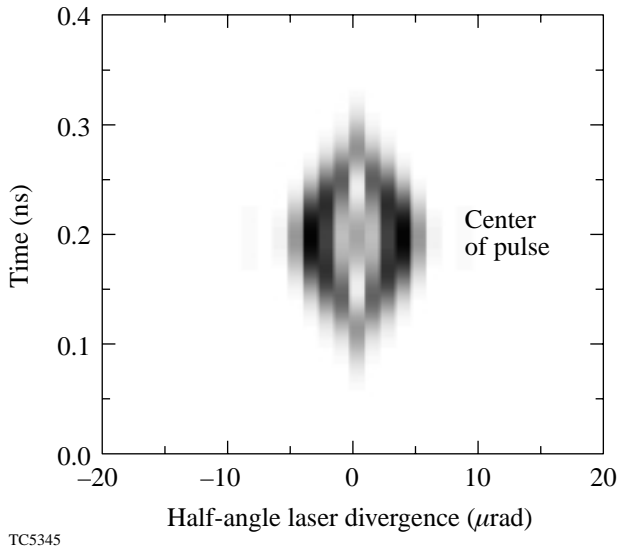


Figure 82.41  
The calculated laser divergence due to the whole-beam *B*-integral as a function of time for a 40-J, 100-ps Gaussian pulse.

Fig. 82.41, where the laser divergence is plotted against time. Based on the calculated laser divergence one would expect that the whole-beam *B*-integral would smooth down to the far-field spatial frequency,

$$k_{ff} = \frac{2\pi}{f_{\Omega}\Delta\theta} \approx 0.35 \frac{\text{rad}}{\mu\text{m}},$$

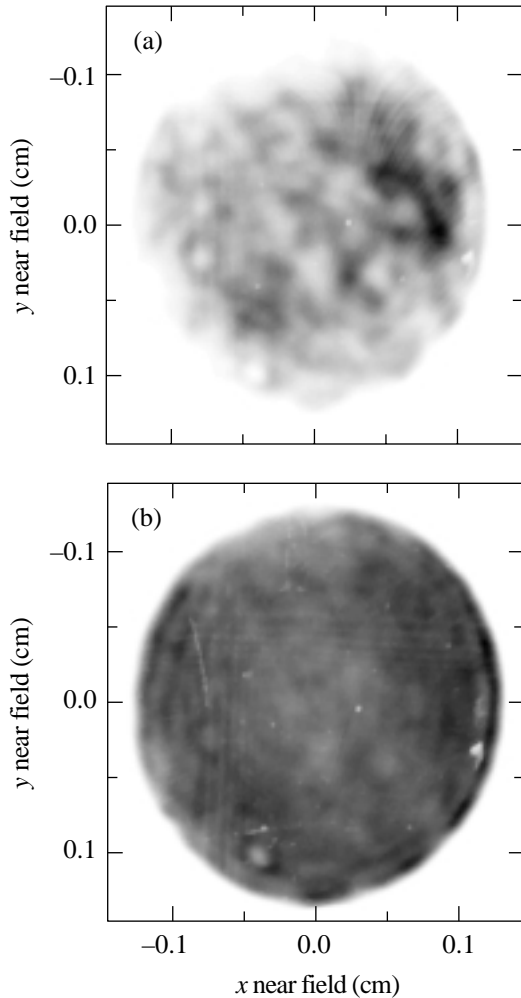
from the calculated full-angle divergence of  $\Delta\theta \approx 10 \mu\text{rad}$  (see Fig. 82.41). As shown in the **Experimental Results** section the nonuniformity calculated with this model, however, falls short of the measured smoothing. Additionally, the power spectrum (dashed line in Fig. 82.37) is almost identical to the low-energy pulse (dashed line in Fig. 82.36). The primary reason is that although there is sufficient laser divergence, the temporal bandwidth for this method is insufficient to produce a short coherence time because the peak *B*-integral is limited. This model also fails to predict the measured nonuniformity and power spectra for the square pulses for the same reasons.

## 2. Modeling of Small-Spatial-Scale and Whole-Beam *B*-Integrals

Near-field images of high-energy shots were obtained in the UV section of the OMEGA system (measured after the final amplifiers and after the FCC's). Two pulse lengths—a 100-ps Gaussian [Fig. 82.42(a)] and a 1-ns square [Fig. 82.42(b)]—were captured to compare the fluence of the early times to that at later times. The 100-ps Gaussian near field was representative of a center-peaked beam; the 1-ns square pulse was representative of an edge-peaked beam. These images revealed evidence of small-spatial-scale intensity ripple across the beam, which was more severe for the shorter pulse than the longer pulse because of gain-saturation effects. This evidence has led to speculation that the small-spatial-scale *B*-integral caused the observed smoothing; the depth of the fluence ripple corresponds to the laser divergence required to affect the smoothing in the range  $k_{ff} > 0.1 \text{ (rad}/\mu\text{m})$ , and the growth of the ripple provides the required temporal bandwidth.

The small-spatial-scale and whole-beam *B*-integral phases both result from self-phase modulation, which is proportional to the local accumulated intensity of the beam as it propagates through a nonlinear medium. The combined phase effects of the small-spatial-scale and whole-beam *B*-integrals can be inferred from the fluence measured by the near-field images. The time evolution of the small-spatial-scale *B*-integral can be approximated to follow the spatiotemporal evolution of the whole-beam *B*-integral that is calculated by *RAINBOW*. This is

only valid, however, over a small energy range neighboring the measured near field because the ripple across the beam becomes less pronounced as saturation becomes important. For long, high-energy (fluence) pulses, the beam experiences significant gain saturation in the system amplifiers. The beam profile is smoothed at later times in the pulse because the amount of gain saturation at any spatial location in the beam is proportional to the beam's fluence at that location; initially "hotter" regions of the beam experience reduced gain. This effect is modeled by temporally blending different measured near fields.



TC5346

Figure 82.42

Two near-field fluence measurements, taken after the FCC's, represent the early- and late-time evolution of a long pulse. (a) The first image (shot 14233) is a 100-ps Gaussian pulse representative of the early-time evolution. (b) The second image (shot 14234) is a 1-n s square pulse representative of the late-time evolution.

A model of combined  $B$ -integral effects is constructed by perturbing both the intensity and phase calculated by *RAINBOW* simulations. The electric field of the near field is expressed as [compare Eq. (3)]

$$E_{\text{sim}}(x, y, t) \equiv E_{0_{\text{sim}}}(x, y, t)e^{i\phi_{B_{\text{sim}}}(x, y, t)}, \quad (14)$$

where the perturbed magnitude of the electric field is defined by

$$E_{0_{\text{sim}}}(x, y, t) \equiv E_{0_{\text{rb}}}(x, y, t)\sqrt{\Gamma(x, y)}, \quad (15)$$

and the perturbed phase contribution due to both small-spatial-scale and whole-beam  $B$ -integral effects is given by

$$\phi_{B_{\text{sim}}}(x, y, t) \equiv \phi_{B_{\text{rb}}}(x, y, t)\Gamma(x, y). \quad (16)$$

The unperturbed magnitude and phase of the electric field calculated by *RAINBOW* simulations are given in Eqs. (15) and (16) by  $E_{0_{\text{rb}}}(x, y, t)$  and  $\phi_{B_{\text{rb}}}(x, y, t)$ , respectively. The perturbation function  $\Gamma(x, y)$  represents the scaled ratio of a UV near-field fluence measurement to the fluence calculated from a *RAINBOW* simulation, namely

$$\Gamma(x, y) \equiv \alpha \frac{F_{\text{UVnf}}(x, y)}{F_{\text{rb}}(x, y)}, \quad (17)$$

where the subscript UVnf indicates the UV near-field measurement, the subscript rb indicates the *RAINBOW* simulation, and  $\alpha$  is the proportionality constant and is defined by

$$\alpha \equiv \frac{W_{\text{rb}}}{W_{\text{UVnf}}}, \quad (18)$$

where  $W_{\text{rb}}$  is the *RAINBOW* simulation energy and  $W_{\text{UVnf}}$  is the UV near-field energy.

The two UV near-field measurements are blended temporally to construct a model for longer, higher-energy pulses. The UV near-field measurements are used to divide the longer pulse into segments based on the energy within each measured UV near field. The techniques described previously are employed to evaluate the perturbation function within each temporal segment. The blending function is defined as a dimensionless and smooth step function:

$$b(\tau_{\text{on}}, \tau_{\text{off}}, r, t) \equiv \frac{1}{2} \left\{ \tanh[r(t - \tau_{\text{on}})] - \tanh[r(t - \tau_{\text{off}})] \right\}, \quad (19)$$

where  $\tau_{\text{on}}$  and  $\tau_{\text{off}}$  are the turn-on and turn-off times and  $r$  is the rate at which the blending function mixes the UV near fields. The dividing time of the segments is defined when the *RAINBOW* simulation has equivalent energy to a UV near-field measurement:

$$W_{\text{UVnf}_n} \equiv \int_0^{\tau_n} \iint_{\text{near field}} I_{\text{rb}}(x, y, t) dx dy dt, \quad (20)$$

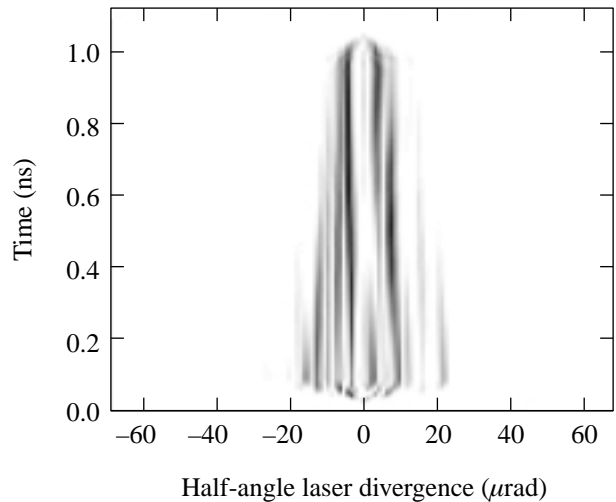
where the subscript  $n$  refers to a particular near field, e.g.,  $n = 1$  for the first UV near field. The times  $\tau_n$  define the turn-on and turn-off times for the blending function; one blending function turns off as the next one turns on, e.g., the first blending function is  $b(-\infty, \tau_1, r, t)$  and the second is  $b(\tau_1, \tau_2, r, t)$ . The final blending function mixes into unperturbed *RAINBOW* data with  $b(\tau_2, \infty, r, t)$ . Energy conservation requires that

$$\sum_{n=1}^3 b(\tau_{\text{on}_n}, \tau_{\text{off}_n}, r, t) = 1; \forall t. \quad (21)$$

The time difference between  $\tau_1$  and  $\tau_2$  will change according to the modeled pulse. As the differential  $\Delta\tau = \tau_2 - \tau_1$  decreases, the mixing rate  $r$  increases, which effectively describes how the small-spatial-scale perturbations change more rapidly. The decreased  $\Delta\tau$  occurs physically because the saturation fluence is reached earlier for the higher-intensity pulses. The mixing

rate is adjusted to eliminate any step that may be introduced in the nonuniformity as a function of time. The switching times and mixing rates for the different modeled pulses are given in Table 82.V.

The calculated laser divergence for this model as a function of time is illustrated in Fig. 82.43 for a 1-ns square pulse at full-system energy. This modeling scheme works well for the longer square pulses but does not adequately describe the smoothing observed for the shorter, 100-ps pulses. This is attributed to the fact that the early time evolution of the small-scale *B*-integral is not captured on either measured near field, and consequently, only a single UV near field is used.



TC5347

Figure 82.43 The calculated laser divergence due to the whole-beam and small-spatial-scale *B*-integrals as a function of time for a 1-ns square pulse at full system energy.

Table 82.V: Summary of the model parameters for 1-ns, 2-ns, and 3-ns square pulses. The parameters  $\tau_1$  and  $\tau_2$  define when the *RAINBOW* simulation has energy equivalent to the first and second UV near field, respectively. The energy of the first UV near field is 100 J; the energy of the second UV near field is 290 J.

Shot Number	Nominal Pulse Width (ns)	Measured Energy (J)	$\tau_1$ for 100 J (ns)	$\tau_2$ for 290 J (ns)	$r$ (1/ns)
S15723	1	508	0.225	0.555	1.92
S13479	2	370	0.645	1.57	1.12
S13879	3	331	1.18	2.99	0.775

## Conclusion

The observed smoothing on high-energy OMEGA shots without applied FM has been successfully modeled using a combination of small-spatial-scale and whole-beam  $B$ -integral effects. The smoothing affects mainly the spatial wave numbers  $k_{\text{eff}} > 0.1(\text{rad}/\mu\text{m})$  and can reduce the nonuniformity to levels of 62%. The nonuniformity decreases approximately linearly with increasing average intensity of the pulsed beam. The amount of smoothing due to small-spatial-scale  $B$ -integral effects is insufficient for direct-drive ICF. Reference 13 shows that smoothing by spectral dispersion overwhelms this effect in the mid-range spatial frequencies where these modes are considered the most dangerous spatial frequencies for ICF implosions.<sup>7</sup> Hence, it is not expected that the  $B$ -integral effects mitigate hydrodynamic instabilities due to their minor influence.

## ACKNOWLEDGMENT

This work was partially supported by the U.S. Department of Energy Office of Inertial Confinement Fusion under Cooperative Agreement No. DE-FC03-92SF19460, the University of Rochester, and the New York State Energy Research and Development Authority. The support of DOE does not constitute an endorsement by DOE of the views expressed in this article.

## REFERENCES

1. C. P. Verdon, *Bull. Am. Phys. Soc.* **38**, 2010 (1993).
2. S. E. Bodner, D. G. Colombant, J. H. Gardner, R. H. Lehmborg, S. P. Obenschain, L. Phillips, A. J. Schmitt, J. D. Sethian, R. L. McCrory, W. Seka, C. P. Verdon, J. P. Knauer, B. B. Afeyan, and H. T. Powell, *Phys. Plasmas* **5**, 1901 (1998).
3. D. K. Bradley, J. A. Delettrez, and C. P. Verdon, *Phys. Rev. Lett.* **68**, 2774 (1992); J. Delettrez, D. K. Bradley, and C. P. Verdon, *Phys. Plasmas* **1**, 2342 (1994); J. D.ilkenny, S. G. Glendinning, S. W. Haan, B. A. Hammel, J. D. Lindl, D. Munro, B. A. Remington, S. V. Weber, J. P. Knauer, and C. P. Verdon, *Phys. Plasmas* **1**, 1379 (1994); R. Epstein, *J. Appl. Phys.* **82**, 2123 (1997); V. A. Smalyuk, T. R. Boehly, D. K. Bradley, V. N. Goncharov, J. A. Delettrez, J. P. Knauer, D. D. Meyerhofer, D. Oron, and D. Shvarts, *Phys. Rev. Lett.* **81**, 5342 (1998).
4. F. J. Marshall and G. R. Bennett, *Rev. Sci. Instrum.* **70**, 617 (1999); F. J. Marshall, J. A. Delettrez, V. Yu. Glebov, R. P. J. Town, B. Yaakobi, R. L. Kremens, and M. Cable, *Phys. Plasmas* **7**, 1006 (2000).
5. T. R. Boehly, D. L. Brown, R. S. Craxton, R. L. Keck, J. P. Knauer, J. H. Kelly, T. J. Kessler, S. A. Kumpan, S. J. Loucks, S. A. Letzring, F. J. Marshall, R. L. McCrory, S. F. B. Morse, W. Seka, J. M. Soures, and C. P. Verdon, *Opt. Commun.* **133**, 495 (1997).
6. S. Skupsky, R. W. Short, T. Kessler, R. S. Craxton, S. Letzring, and J. M. Soures, *J. Appl. Phys.* **66**, 3456 (1989).
7. Laboratory for Laser Energetics LLE Review **69**, 1, NTIS document No. DOE/SF/19460-152 (1996) (Copies may be obtained from the National Technical Information Service, Springfield, VA 22161); S. Skupsky and R. S. Craxton, *Phys. Plasmas* **6**, 2157 (1999).
8. J. E. Rothenberg, *J. Opt. Soc. Am. B* **14**, 1664 (1997).
9. T. J. Kessler, Y. Lin, J. J. Armstrong, and B. Velazquez, in *Laser Coherence Control: Technology and Applications*, edited by H. T. Powell and T. J. Kessler (SPIE, Bellingham, WA, 1993), Vol. 1870, pp. 95–104.
10. Y. Lin, T. J. Kessler, and G. N. Lawrence, *Opt. Lett.* **21**, 1703 (1996).
11. Y. Kato, unpublished notes (1984); K. Tsubakimoto *et al.*, *Opt. Commun.* **91**, 9 (1992); K. Tsubakimoto *et al.*, *Opt. Commun.* **103**, 185 (1993).
12. Laboratory for Laser Energetics LLE Review **45**, 1, NTIS document No. DOE/DP40200-149 (1990) (Copies may be obtained from the National Technical Information Service, Springfield, VA 22161); T. E. Gunderman, J.-C. Lee, T. J. Kessler, S. D. Jacobs, D. J. Smith, and S. Skupsky, in *Conference on Lasers and Electro-Optics*, Vol. 7, 1990 OSA Technical Digest Series (Optical Society of America, Washington, DC, 1990), p. 354.
13. S. P. Regan, J. A. Marozas, J. H. Kelly, T. R. Boehly, W. R. Donaldson, P. A. Jaanimagi, R. L. Keck, T. J. Kessler, D. D. Meyerhofer, W. Seka, S. Skupsky, and V. A. Smalyuk, "Experimental Investigation of Smoothing by Spectral Dispersion," to be published in the *Journal of the Optical Society of America B*.
14. A. E. Siegman, *Lasers* (University Science Books, Mill Valley, CA, 1986).
15. D. C. Brown, in *High-Peak-Power Nd:Glass Laser Systems*, edited by D. L. MacAdam, Springer Series in Optical Sciences (Springer-Verlag, Berlin, 1981), Vol. 25.
16. D. Cortesi, *Topics in IRIX® Programming*, Document Number 007-2478-007, Silicon Graphics, Inc., Mountain View, CA, 1999.
17. J. W. Goodman, *Introduction to Fourier Optics* (McGraw-Hill, New York, 1968).
18. R. N. Bracewell, *The Fourier Transform and Its Applications*, 2nd ed., rev., McGraw-Hill Series in Electrical Engineering. Circuits and Systems (McGraw-Hill, New York, 1986).
19. J. G. Proakis and D. G. Manolakis, *Introduction to Digital Signal Processing* (Macmillan, New York, 1988).
20. Laboratory for Laser Energetics LLE Review **78**, 62, NTIS document No. DOE/SF/19460-295 (1999). Copies may be obtained from the National Technical Information Service, Springfield, VA 22161.
21. A. B. Carlson, *Communication Systems: An Introduction to Signals and Noise in Electrical Communication*, McGraw-Hill Electrical and Electronic Engineering Series (McGraw-Hill, New York, 1968), p. 154.

# Three-Dimensional Modeling of Capsule Implosions in OMEGA Tetrahedral Hohltraums

## Introduction

To achieve ignition and gain in inertial confinement fusion (ICF), a spherical target must be compressed with a highly uniform drive mechanism.<sup>1-3</sup> Perturbations in the drive can lead to a distorted fuel core as well as hydrodynamic instabilities, which cause the colder ablator material to mix with the fuel in the central hot spot, effectively quenching the nuclear burn.<sup>4-6</sup> The direct-drive approach to achieving this uniform implosion uses an intense laser pulse to ablate a glass or plastic shell and compress the fuel inside like a spherical rocket.<sup>7</sup> The nonuniformities inherent in the laser beam tend to imprint the target with a “seed” that can cause debilitating hydrodynamic instabilities. To avoid these high-spatial-frequency perturbations, the lasers can alternatively be pointed at the inside of a high-Z cavity called a *hohlraum*, which converts the laser energy into a smooth x-ray radiation field that then compresses a similar capsule, again through a rocket-type ablation.<sup>2</sup>

Traditionally, hohlraums have utilized a cylindrical geometry with two laser entrance holes (LEH's) and azimuthal symmetry. Recently, an alternative hohlraum geometry with four LEH's in a spherical case has been proposed as a means for producing an extremely uniform radiation drive.<sup>8,9</sup> These “tetrahedral hohlraums” are particularly well suited for experiments on the University of Rochester's OMEGA laser facility<sup>10</sup> since the soccer-ball geometry of the target chamber possesses multiple beam configurations with perfect tetrahedral symmetry. Accordingly, an extensive series of tetrahedral hohlraum experiments have been carried out on OMEGA under the leadership of the Los Alamos National Laboratory,<sup>11</sup> in a multilaboratory collaboration.

This article reports on the three-dimensional (3-D) view-factor code *BUTTERCUP*, which has been used to model these experiments. Since the code was first reported in Ref. 9, it has been expanded to model the time-dependent radiation transport in the hohlraum and the hydrodynamic implosion of the capsule. Additionally, a 3-D postprocessor has been written to simulate x-ray images of the imploded core. Despite *BUTTERCUP*'s relative simplicity, its predictions for radia-

tion drive temperatures, fusion yields, and core deformation show close agreement with experiment.

The tetrahedral hohlraum experiments on OMEGA<sup>11</sup> have investigated the basic symmetry properties and uniformity of capsule implosions, the radiation drive temperatures, and the effect of high convergence on neutron-yield degradation. Most of these experiments have used thin-walled gold hohlraums with standard Nova implosion capsules filled with DD gas. The best results have been obtained from hohlraums with an inner diameter of 2800  $\mu\text{m}$ , LEH diameter of 700  $\mu\text{m}$ , and typical capsule outer diameter of 550  $\mu\text{m}$  (see Fig. 82.44). The 60 OMEGA beams enter the hohlraum in four groups with 15 beams through each LEH. These 15 beams form three rings with various angles of incidence, namely 23.2° (6 beams), 47.8° (6 beams), and 58.8° (3 beams). As with cylindrical hohlraums, the beam pointing is constrained by minimum clearance requirements to avoid absorption and/or refraction through the plasma ablating off the capsule or the hohlraum

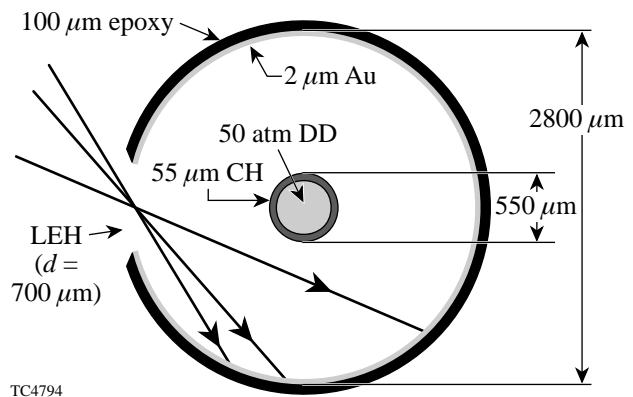


Figure 82.44

Schematic of a thin-walled tetrahedral hohlraum used for OMEGA implosion experiments. One of four laser entrance holes (LEH's) is shown with beams entering at three different angles (23.2°, 47.8°, and 58.8°). The standard Nova capsule has a 550- $\mu\text{m}$  outer diameter and a 55- $\mu\text{m}$ -thick CH shell and is filled with 50 atm of DD gas.

wall. Tetrahedral hohlraums have an additional pointing constraint, that of clearing an opposing LEH to avoid forming plasma blowoff that would interfere with incoming beams. Unlike cylindrical hohlraums, however, the spherical geometry of the tetrahedral design eliminates the possibility of “glint” (irradiation of the capsule by laser light specularly reflected off the hohlraum wall at early times).<sup>12</sup>

The OMEGA soccer-ball geometry has numerous group rotational symmetries, including that of each Platonic solid. The tetrahedral symmetry group is itself embedded in a larger, dodecahedral group where the 60 beams can be divided into 12 sets of 5 independent beams; therefore, pointing coordinates must be calculated for only 5 different beams, and the rest are determined by rotations in the dodecahedral symmetry group. This property provides some inherent symmetry advantages for the tetrahedral hohlraum, causing all  $l = 1, 2,$  and  $5$  spherical-harmonic components of the radiation drive to be identically zero.<sup>8</sup> For the specific hohlraum designs used in this article, the x-ray drive nonuniformity on the capsule ( $\sigma_{\text{rms}}$ ) is almost entirely dominated by the  $Y_{32}$  spherical-harmonic mode<sup>9,13</sup> and, in the optimal designs, is less than 1% during most of the laser pulse. This highly uniform drive has been confirmed by x-ray images of imploded cores that are essentially round to within the resolution of the instrument.<sup>11</sup>

Despite the remarkable symmetry properties of tetrahedral hohlraums, the cylindrical design has been traditionally dominant in the ICF field, largely because of its azimuthal symmetry. Thus, cylindrical hohlraums can be modeled accurately in a two-dimensional (2-D) geometry, while the tetrahedral hohlraum is inherently a three-dimensional (3-D) problem. Considering the complexity of even a 2-D radiation hydrodynamics code,<sup>14</sup> it is understandable that there has not been significant interest in the 3-D tetrahedral hohlraums until only recently. With the recent progress in developing detailed 3-D codes,<sup>5</sup> however, tetrahedral hohlraums offer an ideal test-bed for theoretical and experimental comparisons. As part of this effort, we have written a 3-D view-factor code called *BUTTERCUP*, which includes radiation transport in the hohlraum and a hydrodynamic treatment of the capsule implosion. Because of the highly uniform nature of these implosions, basic 3-D effects can be accurately modeled as perturbations on a one-dimensional (1-D) model. We will explain this pseudo-3D modeling technique in greater detail below.

Although *BUTTERCUP* does not model laser–plasma interactions in the hohlraum or the motion of the gold wall, its simplicity is perhaps its most powerful trait, allowing for

repeated calculations over a wide range of input parameters and thus making it ideal for target design. For example, the dimensions and pointing parameters for the hohlraums described in Ref. 11 were largely based on results of *BUTTERCUP* calculations. Further, by using a simple energy diffusion model, *BUTTERCUP* can predict the time-varying radiation drive temperature  $T_r(t)$  in the hohlraum. This agrees closely with experimental measurements as well as with more sophisticated hydrodynamic code calculations. Neutron yields have also been calculated by 1-D and pseudo-3D models and agree well with initial experimental results. Additionally, a post-processor has been written to simulate x-ray images of the imploded capsule’s self-emission. Comparisons with the theoretical core shapes and experimental images provide valuable new insight into the relationship between a 3-D fuel core and its 2-D image and show in particular how a 3-D distortion may be emphasized or smoothed out.

Ultimately, the success of tetrahedral hohlraum experiments on OMEGA will help to determine the feasibility of a tetrahedral ignition design for the National Ignition Facility (NIF). While the NIF laser’s port geometry lacks true tetrahedral symmetry, the addition of equatorial direct-drive ports allows for a possible design that can focus 44 of the 48 quads (four beams) into a tetrahedral hohlraum and still provide excellent drive uniformity.<sup>9</sup>

In describing *BUTTERCUP* and its results, we will follow a course of increasing complexity, starting in the next section with an explanation of a static view-factor model that assumes a single albedo over the hohlraum wall. This includes a zero-dimensional implosion model, enabling the time-dependent uniformity on the capsule to be predicted for different tetrahedral hohlraum designs on OMEGA, given the albedo as a function of time. In a subsequent section we introduce a time-dependent model for the laser deposition and radiation transport into the wall of the hohlraum, which allows the time-dependent uniformity and radiation temperature  $T_r(t)$  to be calculated directly without reference to the albedo. We then discuss in detail a pseudo-3D radiation-hydrodynamic model for the capsule implosion that predicts convergence ratios, low-order core distortions, and fusion yields. We also describe a 3-D radiation postprocessor that allows direct comparison between theoretical and experimental results.

This work shows that a relatively simple code can make reasonably accurate predictions of hohlraum temperatures, radiation drive uniformity, and the effects of core distortion and high convergence ratio on neutron yield degradation.

*BUTTERCUP* proves to be immediately useful not only in experimental planning and interpretation, but also as an important tool for aiding in the development of more-sophisticated 3-D ICF codes.

### Fundamental Features of the Code *BUTTERCUP*

The most basic features of *BUTTERCUP* include the ability to trace rays from multiple laser beams in a three-dimensional hohlraum and a view-factor algorithm to calculate the resulting radiation uniformity on the surface of the fuel capsule.<sup>9</sup> Both cylindrical and tetrahedral hohlraums can be modeled in a fully 3-D geometry. In the tetrahedral geometry, the four LEH's are located at the angular coordinates  $(\theta, \phi) = [(54.7^\circ, 0^\circ), (54.7^\circ, 180^\circ), (125.3^\circ, 90^\circ), \text{ and } (125.3^\circ, 270^\circ)]$ , while in the cylindrical geometry, the axis of the hohlraum is taken to be along  $\theta = 0^\circ$ . The methods described below apply equally well for either geometry, but we will be concerned primarily with the tetrahedral orientation.

First, each laser beam is divided into a large number of individual rays, each with an equal fraction of the total drive power. The OMEGA beams are treated as circular cones with an  $f/6$  focus. For hohlraum experiments on OMEGA, the direct-drive phase plates are removed, giving a laser spot size of about 50- $\mu\text{m}$  diameter at best focus. Once the beam is divided, each individual ray is traced from an initial position and direction through the hohlraum, allowing multiple geometric reflections with a small amount of random scattering until all the energy in the ray has been absorbed (usually no more than two bounces). When the ray hits the hohlraum wall, it deposits a fraction  $A(\theta_i)$  of its total energy, given by

$$A(\theta_i) = 1 - \exp(-b \cos^r \theta_i), \quad (1)$$

where the parameter  $b$  determines the absorption at normal incidence and the parameter  $r$  gives the angular dependence. In the absence of an accurate experimental determination of  $A(\theta_i)$  in a hohlraum, we take  $r = 1$  and  $b = 3$ . These parameters give an absorption of 90% for  $\theta_i = 40^\circ$  (thus 99% after two bounces), consistent with Nova data.<sup>15</sup> Of the laser energy absorbed by the wall, typically 60% to 70% is re-emitted as x-ray radiation; the rest is lost to hydrodynamic motion and heating of the hohlraum wall. In this static model, no laser energy is deposited along the beam path and the time evolution of the gold plasma is not simulated. The effect of wall motion on the irradiation uniformity can be modeled by repeating the ray-trace calculation with the same laser pointing but using different hohlraum dimensions, such as might be obtained from 1-D hydrody-

namical calculations of a tetrahedral hohlraum or 2-D calculations of a cylindrical hohlraum. For the results reported in this article, however, wall motion was not taken into account.

Despite these simplifications, we can still estimate a single background radiation temperature  $T_r$  by assuming an equilibrium Planckian radiation field in the hohlraum cavity. Following Ref. 9, the temperature  $T_r$  is calculated with a basic energy equation<sup>16–18</sup> that balances the power entering the radiation field from the laser source and the power lost from the radiation field through the LEH's and absorption by the walls and capsule:

$$P_{\text{las}} \eta_l = \sigma T_r^4 (NA_h + \beta_w A_w + \beta_c A_c), \quad (2)$$

where  $P_{\text{las}}$  is the total laser power absorbed by the case,  $\eta_l$  is the conversion efficiency from the laser to x rays in the radiation field,  $\sigma$  is the Stefan–Boltzmann constant, and the term  $(NA_h + \beta_w A_w + \beta_c A_c)$  may be thought of as the effective area of the hohlraum. The quantities  $A_h$ ,  $A_w$ , and  $A_c$  are the areas of an LEH, the wall, and the capsule, respectively, in a hohlraum with  $N$  holes. The quantity  $\beta_w$  is defined as  $1 - \alpha_w$ , where  $\alpha_w$  is the wall albedo, the fraction of the x-ray energy incident on the hohlraum wall that is reradiated into the hohlraum cavity;  $\beta_c (= 1 - \alpha_c)$ , where  $\alpha_c$  is the capsule albedo) is similarly defined. The wall albedo  $\alpha_w$  increases with time and, at the peak of the laser pulse, is typically 0.8 for OMEGA and 0.9 for the NIF. The capsule albedo  $\alpha_c$  is taken here to be small (0.1). The x-ray conversion efficiency  $\eta_l$  generally depends on irradiation conditions and is taken to be 0.65 here. The wall albedo may be calculated as a function of time and location on the hohlraum wall (see the next section); however, it is often useful to assume a single, spatially invariant albedo that characterizes the average hohlraum conditions at a given time. We make this single-albedo assumption in this section.

For a given albedo, *BUTTERCUP* calculates the blackbody emission from each point  $\mathbf{r}$  on the hohlraum wall by combining a spatially uniform background radiation source  $\sigma T_r^4$  with the absorbed laser intensity  $I_l(\mathbf{r})$  at that point. The actual emitted flux  $I_e(\mathbf{r})$  depends on the wall albedo and the x-ray conversion efficiency:<sup>9</sup>

$$I_e(\mathbf{r}) = \alpha_w \sigma T_r^4 + \eta_l I_l(\mathbf{r}), \quad (3a)$$

where the spatial dependence of  $I_e(\mathbf{r})$  and  $I_l(\mathbf{r})$  has been explicitly retained. In this model the wall treats the x-ray and laser sources independently: i.e., a fraction  $\alpha_w$  of the radiation flux  $\sigma T_r^4$  incident upon the wall from the cavity and a fraction

$\eta_l$  of the laser flux  $I_l(\mathbf{r})$  absorbed in the wall are emitted into the cavity. The quantity  $\eta_l$  as defined here includes the combined effects of the conversion of the absorbed laser energy to x rays and reradiation from the wall.

To illustrate this, suppose that the laser were converted to x rays in the plasma with efficiency  $\eta'_l$  and the reasonable assumption were made that half were emitted outward from the wall and half were directed inward to be re-emitted with an albedo  $\alpha'_w$ . (The use of a different  $\alpha'_w$  allows for the x-ray energy fraction reradiated from the laser source to differ from that reradiated from the cavity radiation source.) Equation (3a) would then become

$$I_e(\mathbf{r}) = \alpha_w \sigma T_r^4 + \frac{1}{2}(1 + \alpha'_w) \eta'_l I_l(\mathbf{r}), \quad (3b)$$

giving

$$\eta_l = \frac{1}{2}(1 + \alpha'_w) \eta'_l. \quad (3c)$$

It is also worth noting that Eq. (3a), when integrated over the wall, provides two source terms for the radiation field in the cavity,  $\alpha_w \sigma T_r^4 A_w$  and  $\eta_l P_{\text{las}}$ , consistent with Eq. (2), confirming that the same value of  $\eta_l$  must be used in both equations.

Assuming a Lambertian source, Eq. (3a) permits a brightness (spectrally integrated power/unit area/unit solid angle)  $B_e(\mathbf{r}) = I_e(\mathbf{r})/\pi$  that is independent of direction to be defined at all points on the hohlraum wall. *BUTTERCUP* then uses a 3-D view-factor algorithm<sup>9,19–23</sup> to calculate the radiation drive uniformity on the capsule. For each point on the surface of the capsule, the total incident radiation-drive intensity  $I(\theta, \phi)$  is determined by integrating the brightness  $B_e(\mathbf{r})$  of the wall over all solid angles, as seen by the capsule, for the entire visible hemisphere. The radiation drive as a function of time can be determined by using time-varying input values for the laser pulse shape  $P_{\text{las}}(t)$  and the albedo  $\alpha_w(t)$ ; the latter can be inferred from experimental measurements, calculated directly as in the next section, or imported from a calculation by a hydrocode. For a given pulse shape, the albedo is only weakly dependent on the hohlraum irradiation geometry. Theoretical and experimental Nova results can thus be applied to OMEGA hohlraums with a fair level of accuracy.

Since the radiation uniformity on the capsule depends largely on the ratio of the hohlraum radius to the capsule radius,<sup>2,8,20</sup> the changing size of the imploding capsule must

be considered when calculating the time-dependent drive uniformity. To do this, a zero-dimensional (0-D) “rocket model” is employed, treating the capsule as a thin shell with a time-varying radius  $r_{\text{shell}}(t)$  and mass  $m(t)$ . Following Lindl,<sup>2</sup> we use scaling laws that relate the ablation pressure  $P_a$  (dyn/cm<sup>2</sup>) and the mass ablation rate  $\dot{m}$  (g/cm<sup>2</sup>/s) to powers of  $T_r(t)$  (as measured in hundreds of eV):

$$P_a(t) = 5.1 \times 10^{12} T_r^{3.5}(t),$$

$$\dot{m}(t) = 5.9 \times 10^5 T_r^3(t),$$

(4)

$$P_{\text{gas}}(t) = 7.7 \times 10^2 r_{\text{shell}}^{-5},$$

$$m(t) \ddot{r}_{\text{shell}}(t) = -4\pi r_{\text{shell}}^2 [P_a(t) - P_{\text{gas}}(t)],$$

where  $P_{\text{gas}}$  is the internal gas pressure of the capsule, assuming adiabatic heating of the fuel. The radius of the shell  $r_{\text{shell}}$  is measured in centimeters and the time  $t$  in seconds. This simple model has been found to predict remarkably accurate implosion trajectories, giving a stagnation time of 3 ns for PS22 in close agreement with experiment. Coupling the view-factor vacuum radiation transport with the time-varying capsule radius then gives a prediction for the time-dependent radiation-drive uniformity on the capsule.

Figure 82.45 shows the spatial uniformity of the x-ray drive incident on the capsule as a function of time for two different tetrahedral designs. The dashed curves are the result of the radiation source as determined from Eqs. (2) and (3) coupled to the 0-D rocket model. The time-dependent albedo used in Eqs. (2) and (3) was obtained from the wall-diffusion model described in the next section. The results of this diffusion model are shown as the solid curves. Since the nonuniformity is typically dominated (>90%) by the  $Y_{32}$  spherical-harmonic mode, we show only the contribution from  $\sigma_{32}$ , where the total  $\sigma_{\text{rms}}$  is defined as in Ref. 22:

$$\sigma_{\text{rms}}^2 \equiv \sum_{l,m} \sigma_{lm}^2. \quad (5)$$

For both designs, Fig. 82.45 shows a noticeable improvement in drive uniformity later in time, which is primarily a consequence of the converging capsule radius. Note that the simple energy-balance calculation agrees quite well with the more-detailed wall-diffusion calculation throughout most of the

laser pulse. At early times, the single-albedo assumption of the energy-balance model breaks down since the energy that should be confined to a few small laser-heated spots is spread over the entire hohlraum wall, predicting a more uniform drive. The effect of this early nonuniformity on target performance is not expected to be significant, however, since little energy irradiates the capsule at these times. Also, Eq. (2) implies that, after the laser turns off, the radiation temperature (and thus the drive nonuniformity) immediately goes to zero, while in reality the hohlraum wall acts as a heat reservoir, radiating stored energy well after the end of the laser pulse. This is important for the targets discussed below, where peak compression and neutron production occur several hundred picoseconds after the end of the laser pulse.

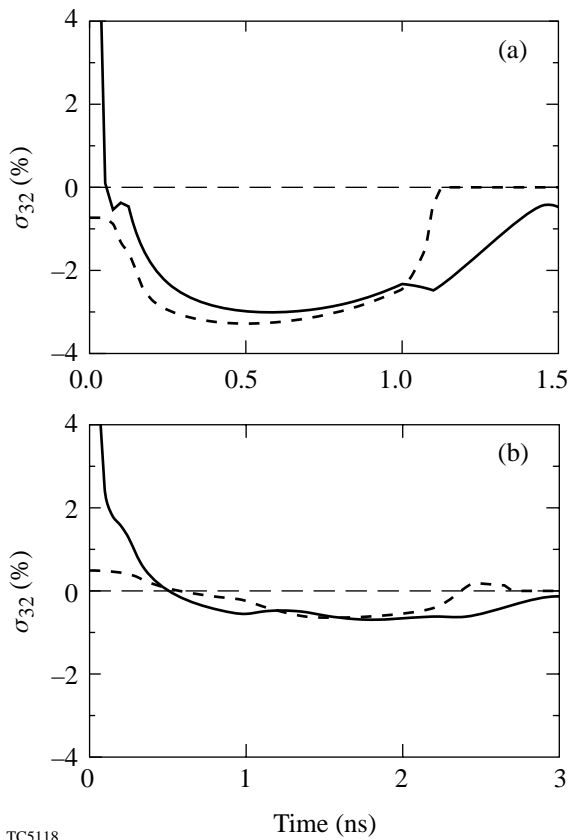


Figure 82.45  
 Predicted drive uniformity on the capsule in a tetrahedral hohlraum. The  $\sigma_{\text{rms}}$  present in the dominant spherical-harmonic mode  $Y_{32}$  is plotted versus time for (a) the initial scale-1 design for a 1-ns square pulse and (b) the optimized scale-1.2 PS22 design. The amplitude of  $\sigma_{32}$  gives the rms nonuniformity when all other modes are absent. The dashed curves were produced by the energy-balance model described in the **Fundamental Features of the Code BUTTERCUP** section, and the solid curves were calculated by the wall-diffusion model described in the **Radiation Transport and Diffusion** section.

The first experimental tetrahedral hohlraums (shot on OMEGA in March 1997) were designed to have the same surface area and total LEH area as a standard cylindrical Nova hohlraum, thus giving comparable drive temperatures for the same laser pulse. This “scale-1” tetrahedral hohlraum had  $R_{\text{case}} = 1150 \mu\text{m}$  and  $R_{\text{LEH}} = 450 \mu\text{m}$ . The predicted radiation-drive uniformity of 2% to 3% for a 1-ns flat-top pulse was certainly good by most ICF standards,<sup>24,25</sup> but the tetrahedral geometry on OMEGA was capable of much better uniformity. With the help of *BUTTERCUP*, the tetrahedral hohlraum was redesigned to give the best-possible drive uniformity while still maintaining reasonable radiation temperatures and sufficient clearance for the laser beams.<sup>26</sup> The optimized design, known as a scale-1.2 hohlraum, had  $R_{\text{case}} = 1400 \mu\text{m}$ ,  $R_{\text{LEH}} = 350 \mu\text{m}$ , and different laser pointing parameters. The optimized design had a total LEH area of  $1.54 \text{ mm}^2$ , a little less than the  $2.26 \text{ mm}^2$  of a standard Nova hohlraum. Additionally, the shaped laser pulse PS22 was used to achieve more-efficient implosions and reduce laser-plasma instabilities in the hohlraum. Figures 82.45(a) and 82.45(b) correspond to the initial and optimized designs, respectively.

The difference between a peak drive uniformity of 3% and one of 1% is apparent when comparing experimental images of the imploded cores, as shown in Fig. 82.46. The initial design, with  $\sigma_{32} \sim 3\%$  at the peak of the drive, results in a core with a clear triangular shape [Fig. 82.46(a)], corresponding to weaker

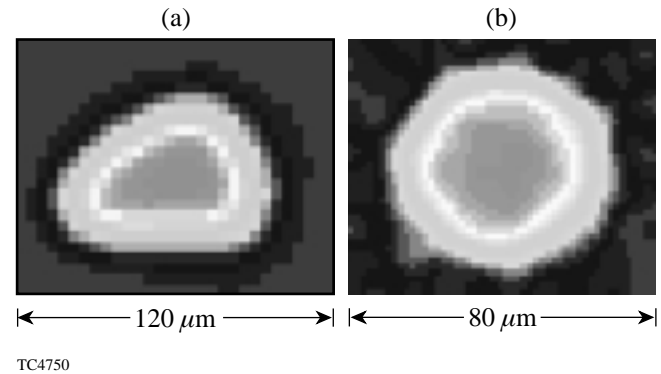


Figure 82.46  
 Experimental x-ray images<sup>11</sup> of imploded capsule cores for the drive conditions of Fig. 82.45, viewed through an LEH. The initial design (a) has a predicted average drive uniformity of  $\sigma_{32} \sim 2\%$  to  $3\%$ , causing a characteristic triangular core, while the optimized design (b) produced a nearly round core with a drive uniformity of  $\sigma_{32} < 1\%$ . The three points in the triangular image are oriented toward the other three LEH’s. Image (a) was taken with a time-integrating pinhole camera and image (b) with an x-ray framing camera.

drive pressure at the points on the capsule that directly face the LEH's. The resulting 3-D tetrahedron-shaped core looks like a triangle when viewed along the axis of one of its vertices (through a LEH). With the optimized design, the imploded core is almost perfectly round [Fig. 82.46(b)], representing one of the most-uniform indirect-drive implosions recorded to date.

The optimized design for OMEGA benefits from a favorable ratio of the case radius to the capsule radius. The tradeoff is a lower coupling efficiency due to the ~40% extra wall area. The tetrahedral geometry on OMEGA has the advantage, however, that all 60 beams can be used, compared with a maximum of 40 for cylindrical hohlraums. On the NIF, the tradeoff between uniformity and efficiency will be a key issue, especially for capsules with the larger convergence ratios that will be required.

### Radiation Transport and Diffusion

The simple zero-dimensional model described in the previous section works well for designing hohlraum targets and estimating the radiation-drive uniformity, but it has some significant shortcomings. For one, the assumption of a single, spatially independent albedo tends to break down early in the laser pulse, when the cold, unirradiated sections of the wall typically have a much lower albedo than the laser-heated spots.<sup>27,28</sup> The energy-balance model also fails at later times, after the end of the laser pulse, giving a radiation temperature of zero. Additionally, the dependence on an external calculation or experimental measurement of the time-varying albedo limits *BUTTERCUP*'s ability to scan through a wide variety of pulse shapes and hohlraum designs. Finally, while the predicted time-dependent drive uniformity agrees qualitatively with experimental data, it unfortunately provides no means for quantitative comparison.

To address these limitations, *BUTTERCUP* has been expanded to model the gold wall as a 2-D grid of mass elements, each with a different temperature profile and radiation brightness. Each point on this 2-D grid is treated as a separate problem in 1-D planar geometry, with the radiation transport into the wall modeled by solving an energy diffusion equation. The boundary zone of each 1-D section is driven by a radiation source from other portions of the hohlraum wall and, for the directly irradiated sections, a laser source. The deposited energy then propagates into the wall (along  $x$ ) according to the diffusion equation, assuming a single radiation and matter temperature  $T_w(x,t)$  at each point in the wall. This treatment is similar to that of Tsakiris,<sup>27</sup> except that he used 1-D self-similar solutions rather than individual 1-D calculations.

Following Rosen<sup>29,30</sup> we use the diffusion equation

$$\frac{\partial}{\partial t}(\rho\epsilon) = \frac{\partial}{\partial x} \left[ \frac{c}{3} \lambda_R \cdot \frac{\partial}{\partial x} (aT_w^4) \right] \quad (6a)$$

in the interior of the wall, and apply

$$\begin{aligned} \frac{\partial}{\partial t}(\rho\epsilon\Delta x) = & \underbrace{\frac{c}{3} \lambda_R \cdot \frac{\partial}{\partial x} (aT_w^4)}_{\text{diffusion}} \underbrace{- \sigma T_w^4}_{\text{loss to hohlraum cavity}} + \underbrace{\eta_l I_l}_{\text{laser source}} \\ & + \underbrace{\frac{1}{\pi} \int \sigma T_w^4(\mathbf{r}) \cos\theta d\Omega}_{\text{radiation source}} \end{aligned} \quad (6b)$$

to the boundary zone. Here  $\rho\epsilon$  is the energy density of the wall material (ergs/cm<sup>3</sup>), which scales as  $T_w^{1.5}$ , the diffusion coefficient is  $1/3 c\lambda_R$ , and  $aT_w^4 [a = 4\sigma/c]$  is the radiant energy density. The Rosseland mean free path  $\lambda_R$  is given as a function of temperature and density.<sup>29</sup> The last term in Eq. (6b) is the radiation flux seen by the point on the wall, integrated over all solid angles (i.e., over all other boundary zones on the hohlraum wall). This term couples together all the individual 1-D diffusion calculations: each boundary zone emits into the hohlraum cavity a flux  $\sigma T_w^4(\mathbf{r})$  [brightness  $\sigma T_w^4(\mathbf{r})/\pi$ ], of which a large fraction provides a source for other boundary zones and a smaller fraction is lost to the capsule and LEH's.

In Eq. (6b),  $\Delta x$  is the thickness of the boundary zone, where the energy from the laser and radiation source terms is deposited. In the limit of  $\Delta x \rightarrow 0$  the left-hand side of Eq. (6b) tends to zero (i.e., the boundary cell has negligible heat capacity), and Eq. (6b) then acts as a boundary condition on  $\partial T_w^4/\partial x$  for the diffusion equation. It is for this reason that the numerical solutions of Eq. (6) are convergent (i.e., independent of  $\Delta x$ ) as  $\Delta x \rightarrow 0$ . In this limit, the laser source and the incident radiation from the other zones on the hohlraum wall balance the radiative loss into the hohlraum cavity and the diffusive loss into the hohlraum wall.

The term  $\int \sigma T_w^4(\mathbf{r}) \cos\theta d\Omega$  is calculated in a way very similar to the view-factor integration used to determine the radiation incident on the capsule. Figure 82.47 shows a schematic representation of this algorithm, where the incident radiation intensity at a given point  $P$  on the hohlraum wall is determined by tracing rays over all solid angles and summing the relative brightness detected from each direction. Of course, the LEH's do not contribute anything to the incoming radia-

tion, and the low-albedo capsule acts effectively as a shield, blocking the radiation transfer between opposite sections of the hohlraum wall. If no capsule were present, the spherical geometry would provide perfect radiation uniformity incident on every point of the wall not directly heated by a laser source, regardless of the spatial emission distribution or the size of the LEH's, as long as the spectral brightness is independent of angle (i.e., Lambertian) as is the case for blackbody radiation.<sup>27</sup> This makes tetrahedral hohlraums particularly well suited for nonimplosion experiments that require a uniform x-ray source for driving foils or other packages mounted on the hohlraum wall.

Here, as in the previous section, the emitted wall brightness is taken to be  $\sigma T_w^4(\mathbf{r})/\pi$  independent of angle. This is probably a good assumption except at very early times when the steep gradient of  $T_w$  within the wall (see Fig. 82.48 below) results in different angles viewing different values of  $T_w$  at about one optical depth into the wall. An angle-dependent brightness could be added to the model.

It is instructive to compare Eq. (6b) with Eq. (3a), obtained for the simpler model of the previous section. The radiation source term of Eq. (6b) may be written as  $\sigma T_R^4(\mathbf{r})$ , defining an effective hohlraum temperature  $T_R(\mathbf{r})$  as seen by a point  $\mathbf{r}$  on

the wall that is analogous to  $T_r$  of the previous section. Generally the spatial dependence of  $T_R(\mathbf{r})$  is weak: as stated previously,  $T_R(\mathbf{r})$  would be independent of  $\mathbf{r}$  for a spherical hohlraum in the absence of a capsule. This provides justification for the use of a single  $T_r$  in the previous section to describe the radiation field in the cavity. It is also possible to define a local albedo  $\alpha_2(\mathbf{r}) \equiv 1 - \beta_2(\mathbf{r})$  by requiring  $\beta_2(\mathbf{r})\sigma T_R^4(\mathbf{r})$  to equal (-1) times the first term on the right-hand side of Eq. (6b), i.e., the diffusive loss into the wall. With these definitions, the flux of x rays emitted into the hohlraum cavity becomes

$$\sigma T_w^4 = \alpha_2(\mathbf{r})\sigma T_R^4(\mathbf{r}) + \eta_l I_l(\mathbf{r}), \tag{7}$$

which compares closely with the right-hand side of Eq. (3a). The first model can thus be expected to best match the second model if  $\alpha_w$  is taken to be the average of  $\alpha_2(\mathbf{r})$  over the hohlraum wall.

An example of the nonlinear heat wave (Marshak wave<sup>31</sup>) described by Eq. (6) is shown in Fig. 82.48, for an unirradiated section of the gold wall. Here the wave is plotted at 100-ps intervals for an illustrative calculation in which a hohlraum is driven by a 1-ns square pulse. The penetration rate is commonly approximated as being proportional to  $\sqrt{t}$ ,<sup>29,31,32</sup>

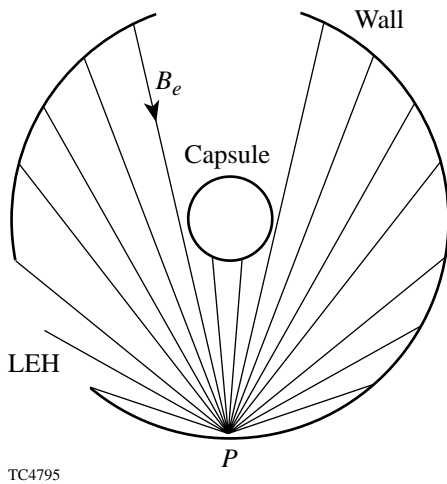


Figure 82.47 Schematic of the view-factor algorithm used by the code BUTTERCUP to calculate radiation transfer within the hohlraum. The x-ray flux incident at each point  $P$  on the wall is determined by integrating the visible brightness  $B_e$  over a hemisphere of solid angle. The low-albedo capsule acts effectively as a shield, blocking the radiation transfer between opposite sections of the hohlraum wall.

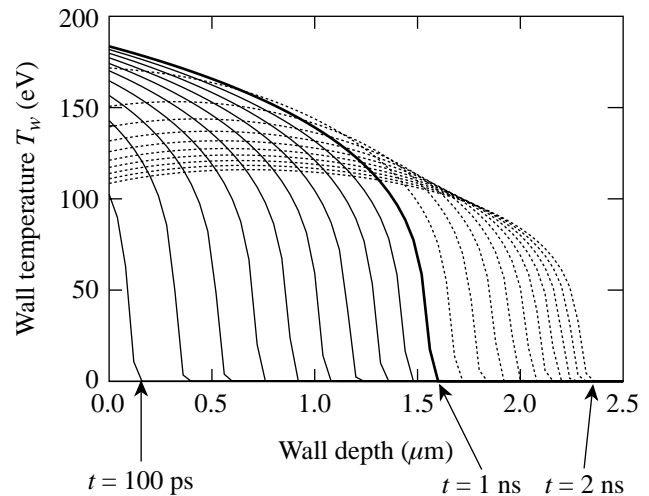


Figure 82.48 Wall temperature  $T_w$  as a function of distance into the gold wall, plotted at 100-ps intervals throughout a 1-ns square-pulse drive shot. For the duration of the laser pulse, the temperature at the boundary rises as the Marshak radiation wave propagates into the hohlraum wall; it then decreases as the wall cools after the laser is turned off.

although this approximation breaks down when blowoff and other effects are included.<sup>16,29</sup> Even after the laser is turned off, the radiation continues to diffuse into the wall; however, much of the energy in the radiation field within the hohlraum cavity leaks out through the LEH's, lowering the temperature at the boundary surface. Note that it is not necessary to calculate the albedo explicitly in this model: the radiation emitted into the hohlraum from each boundary cell is given directly from the  $T_w$  there as  $\sigma T_w^4$ .

With the temperature  $T_w$  defined at each point on the hohlraum wall, it is straightforward to predict what the experimentally measured radiation temperature  $T_r$  will be as a function of time. For the tetrahedral hohlraum experiments on OMEGA,  $T_r(t)$  was measured with the multichannel soft x-ray diagnostic Dante.<sup>33</sup> This looked directly through one of the LEH's, viewing a combination of laser spots and unirradiated wall, representative of what the capsule should see, and thus eliminating the need for "albedo corrections."<sup>34</sup> For a 22.0-kJ PS22 drive shot (i.e., a shot without a capsule), the theoretical and experimental temperatures were in close agreement, as shown in Fig. 82.49.<sup>11</sup> The data are from a scale-1.2 tetrahedral hohlraum with 500- $\mu\text{m}$ -radius LEH's (larger than the 350- $\mu\text{m}$  LEH's used for the optimized implosions). For the *BUTTERCUP* calculation, the experimentally measured SBS backscat-

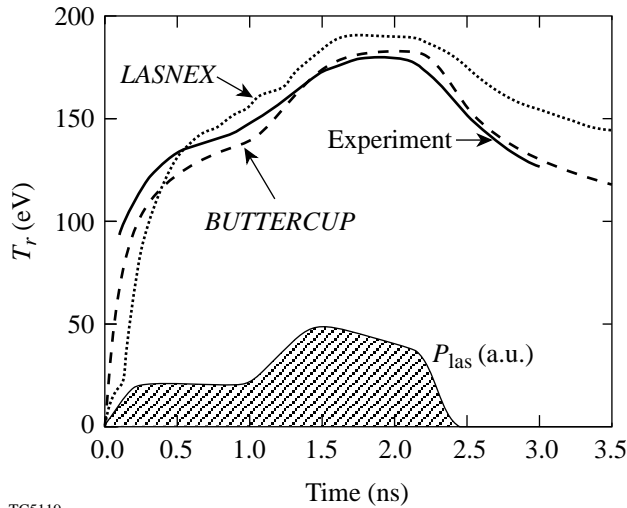
ter fraction of 6% was taken out of the input laser energy. The close agreement with experiment indicates that the basic hohlraum energetics can be accurately modeled with *BUTTERCUP*'s relatively simple combination of diffusion and view-factor calculations.

By this method of performing multiple 1-D diffusion calculations on a 2-D grid covering the hohlraum wall, and coupling them together through view-factor radiation transport, *BUTTERCUP* provides a 3-D description of the time-dependent radiation uniformity on the capsule. This approach allows remarkably rapid simulations without sacrificing physical accuracy. Since fully 3-D radiation-hydrodynamics codes typically take hundreds of CPU hours to do a single simulation on even the fastest supercomputers, pseudo-3D calculations like those presented here will be increasingly valuable. The speed of *BUTTERCUP* also provides the ability to perform multiple simulations with different hohlraum parameters, making the code an ideal tool for developing new target designs.

The evaluation of the effects on uniformity of pointing errors and beam imbalance provides a good example of the type of problem for which *BUTTERCUP* is ideally suited.<sup>35</sup> With each point on the hohlraum wall being modeled independently, the computational overhead associated with changing the beam pointings and energies is very small, even though the tetrahedral symmetry is lost.

One limitation of the model is the assumption of an idealized blackbody radiation spectrum. For example, it would not be correct to treat M-band radiation from multi-keV laser-heated plasma with Eq. (6), which emits blackbody radiation into the hohlraum with the temperature of the dense wall plasma. Here, following Eq. (3c), it would be reasonable to assume that half of this radiation is emitted into the hohlraum and half is lost in the wall (with  $\alpha'_w = 0$ ). The flux and uniformity of M-band radiation on the capsule could nevertheless be calculated with the model of the previous section using  $\alpha'_w = 0$  and taking  $\eta'_l$  to give the observed emission of M-band radiation from the hohlraum wall.

We conclude this section by demonstrating that the simple energy-balance model described in the previous section provides a remarkably accurate description of the radiation temperature  $T_r(t)$  when given a single, spatially averaged albedo as a function of time. This may be seen from Fig. 82.50, which plots  $T_r(t)$  for (a) the initial design (1-ns square pulse) and (b) the optimized design (PS22 shaped pulse). The solid curves correspond to the more accurate wall-diffusion model and the



TC5119

Figure 82.49  
Hohlraum radiation temperature  $T_r$  as a function of time for a 22.0-kJ PS22 drive experiment with 500- $\mu\text{m}$ -radius LEH's. The *LASNEX* predictions (dotted curve) and the experimental data (solid curve) measured by the Dante multichannel, soft x-ray diagnostic are taken from Ref. 11. The dashed curve is the *BUTTERCUP* calculation, with the input laser power  $P_{\text{las}}$  adjusted for the experimental SBS backscatter fraction of 6%.

dashed curves to the energy-balance model. Here we use the spatially averaged albedo (dotted curves) calculated by the wall-diffusion model as input for the energy-balance model. For both cases the albedo rises rapidly to about 0.8. For the duration of the laser pulse, the two models agree very closely, suggesting a close equilibrium between the incident laser power and the radiation field. After the laser pulse ends, the albedo becomes greater than unity since the cooling wall emits more energy than it absorbs. This is also the point at which the energy-balance model breaks down completely, as the  $\beta_w$  in Eq. (2) becomes negative, the left-hand side of Eq. (2) becomes zero, and the wall acts like a radiation source rather than a sink.

**Capsule Implosions**

Given the 3-D, time-dependent radiation field incident on the capsule, BUTTERCUP also provides a pseudo-3D model of

the actual hydrodynamic capsule implosion within a tetrahedral (or cylindrical) hohlraum. For a given x-ray drive intensity  $I_r(\theta, \phi, t)$  on the surface of the capsule, the incident radiation is treated as a blackbody spectrum and deposited into the plastic shell in multiple energy and angular groups. Like the pseudo-3D treatment of the gold wall, the capsule is modeled as a collection of 1-D calculations, each with its own radiation source term. Unlike the treatment of the gold wall (where just the Rosseland opacity is used), however, the radiation transport within the capsule plasma is modeled in greater detail using multigroup opacities.<sup>36</sup>

Each angular wedge of the capsule is modeled as a spherically symmetric problem with 1-D Lagrangian hydrodynamics. About 100 material zones are typically used in the radial direction, with roughly half in the shell and half in the fuel. The radiation energy from the hohlraum wall is deposited in the CH plasma using an  $S_N$  algorithm, which divides the incident radiation into different angular groups,<sup>37</sup> as is represented by Fig. 82.51. The x rays that are nearly normal to the surface penetrate deeper into the shell, while the higher-angle x rays deposit the majority of their energy closer to the outside of the capsule. Since opacities are often quite sensitive to photon energy, the Planckian spectrum from the hohlraum wall is divided into multiple frequency groups, each containing a fraction of the blackbody radiation flux  $\sigma T_r^4$  and each penetrating the plastic shell to a different depth.

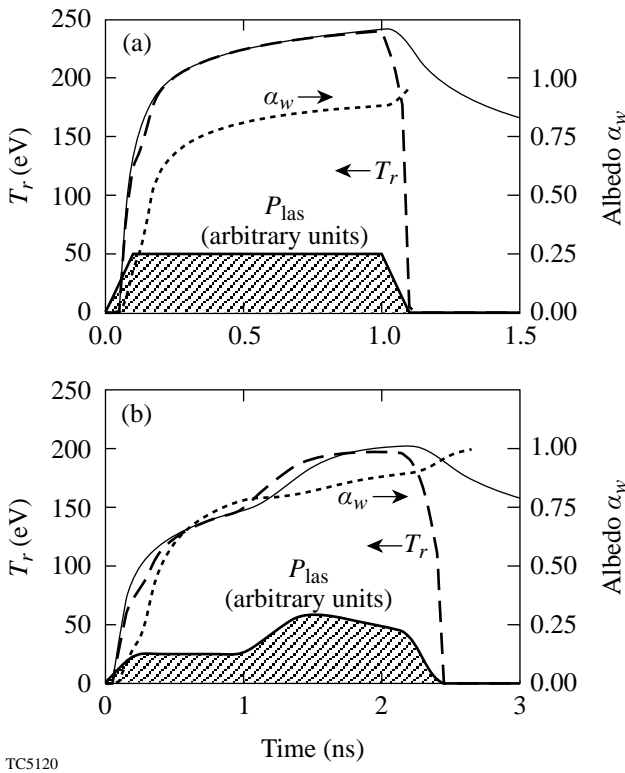


Figure 82.50 Hohlraum radiation temperature  $T_r$  as a function of time for two implosion experiments: (a) scale-1 hohlraum with a 30-kJ, 1-ns square pulse (initial design); (b) scale-1.2 hohlraum with a 24.6-kJ, PS22 shaped pulse (optimized design). The wall-diffusion model produced the solid curves and a time-dependent, spatially averaged albedo, defined here as the total power radiated from the hohlraum wall divided by the total radiative power incident on the wall (dotted curve); this albedo was then used as input in the energy-balance model to give the dashed curves.

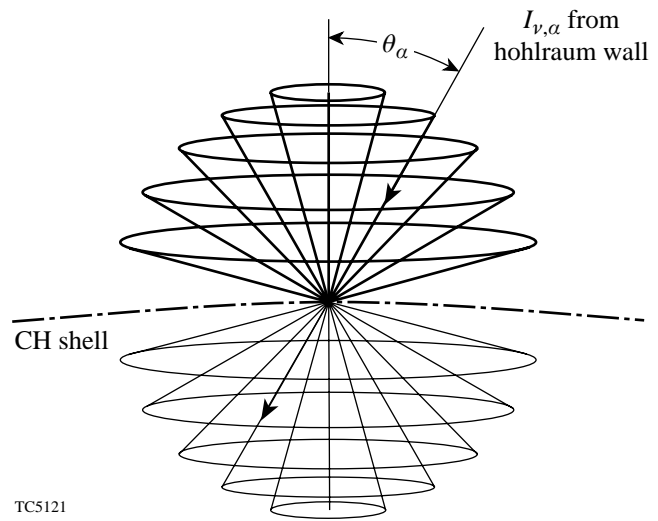


Figure 82.51 Multiple angular groups used to model radiation absorption in the capsule shell. X rays with small angles of incidence  $\theta_\alpha$  penetrate deeper into the ablating plasma, while higher-angle groups deposit their energy closer to the outside of the capsule.

*BUTTERCUP* models the capsule implosion by solving the 1-D spherical Lagrangian hydrodynamic equations, including electron thermal diffusion and multigroup radiation diffusion within the capsule. The basic hydrodynamic equations in a spherically symmetric geometry are<sup>37</sup>

$$\begin{aligned}\frac{\partial r}{\partial t} &= v, \\ \frac{\partial v}{\partial t} &= -4\pi r^2 \frac{\partial}{\partial m} (P + Q), \\ \frac{\partial \varepsilon}{\partial t} &= -4\pi \frac{\partial}{\partial m} (r^2 v) (P + Q),\end{aligned}\quad (8)$$

where  $P$  is the hydrodynamic fluid pressure,  $Q$  is the “artificial viscous stress,”  $r$  and  $v$  are the position and velocity of Lagrangian zone markers, and  $\partial m$  is the differential mass element. For each step of the calculation,  $P$  and the specific energy  $\varepsilon$  (ergs/g) are determined from the *SESAME* equation-of-state tables.<sup>38</sup> The electron thermal diffusion is calculated using

$$\frac{\partial}{\partial t}(\rho\varepsilon) = -\nabla \cdot Q_e = \nabla \cdot (\kappa_0 \nabla T_e), \quad (9)$$

where  $T_e$  is the electron temperature, here assumed to be the same as the ion temperature  $T_i$ ;  $\kappa_0$  is the thermal diffusion coefficient, a function of the temperature, density, and ionization of the plasma.

The multigroup radiation transport is modeled in two steps: first by angular  $S_N$  absorption from the hohlraum wall and then with a mean-free-path diffusion approximation within the capsule. The absorption is determined<sup>39</sup> by the opacity  $\kappa'_\nu$  corrected for stimulated emission [ $\kappa'_\nu = \kappa_\nu(1 - e^{-h\nu/kT})$ ] and the incident intensity  $I_\nu$  for each frequency group:

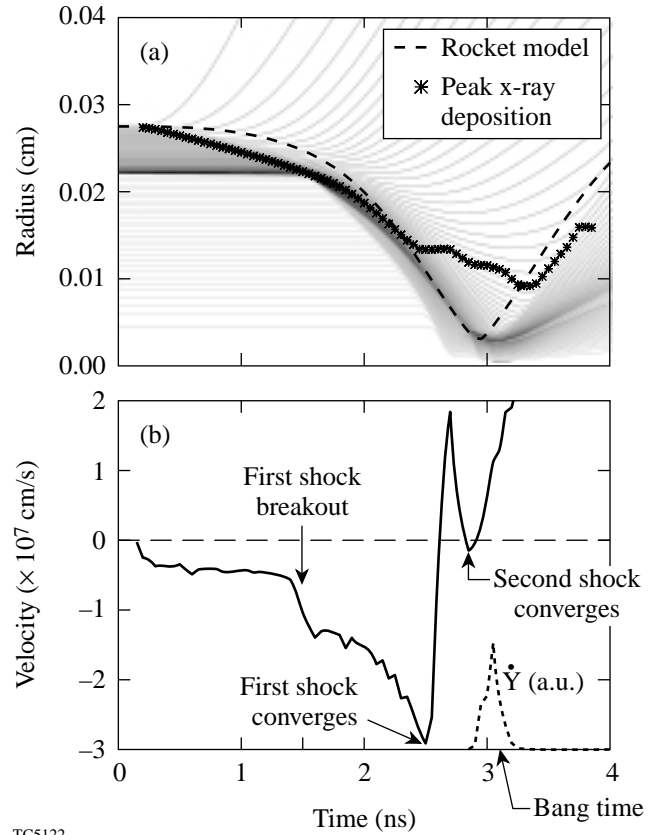
$$\frac{dI_\nu}{ds} = -\kappa'_\nu I_\nu, \quad (10)$$

where  $s$  measures distance in the appropriate direction. Thus, in a region of constant opacity,  $I_\nu$  falls off exponentially. The internal diffusion equation, including emission and reabsorption, is

$$\frac{\partial U_\nu}{\partial t} - \nabla \cdot (D_\nu \nabla U_\nu) = c\kappa'_\nu (U_{\nu p} - U_\nu), \quad (11)$$

where  $U_\nu$  is the spectral radiation energy density (ergs/cm<sup>3</sup>/unit frequency),  $U_{\nu p}$  is the Planckian radiation energy density for a given temperature,  $D_\nu$  is the frequency-dependent diffusion constant ( $= c/3\kappa'_\nu$ ), and  $c$  is the speed of light.

*BUTTERCUP* uses opacity data from the Los Alamos Astrophysical Tables,<sup>36</sup> which include opacities for values of  $h\nu/kT$  between 0.00125 and 30000. For the small number of points outside this regime, the data are interpolated between the cold opacity and the closest-known tabular opacity. As shown in Fig. 82.52(a), the peak x-ray power absorption during the laser pulse occurs in the shell near the steepest density



TC5122

Figure 82.52

(a) Evolution of 1-D Lagrangian interface markers during a PS22 implosion with 50 atm of DD fuel inside a standard Nova capsule. The region of peak x-ray power absorption closely follows the steepest density gradient in the ablating shell for the duration of the laser pulse. The dashed curve shows the trajectory of a thin shell predicted by the 0-D rocket model. (b) Velocity of the shock front propagating through the capsule as a function of time. The first shock breaks out from the shell into the DD fuel at 1.5 ns and converges on the origin at 2.6 ns, followed by the second shock convergence at 2.9 ns. Stagnation and bang time, the time at which the neutron production rate  $\dot{Y}$  peaks, occur at  $t \sim 3$  ns.

gradient, unlike direct-drive implosions where the laser energy is deposited in the plasma corona and must be transported inward toward the ablation front. Even after the laser pulse ends, the hohlraum still provides significant radiation drive, penetrating deep into the ablating shell.

Indirect-drive capsule implosions involve both radiative and shock heating in addition to the adiabatic heating and cooling of the plasma.<sup>40</sup> The velocity of the shock front, defined as the point of maximum artificial viscous pressure, is shown as a function of time in Fig. 82.52(b), a negative value indicating convergence inward. The first shock is driven by the ~150-eV radiation temperature produced during the foot portion of the laser pulse. When it breaks out on the inside of the plastic shell, it experiences “velocity multiplication,” a general phenomenon that occurs whenever a shock wave crosses a boundary from a denser material to a lighter material. Figure 82.52(b) shows that the shock speed jumps from  $6 \times 10^6$  cm/s to  $1.2 \times 10^7$  cm/s around  $t = 1.4$  ns. Then, as the radiation drive from the hohlraum increases near the peak of the laser pulse, the shell and fuel accelerate inward until 2.6 ns, when the first spherical shock wave converges at the origin and sends a reverse shock outward through the fuel. At 2.75 ns, this reflected shock meets the imploding plastic shell, which continues to converge until stagnation around 3.0 ns.

The point of stagnation closely corresponds to the peak core temperature and also to the time of peak neutron production, referred to as the “bang time.” The density and temperature profiles of the core at bang time are shown in Fig. 82.53, plotted

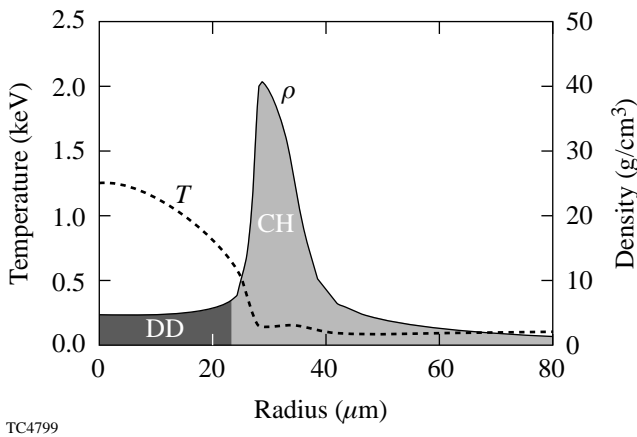


Figure 82.53 Temperature and density profiles for the DD fuel and surrounding CH ablator in the capsule core at bang time (3.0 ns), which closely corresponds to hydrodynamic stagnation. The fuel is assembled in a small, hot region of low-density gas surrounded by the colder, dense plastic pusher. The convergence ratio ( $R_i/R_f$  for the CH-DD interface) for this PS22 implosion is about 10.

as functions of distance from the capsule center. The results shown are from a standard PS22 capsule implosion at  $t = 3.0$  ns, with the DD fuel assembled in a hot, central region surrounded by the cold, dense plastic shell. The radius of the fuel–pusher interface is  $R_f = 23 \mu\text{m}$ , giving a convergence ratio of  $C_R \sim 10$ .

*BUTTERCUP* calculates the neutron yield from the  $D(D,n)^3\text{He}$  reaction using Hively’s formulas for Maxwellian distributions.<sup>41</sup> Since this reaction is so strongly dependent on temperature,<sup>42</sup> almost the entire yield occurs during a short (~200-ps) time when the fuel reaches its maximum temperature and density. Figure 82.54 shows this nuclear burn profile as a function of time for a standard PS22 implosion with a bang time of 3.0 ns. The “foot” of the neutron pulse corresponds to the second spherical shock converging at the origin, as shown in Fig. 82.52(b), which raises the average fuel temperature to 0.7 keV. This is followed by the peak compression and stagnation, when most of the neutrons are produced. After bang time, the core rapidly cools by thermal and radiative diffusion into the surrounding cold material, as well as through adiabatic expansion.

The spherical uniformity of capsule implosions is frequently assessed by comparing the experimental fusion yields to those predicted by a purely one-dimensional calculation. Usually referred to as “yield over clean” (YOC), this ratio provides an indication of how the capsule’s 3-D distortion affects the neutron yield and thus the success of the implosion.<sup>43,44</sup> The cause of core distortion may be understood on

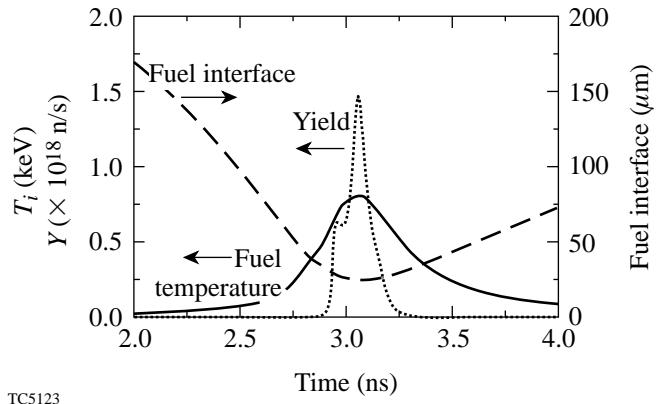


Figure 82.54  $D(D,n)^3\text{He}$  fusion yield as a function of time for a standard implosion driven with PS22. Also shown are the average fuel temperature and the radius of the fuel–pusher interface. The very strong temperature dependence of the fusion rate results in almost all neutron production occurring within about 200 ps.

a very simple level. Following Wallace,<sup>45</sup> the implosion velocity scales as

$$V_{\text{imp}} \propto T_r^{1.5} \propto I_r^{3/8}, \quad (12)$$

so for a peak-to-valley variation in drive uniformity of 10% (typical for  $\sigma_{\text{rms}} = 2.5\%$ ), there should be a peak-to-valley difference of about 4% for the implosion velocity. For a convergence ratio of 10, this means that at the point of maximum compression, the core distortion—as measured by  $a/b$ , the ratio of major to minor axes—will be 1.56. For a peak-to-valley difference of 2% in drive uniformity, however, the resulting core distortion will be only 1.07, or nearly round. For a high-convergence capsule with the same drive uniformity and  $C_r = 30$ ,  $a/b = 1.28$ . While this model is conceptually helpful to understanding the relation between drive uniformity, convergence, and core distortion, we find that it generally overpredicts the values for  $a/b$ . This is probably because it omits the deceleration and stagnation caused by the gas pressure of the compressed fuel, as well as 3-D hydrodynamic smoothing effects that take place during the implosion, causing the relation in Eq. (12) to break down.

*BUTTERCUP* uses a pseudo-3D algorithm to model more accurately the effects of nonuniform drive on a capsule implosion and thus predict the core deformation as well as the neutron yield degradation. Just as the hohlraum wall is modeled in pseudo-3D by coupling a large number of 1-D calculations, the capsule is modeled by performing many 1-D spherical implosion calculations at the same time and coupling them together. As with earlier work that investigated deviations from uniform spherical implosions using a spherical-harmonic expansion,<sup>46</sup> this approach is best suited to implosions that are close to spherically symmetric.

To divide the capsule into multiple 1-D wedges of equal solid angle, we take advantage of the unique dodecahedral symmetry of the OMEGA target chamber. As mentioned previously, the 60 laser beams can be divided into 12 groups of five independent beams. Only these 5 beams need to be explicitly modeled in the hohlraum; the other 11 groups can be added by rotating the original group, greatly simplifying the 3-D problem. Similarly, the spherical capsule can be divided into 12 pentagonal wedges, all interchangeable through transformations in the dodecahedral rotational group. Figure 82.55 shows schematically how the sphere is divided into pentagonal wedges, only one of which is actually modeled. This wedge corresponds to one group of five laser beams and a section of the hohlraum wall including one-third of an LEH.

The pentagonal wedge of the capsule is then divided into triangular slices, each with the same solid angle and all converging at the same origin. For convenient division into symmetric wedges, 10, 30, or 90 triangular slices are typically used. All of these slices are modeled simultaneously with the spherical 1-D Lagrangian hydrodynamic model described previously. Each has a unique radiation-drive input, determined by the dynamic model of the hohlraum wall and the 3-D view-factor radiation transport. For most tetrahedral implosions, the radiation drive can be thought of as nearly uniform, with a small, time-dependent  $Y_{32}$  perturbation. This will in turn cause a nearly spherical implosion, with  $Y_{32}$  variations in the hydrodynamic variables throughout the capsule. This is very convenient since the spherical harmonic functions are solutions to the angular portion of the diffusion equation in a spherical geometry:<sup>47</sup>

$$\frac{\partial}{\partial t} f(r, \theta, \phi, t) = \nabla \cdot D(r) \nabla f(r, \theta, \phi, t). \quad (13)$$

For short times  $\Delta t$ , over which the diffusion constant  $D(r)$  can be treated as static, solutions are eigenfunctions of the form

$$f(r, \theta, \phi, \Delta t) = R(r, \Delta t) U_r(\theta, \phi, \Delta t), \quad (14)$$

where

$$U_r(\theta, \phi, \Delta t) = \sum_{l,m} c_{lm} Y_{lm}(\theta, \phi) \exp\left[\frac{-l(l+1)}{r^2} D(r) \Delta t\right] \quad (15)$$

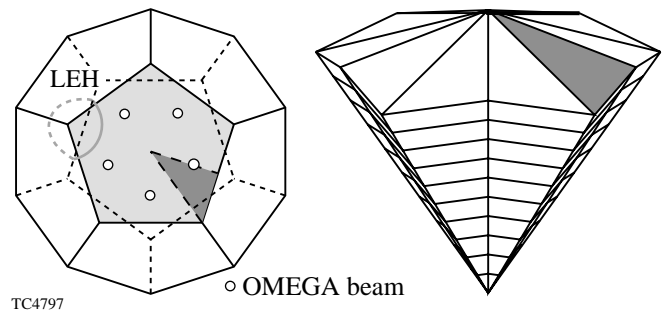


Figure 82.55 Geometry used by *BUTTERCUP* to model a 3-D capsule implosion in a tetrahedral hohlraum on OMEGA. Using the natural dodecahedral symmetry, the spherical target is divided into 12 pentagonal-shaped wedges. Each wedge contains one-third of an LEH and five independent laser beams. This pentagonal wedge of the capsule is in turn divided into multiple triangular wedges of equal solid angle. Each triangular wedge is modeled with a single 1-D hydrodynamic calculation and is then coupled to neighboring wedges.

and  $R(r, \Delta t)$  is calculated with the 1-D spherical hydrodynamics of Eqs. (8)–(11). In *BUTTERCUP*,  $f(r, \theta, \phi, t)$  represents either the electron temperature or the energy density of a radiation group, and Eq. (15) is used to calculate its evolution over short periods of time  $\Delta t$ . For tetrahedral hohlraums on OMEGA, only the  $Y_{lm}(\theta, \phi)$  spherical-harmonic functions with dodecahedral symmetry will have nonzero coefficients in the sum. Just as the  $Y_{32}$  moment dominates the radiation incident on the capsule, it is also the primary term in the angular diffusion equation and typically the only term explicitly calculated.

For the angular portion of each 3-D diffusion step, the Lagrangian hydrodynamic variables are projected onto an orthogonal, Eulerian-type grid. This allows *BUTTERCUP* to solve Eq. (15) for each concentric spherical shell of material, as opposed to lateral diffusion between Lagrangian zones with the same radial index that may be located at different physical radii. After the angular diffusion calculation, the new values of the temperature are projected back onto the pseudo-3D Lagrangian grid. This alternates with the separate 1-D hydrodynamic calculations (including diffusion in the  $r$  direction) that change the values of  $R(r)$  and  $D(r)$  for each angular zone, which are then used as input for the next iteration of the 3-D diffusion calculation. In this way, the triangular slices of the capsule are coupled to produce a pseudo-3D implosion simulation.

Since this algorithm does not include lateral mass transport, it cannot model more-complicated 3-D phenomena like shock dispersion and hydrodynamic instabilities. Furthermore, since the converging radiation shock wave is not perfectly spherical, there can be sharp discontinuities in the hydrodynamic variables as the wavefront propagates through the material. At a given radius near the shock front, some material may be cold and uncompressed, while the material in a neighboring zone may have been heated and compressed by the shock. At this point, the assumption of a smooth  $Y_{32}$  perturbation in the temperature breaks down; however, for the tetrahedral hohlraum implosions performed on OMEGA, we find that this pseudo-3D model provides reasonable predictions for experimental observations.

Specifically, *BUTTERCUP* was used to model a set of recent experiments on the OMEGA laser that utilized tetrahedral hohlraums to achieve high-convergence implosions.<sup>48,49</sup> Indirect-drive capsules with convergence ratios as high as 20 to 30 have been shot previously on Nova<sup>43</sup> and OMEGA<sup>50</sup> in cylindrical geometry, typically giving YOC measurements of 5% to 25%. By using the improved drive uniformity available with tetrahedral hohlraums, it was hoped to eliminate the

effects of low-order nonuniformity on the fusion-yield degradation. For the first series of high-convergence tetrahedral experiments conducted in September 1998 and reported in Refs. 48 and 49, convergence ratios of about 10 to 20 were achieved, with values of YOC similar to earlier results using cylindrical targets with the same convergence. The high-convergence capsules were designed by varying the initial DD fill pressure, with lower-pressure capsules giving higher convergence. The experiment used 550- $\mu\text{m}$ -diam capsules with 55- $\mu\text{m}$  CH shells filled with 50, 25, and 8 atm of DD gas, corresponding to theoretical convergence ratios of 9, 11, and 16, respectively. They were driven with all 60 OMEGA beams with pulse shape PS22, delivering 21 to 25 kJ of UV light into the hohlraum.

Figure 82.56(a) shows how the predicted neutron yields and convergence ratios depend on the DD fill pressure. Low-pressure capsules not only converge to a smaller radius, but they also reach higher core temperatures, leading to higher fusion yields even with significantly less fuel. *BUTTERCUP*'s yield predictions with 3-D effects included are also shown. As expected, for higher-convergence implosions, the predicted 3-D yields are lower with greater degradation from the 1-D prediction. Figure 82.56(b) shows a plot of YOC versus convergence ratio, including both experimental<sup>49</sup> and predicted YOC. A quantitative summary of the predicted results is presented in Table 82.VI.

We believe that the major mechanism for yield degradation in the pseudo-3D model is the thermal transport of energy away from the area of the fuel that is heated earliest in the implosion. As in the 1-D simulation, the fuel temperature increases significantly as the first and second shock waves converge on the origin, but with the 3-D simulation, this occurs at different times for different fuel wedges. As soon as the strongly driven regions of the capsule heat up, they transfer their thermal energy to cooler neighboring zones. Not only does this reduce the yield of the hotter zones, but it also reduces the potential yield of the cooler zones by increasing their adiabat and making an efficient implosion more difficult to achieve. The higher-convergence capsules ( $C_R \sim 20$ ) had the higher 1-D temperature predictions ( $T_i = 1650$  eV) but also experienced a greater reduction in core temperature due to 3-D effects (<70% of 1-D temperature), which is clearly reflected in the degraded yield predictions (YOC = 17%).

The preliminary experimental data of Fig. 82.56(b) seem to exhibit a more rapid falloff with convergence ratio than the *BUTTERCUP* calculations, although a larger data set is needed

to quantify this. It appears that *BUTTERCUP* can explain only some of the YOC reduction at higher  $C_R$ . The comparison suggests that, even with the best drive uniformity, hohlraum capsules are still susceptible to asymmetric shock convergence and other 3-D effects like Rayleigh–Taylor instabilities associated with physical defects caused during target manufacturing. Future experiments will hopefully help to identify the relative importance of irradiation nonuniformity and hydrodynamic instabilities.

**X-Ray Postprocessor**

One of the traditional ways<sup>11,44,51–53</sup> to assess hohlraum drive uniformity is simply to implode a capsule and look at the shape of the core: round indicates good uniformity and elliptical (in a cylindrical hohlraum) or triangular (in a tetrahedral

hohlraum) indicates poor uniformity. Experimentally, this can be done with a time-resolved x-ray-framing camera or with a time-integrated pinhole camera at high magnification. A pinhole camera with filtering chosen to absorb soft x rays automatically selects the bang-time image since the x-ray film detects mainly the high-intensity emission from the hottest part of the capsule. Since the fuel is usually so much hotter than the surrounding plastic shell, the actual shape of the fuel core tends to be well highlighted. In some instances, to improve the x-ray imaging, a small amount of high-Z gas such as argon or neon is added to the fuel, emitting higher-energy x rays at the same temperature. A thin film of beryllium is typically used as a filter on either camera to block out the low-energy radiation ( $\approx 2$  keV) coming from the pusher region.

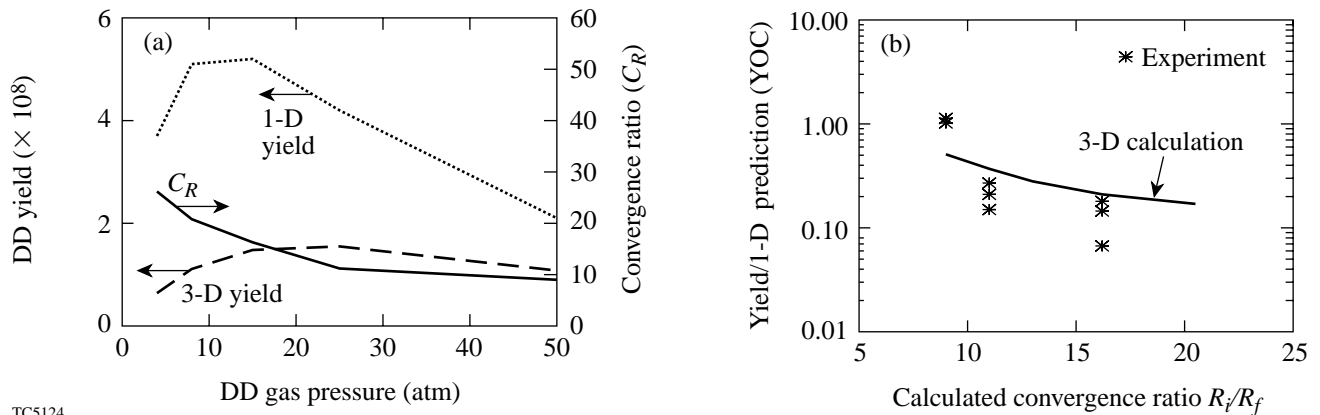


Figure 82.56 (a) Predicted 1-D and pseudo-3D yields and convergence ratio as a function of DD fuel pressure; (b) 3-D yield degradation (solid line) as a function of calculated convergence ratio, along with experimental measurements of these yields.<sup>49</sup> The theoretical yield degradation accounts only for effects caused by drive nonuniformity and not hydrodynamic instabilities. The experimental YOC values were based on experimental yields and 1-D *BUTTERCUP* predictions.

Table 82.VI: Summary of *BUTTERCUP* 1-D and 3-D predictions for the convergence ratio ( $C_R$ ), neutron yield ( $Y$ ), peak temperature ( $T$ ), peak areal density ( $\rho R$ ), core distortion ( $a/b$ ), and yield-over-clean (YOC) ratio for capsule implosions driven by a PS22 laser pulse. Predictions of  $C_R$  and peak  $\rho R$  are similar for 1-D or 3-D calculations.

DD fill (atm)	$C_R$	$Y$ (3-D) ( $10^8$ )	$Y$ (1-D) ( $10^8$ )	Peak $T$ (3-D) (eV)	Peak $T$ (1-D) (eV)	Peak $\rho R$ (mg/cm <sup>2</sup> )	$a/b$	YOC (theory)
4	20.5	0.64	3.7	1125	1650	5.8	1.20	17%
8	16.2	1.1	5.1	1150	1525	7.1	1.14	21%
15	13.0	1.5	5.2	1075	1350	8.7	1.12	28%
25	11.0	1.6	4.2	1000	1175	10.0	1.11	37%
50	9.0	1.1	2.1	825	900	12.6	1.06	51%

*BUTTERCUP* creates an image of the imploded core by analyzing the results of its hydrodynamic calculation with a 3-D radiation postprocessor. The first step is to reconstruct the entire capsule by copying and rotating the single pentagonal wedge modeled by *BUTTERCUP* 11 times, piecing together the 12 sections of a dodecahedron. This produces a complete three-dimensional model of the capsule, which is then rotated to give the correct orientation with respect to the x-ray camera. The complicated 3-D Lagrangian mesh can be projected onto a 2-D image by ray-tracing a grid of parallel lines through the 3-D capsule. Along the path of each ray, *BUTTERCUP* solves the multigroup radiation-transport equation,<sup>39</sup> which is similar to Eq. (10), except now with an additional source term  $I_{vp}$ , the blackbody intensity (erg/s/cm<sup>2</sup>/unit frequency):

$$\frac{dI_v}{ds} = \kappa'_v(I_{vp} - I_v). \quad (16)$$

Figure 82.57 shows a schematic of this procedure, including the Be filter and the x-ray film. The complicated 3-D mesh portrayed in this figure was constructed by connecting the centers of all adjacent Lagrangian zones, where each individual zone has the shape of a triangular prism. Upon exiting the capsule, each ray on the 2-D grid will have its own x-ray intensity spectrum over the range of relevant frequency groups. This spectrum is in turn filtered by the beryllium (using cold

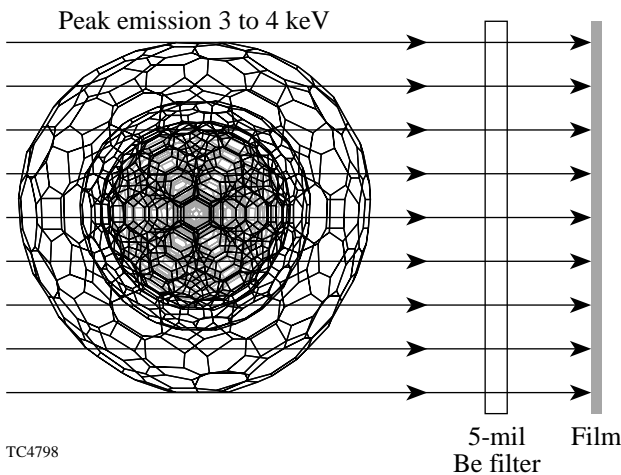


Figure 82.57 Algorithm for simulating experimental x-ray images. A multigroup x-ray postprocessor solves the radiation transport equation along rays traced through the 3-D Lagrangian grid of the capsule. A 5-mil (127- $\mu$ m) beryllium filter is used to remove low-energy signals coming from the colder plastic shell, giving a view of only the hot central fuel region.

opacities at solid density) and then integrated to give a single intensity point on the x-ray film. The resulting postprocessed image can then be directly compared with experimental data, either time averaged or time resolved.

Figure 82.58 shows the simulated x-ray image of a standard PS22 implosion at bang time. Qualitatively this image is very similar to the experimental image of Fig. 82.46(b): both appear round to within experimental error. It should be noted that the formation of this projected image provides an apparent smoothing of the actual 3-D distortion. For this image the calculated “ $a/b$  ratio,” defined as the maximum-to-minimum ratio of the radii of the 50%-intensity contour, is 1.02, while the  $a/b$  ratio of the fuel–pusher interface is 1.06. The reduction from 1.06 to 1.02 could be caused by geometric projection effects or by the nonuniform temperature distribution within the fuel, with the “corners” of the tetrahedral-shaped core being colder and thus not emitting as strongly.

**Conclusions**

Tetrahedral hohlraums have been proposed as an alternative approach to ignition in indirect-drive ICF. Recent experiments on the OMEGA laser have confirmed the predicted radiation drive uniformity ( $\sigma_{rms} < 1\%$ ) incident on an imploding capsule. To further understand these implosions, the view-factor code *BUTTERCUP* has been expanded to include a 3-D, time-

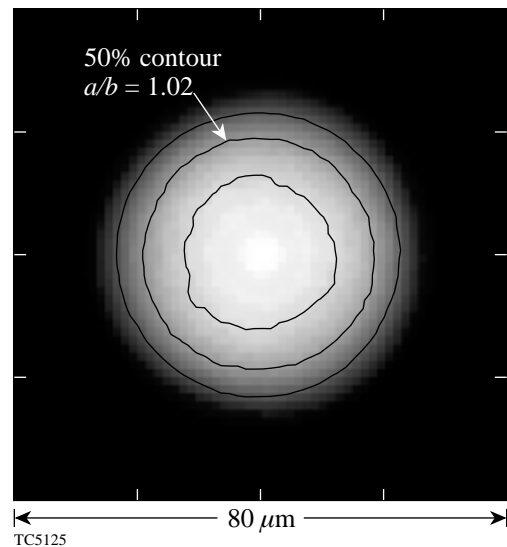


Figure 82.58 A postprocessed simulation of the x-ray image of the imploded core corresponding to Fig. 82.46(b), integrated over a 200-ps window around bang time. The  $a/b$  ratio of major to minor axes (1.02) is measured from the 50% contour of absolute x-ray intensity.

dependent treatment of the radiation diffusion into the gold wall and the radiation transport in the hohlraum. *BUTTERCUP* models the hydrodynamic implosion of the capsule by dividing it into many triangular wedges of equal solid angle, each undergoing a 1-D implosion driven by a different incident radiation source. These individual calculations are coupled together with 3-D thermal and radiation diffusion. Finally, an x-ray postprocessor is used to simulate an image of the imploded core.

The wall-diffusion model predicts a time-dependent radiation-drive temperature that agrees closely with experimental measurements from Dante. Additionally, *BUTTERCUP* is able to calculate a time-dependent albedo, which in turn can be used in a simple energy-balance equation to estimate radiation-drive temperatures. The hydrodynamic implosion calculations have provided valuable insight into the physics of indirect-drive ICF capsule implosions. Given the simplicity of the implosion model, predicted bang times as well as nuclear fusion yields are in reasonable agreement with those seen in the experiments. Pseudo-3D calculations suggest that for high-convergence implosions, one potential cause of yield degradation is the asymmetric shock convergence since the fuel is not heated as efficiently as in a perfectly spherical implosion. The 3-D x-ray postprocessor has shown that experimental images of the imploded capsule underestimate the actual level of core distortion.

These results show that, despite its relative simplicity, *BUTTERCUP* has already provided some critical new understanding of the connection between theory and experiment in hohlraum implosions. Finally, the pseudo-3D methods described here will likely be useful for developing and testing the more-sophisticated, fully three-dimensional codes that are needed to provide detailed modeling of ignition hohlraums on the NIF.

#### ACKNOWLEDGMENT

The authors gratefully acknowledge many valuable discussions with Dr. S. M. Pollaine and Dr. J. M. Wallace and with the many scientists who have come to LLE to participate in tetrahedral hohlraum experiments. Dr. N. D. Delamater is also thanked for providing the experimental images of Fig. 82.46. This work was supported by the U.S. Department of Energy Office of Inertial Confinement Fusion under Cooperative Agreement No. DE-FC03-92SF19460, the University of Rochester, and New York State Energy Research and Development Authority. The support of DOE does not constitute an endorsement by DOE of the views expressed in this article.

#### REFERENCES

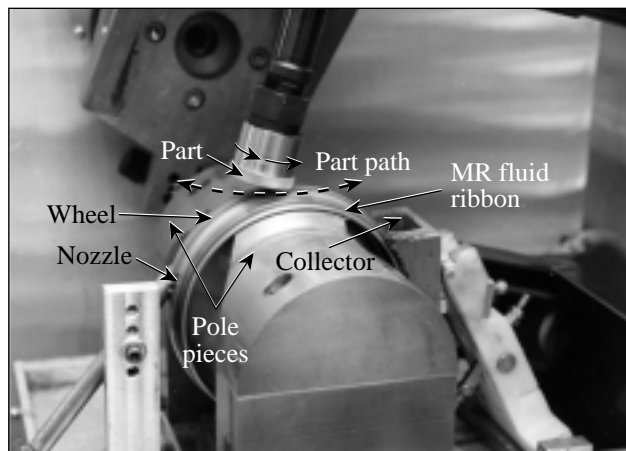
1. J. Nuckolls *et al.*, *Nature* **239**, 139 (1972).
2. J. D. Lindl, *Phys. Plasmas* **2**, 3933 (1995).
3. S. E. Bodner, *Comments Plasma Phys. Control. Fusion* **16**, 351 (1995).
4. S. W. Haan *et al.*, *Phys. Plasmas* **2**, 2480 (1995).
5. M. M. Marinak *et al.*, *Phys. Plasmas* **3**, 2070 (1996).
6. T. R. Dittrich *et al.*, *Phys. Plasmas* **5**, 3708 (1998).
7. K. A. Brueckner and S. Jorna, *Rev. Mod. Phys.* **46**, 325 (1974).
8. D. W. Phillion and S. M. Pollaine, *Phys. Plasma* **1**, 2963 (1994).
9. J. D. Schnittman and R. S. Craxton, *Phys. Plasmas* **3**, 3786 (1996). See also *Laboratory for Laser Energetics LLE Review* **68**, 163, NTIS document No. DOE/SF/19460-139 (1996). Copies may be obtained from the National Technical Information Service, Springfield, VA 22161.
10. T. R. Boehly, D. L. Brown, R. S. Craxton, R. L. Keck, J. P. Knauer, J. H. Kelly, T. J. Kessler, S. A. Kumpan, S. J. Loucks, S. A. Letzring, F. J. Marshall, R. L. McCrory, S. F. B. Morse, W. Seka, J. M. Soures, and C. P. Verdon, *Opt. Commun.* **133**, 495 (1997).
11. J. M. Wallace, T. J. Murphy, N. D. Delamater, K. A. Klare, J. A. Oertel, G. R. Magelssen, E. L. Lindman, A. A. Hauer, P. Gobby, J. D. Schnittman, R. S. Craxton, W. Seka, R. Kremens, D. K. Bradley, S. M. Pollaine, R. E. Turner, O. L. Landen, D. Drake, and J. J. MacFarlane, *Phys. Rev. Lett.* **82**, 3807 (1999).
12. H. Honda *et al.*, *Plasma Phys. Control. Fusion* **40**, 1097 (1998).
13. S. M. Pollaine and D. Eimerl, *Nucl. Fusion* **38**, 1523 (1998).
14. J. A. Harte *et al.*, *ICF Quarterly Report: Special Issue: Computational Advances in ICF*, **6**, 150, Lawrence Livermore National Laboratory, Livermore, CA, UCRL-LR-105821-96-4 (1996).
15. R. L. Kauffman *et al.*, *Phys. Rev. Lett.* **73**, 2320 (1994).
16. M. D. Rosen, *Phys. Plasmas* **3**, 1803 (1996).
17. S. H. Glenzer *et al.*, *Phys. Rev. Lett.* **80**, 2845 (1998).
18. L. J. Suter *et al.*, *Phys. Plasmas* **3**, 2057 (1996).
19. T. Mochizuki, S. Sakabe, and C. Yamanaka, *Jpn. J. Appl. Phys., Part 2*, **22**, L124 (1983).
20. A. Caruso and C. Strangio, *Jpn. J. Appl. Phys., Part 1*, **30**, 1095 (1991).
21. M. Murakami and J. Meyer-ter-Vehn, *Nucl. Fusion* **31**, 1333 (1991).
22. M. Murakami, *Nucl. Fusion* **32**, 1715 (1992).

23. K. H. Kang *et al.*, Nucl. Fusion **33**, 17 (1993).
24. P. Amendt *et al.*, Phys. Rev. Lett. **77**, 3815 (1996).
25. P. Amendt, T. J. Murphy, and S. P. Hatchett, Phys. Plasmas **3**, 4166 (1996).
26. The significant contributions of K. A. Klare and D. Drake to the design are acknowledged.
27. G. D. Tsakiris, Phys. Fluids B **4**, 992 (1992).
28. C. Stöckl and G. D. Tsakiris, Phys. Rev. Lett. **70**, 943 (1993).
29. See National Technical Information Service Document No. DE96000344 [M. D. Rosen, Lawrence Livermore National Laboratory, Livermore, CA, UCRL-JC-121585 (1995)]. Copies may be obtained from the National Technical Information Service, Springfield, VA 22161.
30. M. D. Rosen, Phys. Plasmas **6**, 1690 (1999).
31. R. E. Marshak, Phys. Fluids **1**, 24 (1958).
32. R. Sigel *et al.*, Phys. Fluids B **2**, 199 (1990).
33. H. N. Kornblum, R. L. Kauffman, and J. A. Smith, Rev. Sci. Instrum. **57**, 2179 (1986).
34. C. Decker, R. E. Turner, O. L. Landen, L. J. Suter, H. N. Kornblum, B. A. Hammel, T. J. Murphy, J. Wallace, N. D. Delamater, P. Gobby, A. A. Hauer, G. R. Magelssen, J. A. Oertel, J. Knauer, F. J. Marshall, D. Bradley, W. Seka, and J. M. Soures, Phys. Rev. Lett. **79**, 1491 (1997).
35. R. S. Craxton, J. D. Schnittman, and S. M. Pollaine, Bull. Am. Phys. Soc. **41**, 1421 (1996).
36. See National Technical Information Service Document No. LA-6760-M/XAB [W. F. Huebner *et al.*, Los Alamos National Laboratory, Report LA-6760-M (1977)]. Copies may be obtained from the National Technical Information Service, Springfield, VA 22161.
37. R. L. Bowers and J. R. Wilson, *Numerical Modeling in Applied Physics and Astrophysics* (Jones and Bartlett, Boston, 1991).
38. See National Technical Information Service Document No. LA-7130/XAB [B. I. Bennett *et al.*, Los Alamos National Laboratory, Report LA-7130 (1978)]. Copies may be obtained from the National Technical Information Service, Springfield, VA 22161.
39. Ya. B. Zel'dovich and Yu. P. Raizer, in *Physics of Shock Waves and High-Temperature Hydrodynamic Phenomena*, edited by W. D. Hayes and R. F. Probstein (Academic Press, New York, 1966).
40. T. R. Dittrich *et al.*, Phys. Plasmas **6**, 2164 (1999).
41. L. M. Hively, Nucl. Fusion **17**, 873 (1977).
42. B. N. Kozlov, At. Energ. **12**, 247 (1962).
43. M. D. Cable *et al.*, Phys. Rev. Lett. **73**, 2316 (1994).
44. T. J. Murphy, J. M. Wallace, N. D. Delamater, C. W. Barnes, P. Gobby, A. A. Hauer, E. L. Lindman, G. Magelssen, J. B. Moore, J. A. Oertel, R. Watt, O. L. Landen, P. Amendt, M. Cable, C. Decker, B. A. Hammel, J. A. Koch, L. J. Suter, R. E. Turner, R. J. Wallace, F. J. Marshall, D. Bradley, R. S. Craxton, R. Keck, J. P. Knauer, R. Kremens, and J. D. Schnittman, Phys. Plasmas **5**, 1960 (1998).
45. J. M. Wallace, K. A. Klare, T. J. Murphy, N. D. Delamater, E. L. Lindman, G. R. Magelssen, A. A. Hauer, S. M. Pollaine, R. E. Turner, R. S. Craxton, and J. D. Schnittman, Bull. Am. Phys. Soc. **42**, 2009 (1997).
46. R. L. McCrory, R. L. Morse, and K. A. Taggart, Nucl. Sci. Eng. **64**, 163 (1977).
47. G. B. Arfken, *Mathematical Methods for Physicists*, 3rd ed. (Academic Press, Orlando, 1985), p. 450.
48. J. M. Wallace, G. R. Bennett, T. J. Murphy, J. A. Oertel, P. Gobby, A. A. Hauer, W. S. Varnum, D. C. Wilson, R. S. Craxton, J. D. Schnittman, and S. M. Pollaine, Bull. Am. Phys. Soc. **43**, 1737 (1998); J. D. Schnittman, R. S. Craxton, S. M. Pollaine, R. E. Turner, T. J. Murphy, N. D. Delamater, J. A. Oertel, A. A. Hauer, and K. A. Klare, Bull. Am. Phys. Soc. **43**, 1737 (1998).
49. G. R. Bennett, J. M. Wallace, T. J. Murphy, A. A. Hauer, J. A. Oertel, D. C. Wilson, P. L. Gobby, N. D. Delamater, R. E. Chrien, R. S. Craxton, and J. D. Schnittman, Bull. Am. Phys. Soc. **43**, 1737 (1998).
50. P. Amendt, R. E. Turner, O. Landen, S. G. Glendinning, D. Kalantar, M. Cable, J. Colvin, C. Decker, L. Suter, R. Wallace, D. Bradley, S. Morse, G. Pien, W. Seka, and J. M. Soures, Bull. Am. Phys. Soc. **43**, 1739 (1998).
51. A. Hauer *et al.*, Rev. Sci. Instrum. **66**, 672 (1995).
52. A. A. Hauer *et al.*, Phys. Plasmas **2**, 2488 (1995).
53. T. J. Murphy, J. M. Wallace, N. D. Delamater, C. W. Barnes, P. Gobby, A. A. Hauer, E. Lindman, G. Magelssen, J. B. Moore, J. A. Oertel, R. Watt, O. L. Landen, P. Amendt, M. Cable, C. Decker, B. A. Hammel, J. A. Koch, L. J. Suter, R. E. Turner, R. J. Wallace, F. J. Marshall, D. Bradley, R. S. Craxton, R. Keck, J. P. Knauer, R. Kremens, and J. D. Schnittman, Phys. Rev. Lett. **81**, 108 (1998).

# Nanoindentation Hardness of Particles Used in Magnetorheological Finishing (MRF)

## Introduction

Classical finishing processes of optics employ precisely shaped, viscoelastic pitch or polyurethane foam-faced tools to transfer pressure and velocity through an abrasive slurry to the workpiece. Material is removed by chemical and mechanical interactions among the abrasive (typically micron- to submicron-size cerium oxide or aluminum oxide), the carrier fluid (water), and the workpiece. Magnetorheological finishing (MRF)—a new method of polishing optics—is being studied at the Center for Optics Manufacturing (COM) at the University of Rochester. This method utilizes a suspension consisting of magnetic particles [typically carbonyl iron (CI)], nonmagnetic abrasive particles, water, and stabilizing agents. Figure 82.59 shows an MR polishing machine. Rotation of the bottom wheel takes the fluid from the delivery nozzle and drives it underneath the part, where there is a strong magnetic field. Under the influence of the magnetic field, the fluid behaves like a “plastic” fluid; it is the shear stress caused by the hydrodynamic flow between the part and the rotating wheel that removes the material.<sup>1</sup>



G4973

Figure 82.59

Photograph of the MRF polishing process. The fluid emerges from the nozzle on the left and is carried to the right into the polishing zone under the part surface by the rotation of the wheel. The pole pieces are part of the electromagnet that provides the magnetic field that stiffens the fluid into a ribbon.

Figure 82.60 shows an example of microroughness on the surface of an initially pitch-polished fused-silica part processed without part rotation and with a nonaqueous MR fluid. With all chemistry eliminated, what remains are parallel grooves approximately 16-nm peak-to-valley and 1-nm rms,<sup>2</sup> caused by microscratching along the direction of flow. The water in aqueous MR fluids “turns on” chemistry, and removal rates increase substantially. Removal rates increase further in aqueous-based MR fluids containing nonmagnetic polishing abrasives (e.g.,  $\text{Al}_2\text{O}_3$ ,  $\text{CeO}_2$ , and nanodiamonds).<sup>3</sup> The features of the grooves look similar to the ones shown in Fig. 82.60. It is not known whether it is the abrasive action of the magnetic or nonmagnetic particles, or a chemical contribution from water and the presence of the nonmagnetic particles that plays the most important role in enhancing removal. Nanohardness tests described here allow us to begin to understand more fully the role of the various magnetic and nonmagnetic abrasives in the removal process.

Many authors (see Ref. 4 for example) describe a hydrated layer at the glass surface caused by the chemistry of the aqueous slurry. This soft hydrated layer affects polishing since it is easier to remove than the bulk material. An abrasive that is softer than the bulk material could conceivably remove material from a hydrated layer, but a harder particle (under the same load) could penetrate farther into the layer and thus remove more material. Kaller<sup>5</sup> discusses both the importance of finding the unknown hardness of abrasive particles and how the abrasive should actually be softer than the material being polished. An interesting experiment would be to compare removal characteristics of particles of different hardness in the same chemical environments. The variation in groove depth as a function of particle hardness would estimate the extent of the hydrated layer. For this experiment to be of the greatest utility the actual hardness of the particle must be known. The work described above is in progress.<sup>6</sup> To support this work, particle-nanohardness measurements are reported here and compared to some materials important to optics.

The hardness of a material is typically measured by pushing a hard material into a softer one and measuring the area of residual deformation left on the softer material. The hardness is the indenting load divided by the area of the residual deformation. In the past, Steinitz<sup>7</sup> determined particle microhardness through microindentation (material hardness found through microindentation will be referred to as microhardness, and that found through nanoindentation will be referred to as nanohardness). His figures show that the particle areas being indented were of the order of  $100\ \mu\text{m}$  in size and that the size of an indent was about  $20\ \mu\text{m}$ . Loads from 25 to 300 g (about 0.25 to 3 N) were used. The author points out that relatively large loads were needed for these indents so that the diagonals could be accurately measured for the microhardness calculation. This limited Steinitz to relatively large particles. The particles that we are concerned with have a median diameter of about  $5\ \mu\text{m}$ , although it is possible to screen out  $\approx 20\text{-}\mu\text{m}$  particles for study. The indent should therefore be significantly smaller than  $20\ \mu\text{m}$  for reasons that will be discussed later. These particles are still too small to be tested with a traditional microhardness tester. Small particles could be sintered or pressed together for ease of indentation, but heating or stressing the particles could change their mechanical properties.<sup>7</sup> Using the nanoindentation techniques described below, we are able to make smaller indents on much smaller particles than was done previously with microindentation, without altering the mechanical properties of the particles.

**Nanoindenter**

Hardness is measured with a commercially available nanoindenter.<sup>8</sup> The indenter is a Berkovich three-sided, pyramidal

diamond that accommodates maximum loads up to about 700 mN. Our experiments used maximum loads of 1 and 5 mN. This instrument applies a load by magnetic coil; the displacement of the indenter is continuously measured with a capacitance gauge. The displacement can be measured to within  $\pm 0.04\ \text{nm}$  and the output voltage from the loading operation to within  $4\ \mu\text{V}$ . The loads and displacements for our experiments are such that the measurement error is much less than 1%.

The nanoindenter's computer-automated system allows the user to choose the indentation experiment (loading rate, maximum load, drift correction, etc.) and location of the indent, leaving the instrument unattended as the experiment is performed. A typical experiment takes only about 15 min, but the time depends on the environment where the nanoindenter is located and the number of indents made. The first part of a test requires that the instrument settle to a user-specified critical drift rate. The indenter is kept in an insulated cabinet on a vibration isolation table. If the room containing the instrument has significant vibrations or temperature gradients, it may take some time for the drift rate to settle to the user-selected value. Our tests utilize the default critical drift rate of 0.05 nm/s.

Both nanohardness and the elastic modulus can be calculated via the load-displacement curves.<sup>9</sup> Since the load-displacement curve is of greatest interest, it is important that the particle be constrained from displacing due to the indenter loading from the top. That is, the measured displacement must be due to the motion of the indenter into the particle surface, and not due to the motion of the particle. For this reason,

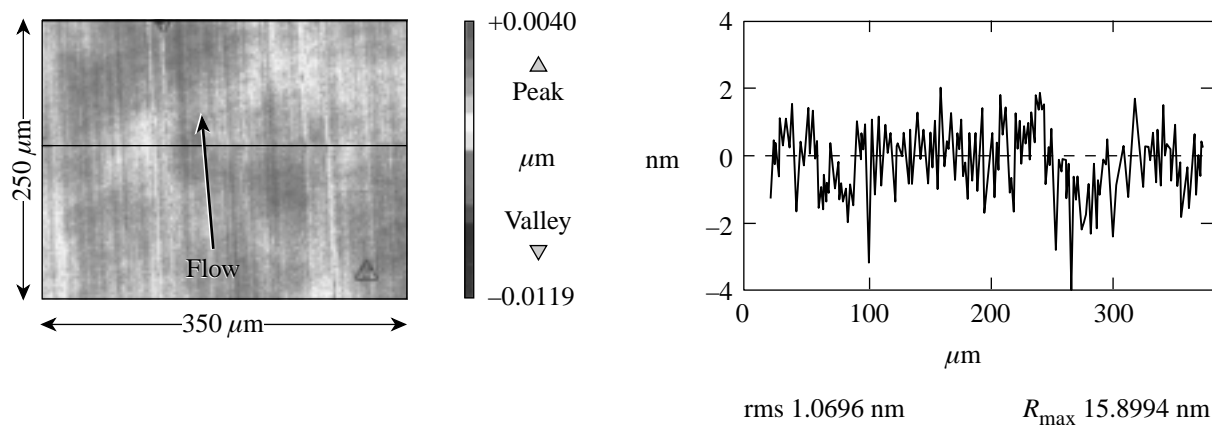


Figure 82.60 Microroughness on the surface of a fused-silica part after MRF without rotation. The MR fluid contains CI and nanodiamonds in a nonaqueous carrier fluid. The grooves are parallel to flow and are a result of particle/glass interaction.

magnetic particles are fixed rigidly to a glass substrate by embedding them in an epoxy matrix, and nonmagnetic particles are cast in a polymer substrate (phenol-formaldehyde or Bakelite). There is evidence in the literature that the substrate affects the measured properties of thin films.<sup>10,11</sup> Initial screening experiments before this study suggested that this problem influenced small-particle indentation as well. Special sample preparation techniques described below were devised to avoid this effect.

One of the strengths of the nanoindenter is that it allows precise positioning of indents. This ability allows us to search for and indent individual particles. Indents can be positioned to within  $0.4\ \mu\text{m}$ , but this accuracy is reduced by thermal drift and the accumulation of small errors.<sup>8</sup> Frequent system calibration allows for the precision necessary to indent  $5\text{-}\mu\text{m}$  particles, but there are fewer failed tests (i.e., no particles indented) if the indented surface is approximately  $20\ \mu\text{m}$  in diameter. The larger particle size reduces the importance of any positioning error caused by the nanoindenter translation stages. For this reason, the particles are suspended in methanol and passed through a sieve<sup>12</sup> to separate out larger particles for testing. A second option, if the particles are relatively small, is to create an array of indents near a particle. For example, a line of indents can be defined so that, while some of the indents will be into the epoxy, the rest will be on the particle. Results reported here are from experiments performed by either method.

**Sample Preparation for Magnetic Particles**

The magnetic particles (primarily CI) are processed as illustrated in Fig. 82.61. After they are sieved, the particles are placed on a BK7<sup>13</sup> glass substrate, which is set on top of a rare earth permanent magnet.<sup>14</sup> The roughness of the substrate is about  $1\ \mu\text{m}$  rms or smoother, and the substrate is flat to within about  $1$  to  $10\ \mu\text{m}$  per  $\text{cm}^2$  of surface. These specifications are not critical, but height variations in the substrate surface of the order of tens of microns per centimeter are avoided. Next, a two-part, room-temperature curing epoxy<sup>15</sup> is spread onto a polymer foil,<sup>16</sup> and the foil is placed over the particles, epoxy side down. A microscope slide is placed on top of the back side of the polymer foil (the foil prevents the epoxy from adhering to the slide), and finally a mild iron weight (40 g) is placed over the slide [see Fig. 82.61(a)]. Since the iron weight is attracted to the magnet, the epoxy/particle matrix is forced into a thin layer, and the microscope slide helps to create a more uniform surface on the epoxy. Figure 82.61(b) shows how the epoxy is believed to surround the CI particles to hold them in position during curing.

This fabrication procedure accomplishes two things: First, the particles are attracted downward to the magnet. This pulls the bottom particle layer toward the BK7 surface. Second, when placed in a magnetic field, the magnetic particles tend to align into chain structures.<sup>17</sup> This helps prevent epoxy from getting in between adjacent particles. The perceived advantage is that by having chains of particles resting against the glass substrate, we minimize the possibility of measuring a reduced hardness due to effects of a compliant substrate mentioned above.<sup>10,11</sup> The assembly shown in Fig. 82.61(a) is left to cure in air for 24 h. Once the epoxy has cured, the mild iron weight and microscope slide are removed from the magnet. The polymer foil is stripped away, leaving the BK7 substrate and CI/epoxy matrix. The matrix surface is ground by hand on a serrated, cast iron lap with  $9\ \mu\text{m}$  alumina<sup>18</sup> to thin the film and create flat surfaces on the particles. Grinding is performed as described by Parks *et al.*<sup>19</sup> so that work hardening of the particles is minimized. A load of about 35 kPa (about 5 psi)<sup>20</sup> is used with the iron lap rotating at 35 rpm. This step takes no more than a few minutes. The grinding step always results in some wedge being put into the surface, leaving an epoxy/CI

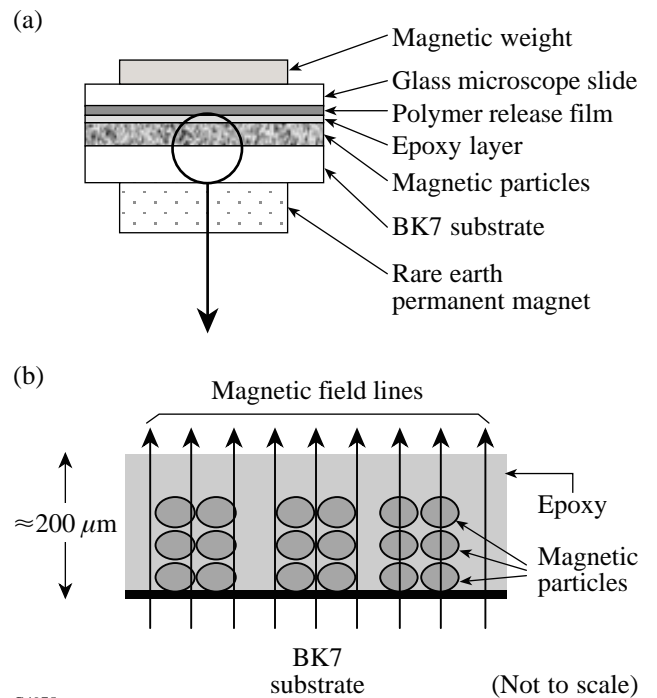


Figure 82.61 (a) Schematic diagram of the method used in sample preparation. The particles and epoxy are sandwiched between two hard, flat surfaces so that a thin layer is formed. (b) Sketch of how the particles are thought to orient in the epoxy layer shown in (a) under the influence of a magnetic field.

film that decreases in height from one side to the other (see Fig. 82.62). The grinding step is complete when the glass substrate starts to become visible. In this way, we know that there is a thin layer of the composite film where indents can be taken very near the glass substrate.

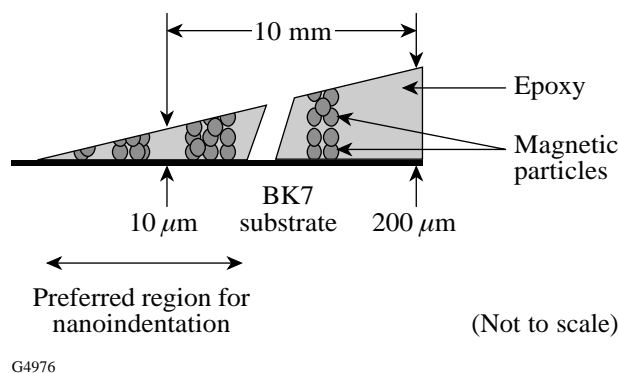


Figure 82.62

Schematic diagram of the sample after the magnet has been removed and the top layer of epoxy has been ground and polished away. The flats on the particles constitute the potential indent sites.

Samples are polished with light pressure on a cerium oxide impregnated felt lap<sup>21</sup> at a rotation speed of 50 rpm. This step is monitored with the help of an optical microscope.<sup>22</sup> The polishing phase is considered complete when few polishing grooves can be seen on the CI surfaces at 1000× magnification. This step is a manual operation that takes approximately 30 min, depending on the skill of the operator.

At the conclusion of sample preparation, the CI/epoxy film thickness varies from about 200 μm down to zero (at the glass surface) over a distance of about 10 mm as measured by mechanical profilometry.<sup>23</sup> Indents are placed where the film is about 25 to 50 μm thick. As shown schematically in Fig. 82.62, the goal of our sample preparation process is to create polished flats on the CI particles.

### Sample Preparation for Nonmagnetic Abrasive Particles

The above technique for sample preparation is appropriate only for magnetic particles since we take advantage of the magnetic attraction of the particles to try to minimize the effect of deformation of the embedding medium. The nonmagnetic particles are treated differently. They are mixed with Bakelite pellets in a ratio of about 1 to 5. This mixture is then put into a 1.25-in.-diam cylindrical mold, placed into a press,<sup>24</sup> heated to 150°C, and pressed under 5000-psi pressure. It is assumed that this heat and pressure do not change the particle properties.

The heat and pressure allow the Bakelite to form a network around the abrasives so that they are held in place during indentation experiments. The Bakelite sample is then ground and polished as described above until several particles are exposed. We have found that the Bakelite medium has a hardness and elastic modulus of about 0.4 GPa and 7 GPa, respectively. These values are significantly lower than those of the particles being tested, so deformation of the embedding medium is a concern (discussed below).

### Validation of Tests

It is important to have a way to verify that indentations are actually being placed on an individual particle. Figures 82.63(a) and 82.63(b) show SEM<sup>25</sup> images of a carbonyl iron particle surface after indentation testing. The programmed maximum load was 5 mN. The test was set up to put an initial indent in the center of the particle and follow it with four more indents spaced 2 μm apart. The five indents are clearly shown in Fig. 82.63(a). Figure 82.63(b) shows a close-up view of two of the indents. The sharpness and repeatability in size of the indents are apparent. Indenter tip radius is 20–80 nm<sup>8</sup>.

The sample thickness should be four to ten times larger than the depth of an indent.<sup>10</sup> Also, indents should be more than two times the size of any “stress deformation” that results from indentation. This prevents deformation due to neighboring indents from interacting.<sup>26</sup> Since most indents are approximately 200 nm deep, particles greater than 2 μm in size are sufficiently large for these loads. We choose relatively large particles and avoid the edges of particles so that we meet this criteria. The indents in Fig. 82.63 are for illustration only. Quantitative data are obtained mostly by placing a single indent on a single particle. It should be noted, however, that the nanohardness values obtained from the indents shown in Fig. 82.63 were consistent with nanohardness values obtained from other tests performed on the same particle type.

If the particles are particularly small, it might be advantageous to make arrays of indents. In this case, care must be taken to identify valid indents from invalid ones. Figure 82.64 shows the indenter load/displacement curves of three indents from a linear array (similar to Fig. 82.63) on a single CI particle. The maximum load was 5 mN for all three indents, but the vertical displacement of the indenter was about 220 nm for indent 1, about 300 nm for indent 2, and about 550 nm for indent 3. The projected area and calculated nanohardness varied accordingly. The nanohardness was 715 kgf/mm<sup>2</sup> (7.01 GPa) for indent 1, 370 kgf/mm<sup>2</sup> (3.63 GPa) for indent 2, and 86 kgf/mm<sup>2</sup> (0.84 GPa) for indent 3. This wide range in the

measured nanohardness indicates that there is some error in the measurement.

The reason for the variation in the nanohardness for this single particle is evident from the three load/displacement curves in Fig. 82.64. The first indent shows typical loading and unloading behavior<sup>9</sup> for a single, hard material, whereas the second and third indents show a clear slope change in the loading curve (circled in Fig. 82.64). It is believed that this slope change is due to epoxy contamination around the edge of the particle. For the second and third indents, as the load is applied, the indenter first encounters an epoxy film, and the shallow slope of the loading curve is due to the fact that the epoxy is much softer than the CI. The change in slope of the

loading curve can be explained by the fact that the thin material under load becomes more stiff (the slope of the curve increases) as the indenter is influenced by the underlying material. That is, we expect the slope of the loading curve to increase due to both elastic and permanent deformation as the indenter moves through the epoxy layer. Hay and Pharr<sup>11</sup> use a similar method to monitor the effects of a thin, hard film on a soft substrate. In their work, the slope of the loading curve becomes shallower as the soft substrate begins to flow under the hard film. As expected, the loading curve becomes steeper in our case since we have a thin film of soft material on a hard substrate. Such an interpretation is also consistent with a quantitative estimate of contact zone width based on the Sneddon solution of a rigid cone indenting an elastic half-space of a material with the properties of epoxy.<sup>27</sup> For these reasons indent 1 would be considered a successful indent, whereas indents 2 and 3 would not.

Krell *et al.*<sup>28</sup> discuss another consideration for indentation experiments. It is possible that a particle could be pushed into the embedding medium under the influence of the indenting load. By creating chains during sample preparation of magnetic particles and indenting particles near the BK7 surface, we minimize the chance of particle motion. The nonmagnetic particles are simply sitting in a relatively soft Bakelite matrix. It is conceivable that a small particle could be pushed into the matrix by the indenting load. To estimate this effect, consider

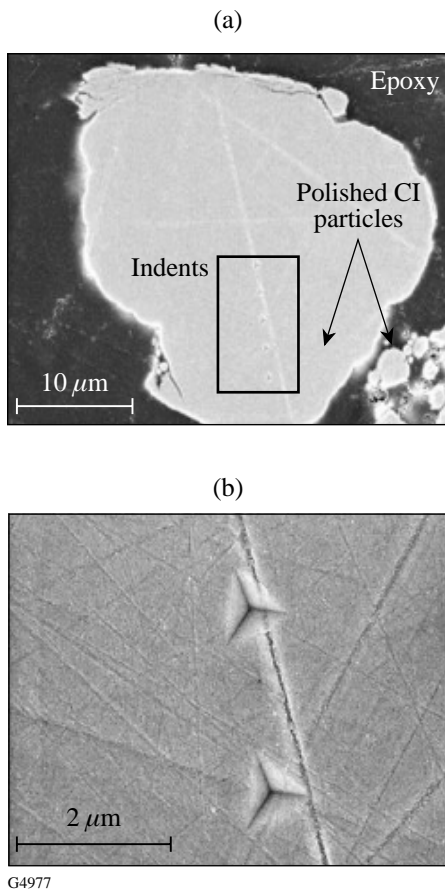


Figure 82.63  
SEM of a large CI particle after a set of five indentations at 5-mN maximum load. The initial indent was placed in the middle of the particle, and the five indents were spaced 2 μm apart. This demonstrates the ability of the nanoindenter to place multiple indents precisely on a 20- to 25-μm-diam particle. Photographs like these are very difficult to obtain because of the difficulty in locating the indentation site after moving the sample from the nanoindenter to the SEM.

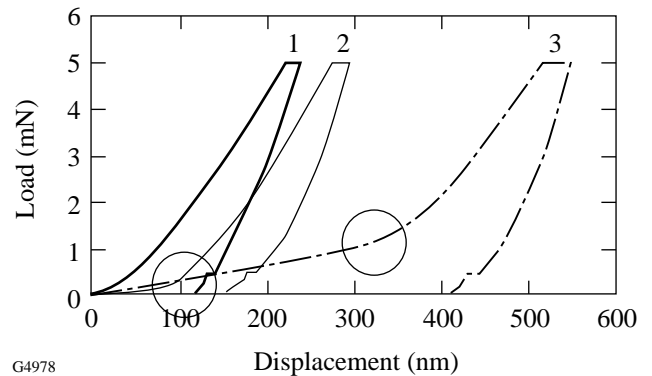


Figure 82.64  
Load/displacement curves of three indents placed in a linear array on a single particle. The continuous behavior of indent 1 suggests a legitimate particle indent, whereas the slope changes in indents 2 and 3 (shown circled) suggest that there may be a region on the edge of the particle contaminated by the epoxy. Indent 2 shows a small region at the beginning of the loading, suggesting a small soft layer between the indenter and the particle. Indent 3 has a much larger region with this shallow slope, suggesting a deeper soft layer. Indents with these distinct changes in slope are not used.

the particle shown in Fig. 82.63(a). The area of this particle is approximately  $30\ \mu\text{m} \times 30\ \mu\text{m}$  ( $900 \times 10^{-12}\ \text{m}^2$ ) and subject to a 5-mN load. The approximate stress underneath the particle is the force divided by the cross-sectional area or 5.6 MPa in this case. This is two orders of magnitude below the hardness of the Bakelite or epoxy matrix. As the particle size decreases, the applied stress approaches the hardness of the matrix material. For this reason, low indenting loads are used, and particles on the large end of the size distribution are tested.

Finally, a problem that may affect both magnetic and nonmagnetic particles is the indentation-size effect (ISE). Lambropoulos *et al.*<sup>29</sup> and Fang<sup>30</sup> discuss this phenomenon in microindentation tests where the microhardness is a function of the applied load (and therefore size) of the indent. More recently Sangwal *et al.*<sup>31</sup> used an atomic force microscope to study ISE in nanoindentation experiments. Specifically, they report that the nanohardness decreases with an increase in indentation size and that there is a large discrepancy between hardness due to nanoindentation and microindentation of MgO.

Dahmani *et al.*<sup>32</sup> show that the elastic modulus and nanohardness of fused silica measured with nanoindentation agree with published results (the nanohardness was compared with a Vickers microhardness test<sup>33</sup>). This means that the low loads used in nanoindentation are not an immediate cause of ISE. We have also performed experiments at both 1-mN maximum load and 5-mN maximum load. A different nanohardness measured at the two different loads would be a sign that either ISE is a problem and/or the particle was moving relative to the indenter. None of our experiments showed a difference at the two loads, so these effects are not considered significant for our experiments. Sangwal *et al.*<sup>31</sup> perform indents at a load of  $10\ \mu\text{N}$ , which is two orders of magnitude below the load that we use. Also, they mention that their indentations fully recover after a sufficiently long time. Our indents do not recover. The fact that we are able to take SEM scans of indents a week after indentation tests is evidence of permanent deformation of the material. It is believed that their low loads and evidence of complete indent recovery put them in a different experimental regime.

### Prior Work

Previously obtained hardness data for materials of interest to optics fabrication have typically been measured using either a Moh's test<sup>34</sup> or microindentation techniques on bulk or sintered samples. The Moh's scale is derived from a scratch test that uses ten minerals of increasing hardness. A substrate

material is assigned a number on the Moh's scale according to the hardest standard mineral for which there is a visible scratch during a simple abrasion operation.<sup>34</sup> This is a qualitative test, but it gives relative hardness values for different substrate materials against known standards. Microindentation is a more quantitative experimental technique that typically uses a four-sided, pyramidal indenter (usually a Knoop or Vickers diamond) to permanently deform a material under a known load (1 to 1000 gf). The hardness of a material is the applied load divided by a measure of the area of the indent.<sup>26</sup> The Vickers and Knoop microhardness numbers are similar in magnitude.<sup>35</sup> More recently, it has been suggested that the hardness of submicrometer particles may be estimated by associating the hardness to the density of the material.<sup>36</sup> This correlation is unknown and is complicated by internal porosity of the particles. Results reported here for CI show the hardness–density correlation to be invalid.

This is the first work that has utilized nanoindentation to determine the hardness of small abrasive particles. Dahmani *et al.*<sup>32</sup> show that the Berkovich indenter measures a nanohardness similar in value to that from a Vickers microindent. Therefore we validate our results using existing microhardness data from bulk materials to compare with nanohardness results. Moh's data is used for comparison where no microhardness data exist in the literature.

### 1. Hard and Soft CI

The magnetic particles of interest to us are the “hard” and “soft” carbonyl iron particles that are typically used to prepare aqueous suspensions of MRF. These powders are formed from the decomposition of liquid iron pentacarbonyl. This process is explained elsewhere.<sup>37–39</sup> The high microhardness of the hard CI particles is attributed to the presence of carbon, oxygen, and nitrogen<sup>37</sup> and/or high internal stress in the material,<sup>39</sup> but does not appear to be clearly understood. Pfeil<sup>37</sup> cites a Vickers microhardness (25-g load) of about  $850\ \text{kgf}/\text{mm}^2$  (8.33 GPa) for the hard carbonyl iron particles. Softening is achieved by annealing in a hydrogen environment to drive out the carbon, oxygen and nitrogen impurities. Boehm<sup>40</sup> discusses this annealing process and claims that, initially, the microhardness rises with heat treatment. Eventually it drops when the temperature is raised above  $500^\circ\text{C}$ . Boehm confirms Pfeil's result for the hard CI and gives a minimum microhardness of  $280\ \text{kgf}/\text{mm}^2$  (2.75 GPa) for the softer, reduced CI. Finally, Ebenhoeh<sup>38</sup> cites a Vickers microhardness of  $900\ \text{kgf}/\text{mm}^2$  (8.82 GPa) for the hard CI and  $100\ \text{kgf}/\text{mm}^2$  (1 GPa) for the soft CI at the same 25-g load. No details about the tests are given.

2. Nonmagnetic Abrasives

Six nonmagnetic particles have also been chosen for nanohardness tests since they are often used in grinding and polishing. Two types each of alumina and cerium oxide were chosen since they are of particular interest to optics fabrication. The two types of alumina differ in that one is used for grinding and one for polishing. The cerium oxide samples are both refined from a common ore, but with different heat treatments. We also tested silicon carbide and cubic zirconia particles, which were chosen because (1) they, too, are commonly used in optical fabrication and (2) the existing microhardness data in the literature helps to further verify our test results.

Microindentation hardness data for nonmagnetic abrasives exist in the literature. Krell *et al.*<sup>28</sup> test various alumina abrasives and discuss how the particle hardness and fracture toughness can affect the grinding efficiency. They also discuss the importance of knowing the hardness of individual abrasive particles as opposed to bulk values, especially in sintered specimens. Their experiments utilize 0.6-mm-mean-sized samples embedded in an epoxy matrix. They use Vickers indents at 10-N load. They also discuss the effect of the substrate and magnitude of the load on their measurements. Namely, if they use a higher load, the particles are pushed into the matrix. If they use a lower load, then they have difficulty measuring the size of the indent. We discussed the problems associated with using a high load, but we do not have their problem associated with low loads since our hardness is determined from the load/displacement curve. Our loads are four orders of magnitude less than theirs, which allow us to measure smaller particles in more-localized regions. Their results for different types of sintered alumina (at various

densities and compositions) show Vickers hardness values of about 15 to 20 GPa. They estimate the actual microhardness values for some of the samples to be as high as 25 GPa, but porosity effects are believed to give lower values. These data are included in Table 82.VII.

Several other references, summarized in Table 82.VII, give bulk microhardness data for materials of interest. Okuyama *et al.*,<sup>41</sup> Nathan,<sup>42</sup> and Brecker *et al.*<sup>43</sup> give hardness data for alumina (Al<sub>2</sub>O<sub>3</sub>) and silicon carbide (SiC). These references suggest a Moh's hardness of about 9, and an approximate Knoop microhardness of 20±3 GPa for alumina and 27±5 GPa for SiC. Nassau<sup>44</sup> gives the hardness of cubic zirconia between 8.0 and 8.5 on the Moh's scale. Since alumina and SiC have a Moh's hardness of about 9, we can expect cubic zirconia to have a Knoop microhardness similar to, but slightly less than that of Al<sub>2</sub>O<sub>3</sub> and SiC. There is, however, no direct relationship between the two hardness scales. No details about these microhardness measurements are given.

Some information on the hardness of cerium oxide is also available in the literature. Izumitani<sup>4</sup> states that cerium oxide has an approximate Moh's hardness of 6 and that most optical glasses range from 5 to 6 on the same hardness scale. Therefore we can expect the hardness of cerium oxide to be of the order of BK7 and FS glasses. While West<sup>45</sup> does not give a number for the hardness of cerium oxide, he does discuss how thermal treatments at elevated temperatures cause cerium oxide to become harder. Izumitani<sup>4</sup> also discusses the heat treatment of cerium oxide and confirms West's result. We will show a similar result with our experiments.

Table 82.VII: Summary of hardness data from the literature for various abrasive materials.

Abrasive	Mohs Hardness <sup>(Ref)</sup>	Knoop Hardness (Gpa)	Vickers Hardness (Gpa)
Alumina <sup>a,c</sup>	9 <sup>(41)</sup> , 9.4 <sup>(42)</sup>	16.58–24.22 <sup>(41,43)</sup>	–
Sintered alumina <sup>b</sup>	–	–	15–25 <sup>(28)</sup>
Zirconia <sup>c</sup>	8.0–8.5 <sup>(44)</sup>	–	–
Cerium oxide <sup>c</sup>	6 <sup>(4)</sup>	–	–
Silicon carbide <sup>a</sup>	9.6 <sup>(42)</sup>	22.15–31.63 <sup>(41,43)</sup>	–

<sup>a</sup>Microhardness tests of bulk material

<sup>b</sup>Microhardness tests of large particles

<sup>c</sup>Moh's tests not well defined

**Results**

Tables 82.VIII to 82.X show the results from our experiments. Table 82.VIII gives the 11 magnetic particles that were tested with the nanoindenter: ten are carbonyl iron and one is a carbonyl nickel. The types and vendor plus information on the composition and nanohardness of each particle are listed. Table 82.IX lists the nonmagnetic abrasives along with their vendor, crystal structure, and nanohardness information. We also indented two optical glasses (BK7<sup>13</sup> and fused silica, FS<sup>46</sup>), one laser glass (LHG8<sup>47</sup>), and a soft crystal (potassium dihydrogen phosphate, KDP<sup>48</sup>) under identical conditions for comparison. Information on these materials is given in Table 82.X.

Figure 82.65 shows the relative nanohardness values for the different particles compared to the reference glasses. First, consider the CI particles: the hard CI's are as hard (S-1701) or harder (EW, OS 3770, OS 1225, OS 2983, OM) than fused silica. The soft, reduced forms of the CI's are significantly softer than all of the glasses and comparable in hardness to KDP. Two of the OS samples (OS 5942 and OS 9560) have

intermediate nanohardness values due to a variation of processing parameters. Some of the nanohardness values measured for hard particles are harder than those cited in the literature, while others are in good agreement with the numbers cited. The soft CI's are much softer, as suggested by the literature. The nickel proved to be an extremely soft particle, in contradiction to our expectations from discussions with the manufacturer.

The differences in nanohardness among the hard CI samples can be analyzed further. The heat treatment process and the presence of impurities play a significant role in determining hardness of the particles. The reduction process softens the particles by removing the impurities in the iron. Conversely, it has been shown that the inclusion of some of these impurities often hardens iron (see, for example, Refs. 58 and 59). It is not known if the impurities are present in atomic or molecular form. It would be expected that impurities strengthen a metal as the square root or cube root of the concentration whether in atomic or molecular form.<sup>60</sup> Specifically, it is expected that the hardness of iron will increase as the square

Table 82.VIII: Summary of the manufacturer information and nanohardness results for the indented magnetic particles, given in rank order from hardest to softest.

ID	Material	Lot Number <sup>Mfr.</sup>	<i>b</i> <sub>wt%</sub>			Hardness by Nanoindentation (standard deviation) (Gpa)	
			Nitrogen	Carbon	Oxygen		
OS 1225	Carbonyl iron	1225 <sup>(49)</sup>	[0.540	0.880	0.580] <sup>(52)</sup>	14.4	(0.8)
OS 2983	Carbonyl iron	2983 <sup>(49)</sup>	[0.750	0.800	0.590] <sup>(52)</sup>	13.1	(0.6)
OM	Carbonyl iron	3999 <sup>(49)</sup>	0.800	0.790	0.240	12.4	(1.0)
EW	Carbonyl iron	9970 <sup>(49)</sup>	1.000	0.800	0.500	11.7	(0.8)
OS 3770	Carbonyl iron	3770 <sup>(49)</sup>	[0.180	1.120	0.650] <sup>(52)</sup>	10.5	(1.0)
S-1701	Carbonyl iron	6070111 <sup>(50)</sup>	0.850	0.850	0.730	9.7	(0.5)
OS 5942	Carbonyl iron	5942 <sup>(49)</sup>	0.060	1.170	0.320	7.3	(1.0)
OS 9560	Carbonyl iron	9560 <sup>(49)</sup>	1.180	0.970	0.200	4.9	(1.0)
CM	<sup>a</sup> Carbonyl iron	7829 <sup>(49)</sup>	[<0.010	0.009	0.170] <sup>(52)</sup>	2.4	(0.5)
R-1521	<sup>a</sup> Carbonyl iron	8052131 <sup>(50)</sup>	0.024	0.033	0.240	2.2	(1.0)
Nickel	Carbonyl nickel	101397 <sup>(51)</sup>				1.7	(0.6)

<sup>a</sup>Reduced form of particle

<sup>b</sup>Amount of residual nitrogen, oxygen, and carbon in the carbonyl icons is in weight percent, usually per certificate of analysis from the manufacturer.

root or cube root of the concentration of carbon, nitrogen, and oxygen (in this order for the hardening effect).<sup>61</sup> Using the amounts of residual carbon and nitrogen provided by the vendor, nanohardness values are plotted as a function of the total amount of carbon and nitrogen in Fig. 82.66. The OS samples show a relatively large variation in nanohardness; therefore, data for all OS samples have been averaged into a single data point with error bars representing a standard deviation. After discussions with the company, we hypothesize that variations in their internal processing methods, such as annealing, were responsible for this variation in the nanohardness data. The data have been fit with a simple power law curve on a log-log scale, and the equation and correlation coefficient are shown with the plot. Notice that the data fit (correlation better than 0.94) a power law of about 0.38. While the variation due to the OS samples is somewhat large, this trend in the nanohardness as a function of impurity content is in the expected range.

The data for the polishing abrasives reveal some interesting features. The nanohardness values of the #30 grinding alumina, silicon carbide, cubic zirconia, and cerium oxide samples agree with microhardness and Moh's hardness values reported for bulk materials (compare Tables 82.VII and 82.IX), validating our results. The 1- $\mu\text{m}$  alumina has a significantly lower nanohardness than the grinding alumina—a surprising result that can be attributed to proprietary manufacturing methods.<sup>62</sup>

We report for the first time on nanohardness data for cerium oxide abrasives. The two cerium oxides, SRS 372 and SRS 373, differed only in their heat treatments. Specifically, SRS 372 had a higher thermal treatment than did SRS 373.<sup>63</sup> This resulted in SRS 372 having about a 50% higher nanohardness than SRS 373, which agrees with descriptions of heat-treated cerium oxide given by Izumitani<sup>4</sup> and West.<sup>45</sup>

Table 82.IX: Summary of the manufacturer information and nanohardness results for the indented nonmagnetic abrasives, given in rank order from hardest to softest.

ID	Material	Lot Number <sup>Mfr.</sup>	Crystal Structure	Hardness by Nanoindentation (standard deviation) (Gpa)
SiC	Silicon carbide	<sup>a</sup> N/A <sup>(53)</sup>	Hexagonal	31.8 (8.0)
#30 Al <sub>2</sub> O <sub>3</sub>	Grinding alumina	C9043 <sup>(54)</sup>	Hexagonal	29.8 (7.0)
CZ	Cubic zirconia	1502792 <sup>(55)</sup>	Cubic	24.1 (5.0)
1 $\mu\text{m}$ Al <sub>2</sub> O <sub>3</sub>	Polishing alumina	C602 <sup>(56)</sup>	Not reported	10.0 (4.0)
SRS 372 <sup>b</sup>	Cerium oxide	SDH-13-1 <sup>(57)</sup>	Not reported	7.5 (2.0)
SRS 373 <sup>c</sup>	Cerium oxide	SDH-13-2 <sup>(57)</sup>	Not reported	5.0 (1.3)

<sup>a</sup>Lot number is not available. Abrasives were received in 8/94.

<sup>b</sup>High thermal treatment

<sup>c</sup>Low thermal treatment

Table 82.X: Summary of the manufacturer information and nanohardness results for the indented bulk optical materials given in rank order from hardest to softest.

ID	Lot Number <sup>Mfr.</sup>	Hardness by Nanoindentation (standard deviation) (Gpa)
FS	7940 <sup>(46)</sup>	9.8 (0.1)
BK7	N/A <sup>(13)</sup>	7.7 (0.1)
LHG8	N/A <sup>(47)</sup>	5.3 (0.1)
KDP	N/A <sup>(48)</sup>	1.5 (0.4)

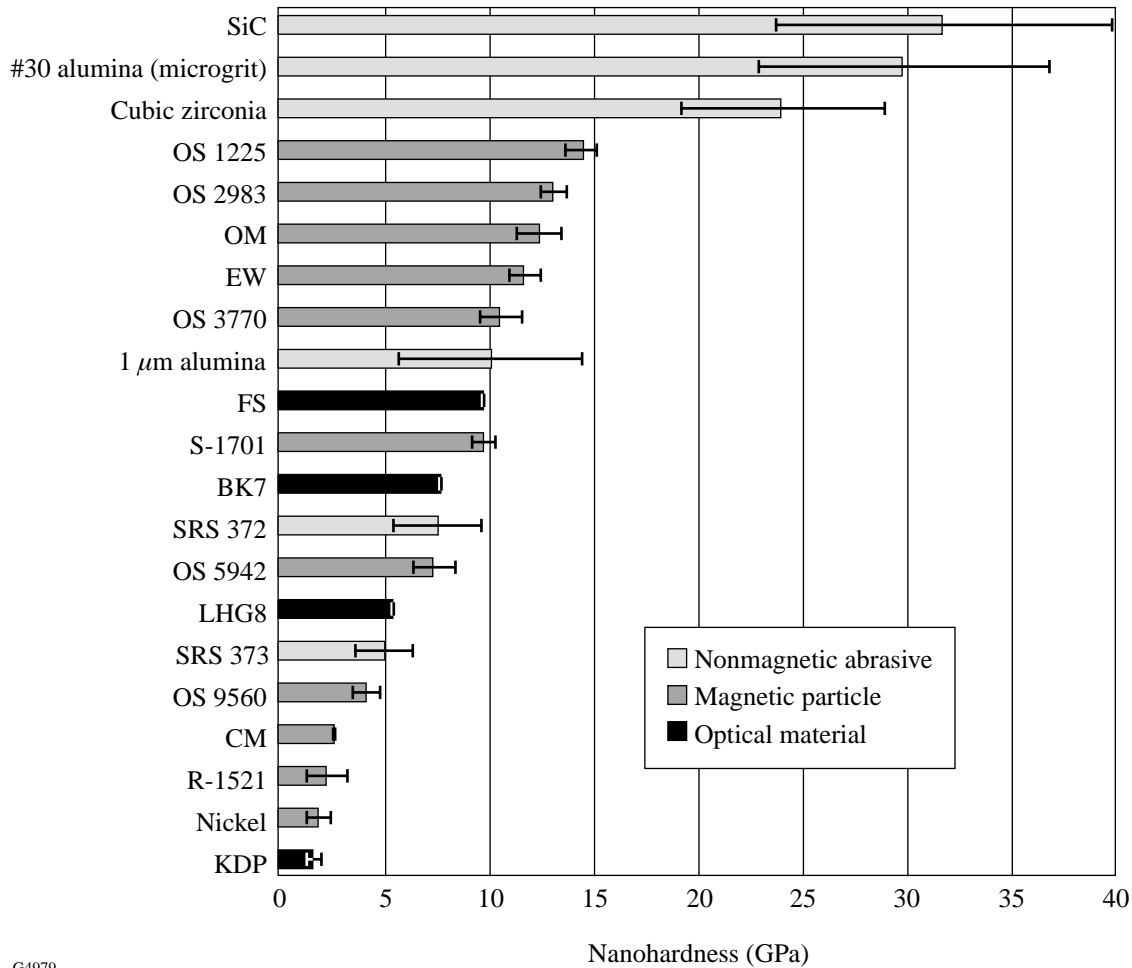
The error bars for the magnetic abrasives and optical materials are considerably smaller than those of the polishing abrasives. This is attributed to the more uniform structure of CI and the optical materials versus the multiphase nature and heterogeneity of the polishing abrasives tested. Krell *et al.*<sup>28</sup> also had relatively large errors in their measurements, which they attributed to microstructure. We do not have control of the crystal orientation of the abrasives that we are indenting, which will also affect the measured nanohardness.

**Summary**

A technique for nanoindentation of small, magnetic and nonmagnetic abrasive particles has been described. Most results are consistent with what has been previously reported, but some results are new. While Krell *et al.*<sup>28</sup> show microhardness differences in various grinding aluminas, it is interesting to see

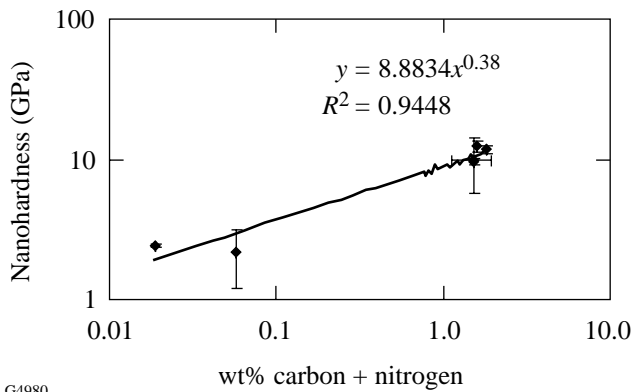
the large differences in nanohardness values of the actual commercial products used in grinding and polishing.

The literature contains only Moh's hardness data for cerium oxide abrasives. We report here, for the first time, an actual nanohardness value for individual cerium oxide abrasives. The tests and procedures described here allow for the characterization of the mechanical properties of small particles that is not possible through microindentation without sintering or using samples much larger than those normally used. This allows for the study of abrasives in forms actually used in polishing, so that full characterization of the mechanical properties of polishing materials is now possible. Furthermore, removal experiments using various combinations of magnetic and nonmagnetic abrasive particles and slurry fluid chemistries should give valuable information in the future regarding the removal mechanisms for MRF.



G4979

Figure 82.65 The relative nanohardness values of the particles, glasses, and crystal that have been indented (in air) at 5-mN load on the nanoindenter.



G4980

Figure 82.66  
Particle nanohardness as a function of the sum of carbon and nitrogen present. An expected power law dependence is seen. Similar results are achieved if only nitrogen or carbon is analyzed.

## ACKNOWLEDGMENT

The authors would like to thank Professor John C. Lambropoulos of the Mechanical Engineering Department of the University of Rochester for his assistance. We also acknowledge the contributions of Cindy Barnett and Becky Coppens of the COM and Gail Schlosser and Lisa Cliff of LLE for assistance in preparation of this article; Alexander Maltsev of the LLE and Dennis Van Gee of the COM for assistance in sample preparation, Professor Roger Gans of the Mechanical Engineering Department, Professor James Li of the Materials Science Program at the University of Rochester and Bob Nesin of Micro Abrasives for helpful discussions. Brian McIntyre of the Optics Department at the University of Rochester is acknowledged for his work on the SEM. We would also like to thank Jennifer Murphy, Susan Brandt, Rosa Lee, Caleb Farny, Leslie Gregg, and Dr. Steven Arrasmith for their participation in the project. Dr. Al Friederang of BASF Corporation and Ms. Dana Zagari of Ferro Corporation are thanked for providing many different samples. Support for this work was provided in part by a Department of Education graduate fellowship (GAANN), QED Technologies, LLC, Byelocorp Scientific, Inc, U.S. Army Materiel Command, DARPA (Defense Advanced Research Project Agency), and the National Science Foundation (Grant CMS-9601585).

## REFERENCES

1. D. Golini, S. Jacobs, W. Kordonski, and P. Dumas, in *Advanced Materials for Optics and Precision Structures*, edited by M. A. Ealey, R. A. Paquin, and T. B. Parsonage, Critical Reviews of Optical Science and Technology (SPIE, Bellingham, WA, 1997), Vol. CR67, pp. 251–274.
2. Zygo New View™ 100 White-Light Interferometer, 20× Mirau objective, Zygo Corporation, Middlefield, CT 06455.
3. S. D. Jacobs, W. Kordonski, I. V. Prokhorov, D. Golini, G. R. Gorodkin, and T. D. Strafford, U.S. Patent No. 5,795,212 (18 August 1998).
4. T. S. Izumitani, *Optical Glass*, American Institute of Physics Translation Series (American Institute of Physics, New York, 1986), pp. 92–98.
5. A. Kaller, *Glass Sci. Technol.* **71**, 174 (1998).

6. A. B. Shorey, L. L. Gregg, H. J. Romanofsky, S. R. Arrasmith, I. Kozhinova, J. Hubregsen, and S. D. Jacobs, in *Optical Manufacturing and Testing III*, edited by H. Stahl (SPIE, Bellingham, WA, 1999), Vol. 3782, pp. 101–111.
7. R. Steinitz, *Metals & Alloys* **17**, 1183 (1943).
8. Nano IIS Nanoindenter and accompanying operating instructions, Version 2.2, p. 7 (1996), Nano Instruments, Oak Ridge, TN 37830.
9. W. C. Oliver and G. M. Pharr, *J. Mater. Res.* **7**, 1564 (1992).
10. G. M. Pharr and W. C. Oliver, *Mater. Res. Bull.* **17**, 28 (1992).
11. J. C. Hay and G. M. Pharr, in *Thin-Films—Stresses and Mechanical Properties VII*, edited by R. C. Cammarata *et al.*, Mat. Res. Soc. Symp. Proc. Vol. 505 (Materials Research Society, Warrendale, PA, 1998), pp. 65–70.
12. 16- to 18- $\mu\text{m}$  wire mesh sieve, Newark Wire Cloth Company, Newark, NJ 07104.
13.  $2.54 \times 1.27 \times 0.64$ -cm samples made from material provided by Schott Glass Technologies, Duryea, PA 18642.
14. Samarium-Cobalt magnets ( $2.54 \times 2.54 \times 1.08$  cm) purchased from the McMaster-Carr Supply Company, Elmhurst, IL 60126. They supply a field intensity of about 2.5 kG in a direction perpendicular to the surface of the magnet.
15. 2-Ton® Clear Epoxy from ITW Devcon, Danvers, MA 01923.
16. Kapton® is a polyamide film provided by DuPont®. We used type HV300. Teflon® films have also been used.
17. Y. Grasselli, G. Bossis, and E. Lemaire, *Prog. Colloid Polym. Sci.* **93**, 175 (1993).
18. Microgrit Micro Abrasives Corporation, Westfield, MA 01086-0669.
19. R. E. Parks, R. E. Sumner, and J. T. Appels, *Opt. Eng.* **16**, 332 (1977).
20. Load was measured by the I-Scan pressure measurement system from Tekscan, Inc., Boston, MA 02127. We used a 5051 pressure film with a maximum allowable load of 345 kPa (50 psi).
21. J. H. Rhodes, # FJ0202, Universal Photonics, Inc., Hicksville, NY 11801-1014.
22. Olympus VANOX-TAH-2 optical microscope, No. 501008, Olympus Optical Co. Ltd., Tokyo, Japan.
23. Measurements were made using the Form Talysurf® mechanical profilometer, Taylor Hobson Ltd., Leicester, LE4 9JQ, UK. The device has a 60-mm stylus arm length and a 2- $\mu\text{m}$ -radius tip.
24. Buehler Ltd., Lake Bluff, IL 60044-1699.
25. LEO 982 field emission SEM (LEO is a Zeiss-Leica company).
26. *Metals Test Methods and Analytical Procedures*, Annual Book of ASTM Standards (American Society for Testing and Materials, West Conshohocken, PA, 1999), Vol. 3.01, p. 393.

27. I. N. Sneddon, *Fourier Transforms*, 1st ed. (McGraw-Hill, New York, 1951), Sec. 52.5.
28. A. Krell, P. Blank, E. Wagner, and G. Bartels, *J. Am. Ceram. Soc.* **79**, 763 (1996).
29. J. C. Lambropoulos, T. Fang, P. D. Funkenbusch, S. D. Jacobs, M. J. Cumbo, and D. Golini, *Appl. Opt.* **35**, 4448 (1996).
30. T. Fang, "Near-Surface Mechanical Properties of Optical Materials in Deterministic Microgrinding," Ph.D. thesis, University of Rochester, 1997, Chap. 3.
31. K. Sangwal *et al.*, *J. Mater. Res.* **14**, 3973 (1999).
32. F. Dahmani, J. C. Lambropoulos, A. W. Schmid, S. J. Burns, and C. Pratt, *J. Mater. Sci.* **33**, 4677 (1998).
33. J. H. Westbrook, *Phys. Chem. Glasses* **1**, 32 (1960).
34. D. Tabor, *Proc. Phys. Soc., Sec. B* **67**, 249 (1954).
35. W. D. Callister, *Materials Science and Engineering*, 2nd ed. (Wiley, New York, 1991), pp. 131-141.
36. S. Ramarajan *et al.*, *Surf. Eng.* **15**, 324 (1999).
37. L. B. Pfeil, *Symposium on Powder Metallurgy*, 47, The Iron and Steel Institute, Grosvenor Gardens, London, Special Report No. 38 (1947).
38. F. L. Ebenhoech, *Prog. Powder Metall.* **42**, 133 (1986).
39. J. E. Japka, *J. Met.* **40**, 18 (1988).
40. G. Boehm, *Fachber. Huettenprax. Metallweiterverarb.* **20**, 146 (1982).
41. K. Okuyama and Y. Kousaka, in *Powder Technology Handbook*, edited by K. Iinoya, K. Gotoh, and K. Higashitani (Marcel Dekker, New York, 1991), pp. 57-61.
42. G. K. Nathan and W. J. D. Jones, *Proc. Instn. Mech. Engrs.* **181**, 215 (1966-67).
43. J. N. Brecker, R. Komanduri, and M. C. Shaw, *Ann. CIRP* **22**, 219 (1973).
44. K. Nassau, *Lapidary J.* **35**, 1194 (1981).
45. C. A. West, *Can. Chem. Process Inds.* **28**, 3 (1944).
46. Corning 7940, Corning, Inc., Corning, NY 14831-0002.
47. LHG8, Hoya Corporation USA, San Jose, CA 95131.
48. KDP provided by Cleveland Crystals, Inc. (CCI), Cleveland, OH 44110. Indents were done on a fractured surface (Type-II cut).
49. BASF Corporation, Mt. Olive, NJ 07828-1234.
50. ISP International, Wayne, NJ 07470.
51. Novamet, Wyckoff, NJ 07481.
52. Personal communication with Dr. Al Friederang, BASF Corporation, 28 July 1998.
53. Exolon-Esk Company, Tonawanda, NY 14151-0590.
54. Microabrasives Corporation, Westfield, MA 01085.
55. Zirconia I, batch #1502792, courtesy of Saint Gobain/Norton Industrial Ceramics Corporation, Worcester, MA 15136.
56. 1.0- $\mu$ m C, alumina polishing compound, Praxair Surface Technologies, Indianapolis, IN 46222-3274.
57. Transelco Division of Ferro Corporation, Penn Yan, NY 14527.
58. C. R. Brooks, *Heat Treatment of Ferrous Alloys* (Hemisphere, Washington, 1979).
59. T. Fujihana *et al.*, *Surf. Coat. Technol.* **51**, 19 (1992).
60. J. D. Verhoeven, *Fundamentals of Physical Metallurgy* (Wiley, New York, 1975), Chaps. 11 and 14.
61. Personal communication with Prof. James C. Li, Materials Science Program, University of Rochester, 1998.
62. Personal communication with Dr. James Knapp, Praxair Surface Technologies, 1999.
63. Personal communication with Ms. Dana Zagari, Transelco Division of Ferro Corporation, 1999.

---

## Publications and Conference Presentations

---

### Publications

---

R. Adam, M. Currie, C. Williams, R. Sobolewski, O. Harnack, and M. Darula, "Direct Observation of Subpicosecond Single-Flux-Quantum Generation in Pulse-Driven Y-Ba-Cu-O Josephson Junctions," *Appl. Phys. Lett.* **76**, 469 (2000).

S. H. Chen, R. J. Jin, D. Katsis, J. C. Mastrangelo, S. Papernov, and A. W. Schmid, "Photorecimization Broadening of Selective Reflection and Polarization Band of Glassy Chiral-Nematic Films," *Liq. Cryst.* **27**, 201 (2000).

J. P. Knauer, R. Betti, D. K. Bradley, T. R. Boehly, T. J. B. Collins, V. N. Goncharov, P. W. McKenty, D. D. Meyerhofer, V. A. Smalyuk, C. P. Verdon, S. G. Glendinning, D. H. Kalantar, and R. G. Watt, "Single-Mode Rayleigh-Taylor Growth-Rate Measurements on the OMEGA Laser System," *Phys. Plasmas* **7**, 338 (2000).

F. J. Marshall, J. A. Delettrez, V. Yu. Glebov, R. P. J. Town, B. Yaakobi, R. L. Kremens, and M. Cable, "Direct-Drive, Hollow-Shell Implosion Studies on the 60-Beam, UV OMEGA Laser System," *Phys. Plasma* **7**, 1006 (2000).

R. L. McCrory, J. M. Soures, A. Babushkin, R. E. Bahr, R. Betti, T. R. Boehly, R. Boni, D. K. Bradley, T. J. B. Collins, R. S. Craxton, J. A. Delettrez, W. R. Donaldson, R. Epstein,

V. Yu. Glebov, V. N. Goncharov, R. Q. Gram, D. R. Harding, D. G. Hicks, B. Hughes, P. A. Jaanimagi, T. J. Kessler, J. P. Knauer, C. K. Li, S. J. Loucks, F. J. Marshall, P. W. McKenty, D. D. Meyerhofer, A. V. Okishev, S. Padalino, R. D. Petrasso, P. B. Radha, S. P. Regan, F. H. Séguin, W. Seka, R. W. Short, A. Simon, M. D. Skeldon, S. Skupsky, C. Stoeckl, R. P. J. Town, M. D. Wittman, B. Yaakobi, and J. D. Zuegel, "Recent Advances in Direct-Drive ICF Target Physics at the Laboratory for Laser Energetics," in *Fusion Energy 1998* (IAEA, Vienna, 1999), Vol. I, pp. 167-176.

A. V. Okishev, "The Oldest Higher-Educational Optical Institution in Russia Turns 100," *Optics & Photonics News*, March 2000, 17.

A. V. Okishev, M. D. Skeldon, R. L. Keck, and W. Seka, "All-Solid-State Optical Pulse Shaper for the OMEGA Laser Fusion Facility," in *Advanced Solid-State Lasers*, OSA Technical Digest (Optical Society of America, Washington, DC, 2000), pp. 30-32.

D. L. Tubbs, C. W. Barnes, J. B. Beck, N. M. Hoffman, J. A. Oertel, R. G. Watt, T. Boehly, D. Bradley, P. Jaanimagi, and J. Knauer, "Cylindrical Implosion Experiments Using Laser Direct Drive," *Phys. Plasmas* **6**, 2095 (1999).

---

### Forthcoming Publications

---

E. L. Alfonso, I. Anteby, and D. R. Harding, "Temperature Profiles and  $\ell = 1$  Nonuniformity within Cryogenic ICF Targets," to be published in *Fusion Technology*.

S. R. Arrasmith, S. D. Jacobs, I. A. Kozhinova, A. B. Shorey, D. Golini, W. I. Kordonski, S. Hogan, and P. Dumas, "Development and Characterization of Magnetorheological Fluids for Optical Finishing," to be published in the *Proceedings of Fine Powder Processing '99*, University Park, PA, 20-22 September 1999.

R. Betti and J. P. Freidberg, "Low- $\beta$ , Magnetohydrodynamic Tokamak Equilibria with Poloidal Transonic Flow," to be published in *Physical Review Letters*.

R. Betti and J. P. Freidberg, "Radial Discontinuities in Tokamak MHD Equilibria with Poloidal Flow," to be published in *Physics of Plasmas*.

T. R. Boehly, A. Babushkin, D. K. Bradley, R. S. Craxton, J. A. Delettrez, R. Epstein, T. J. Kessler, J. P. Knauer, R. L. McCrory,

P. W. McKenty, D. D. Meyerhofer, S. Regan, W. Seka, S. Skupsky, V. A. Smalyuk, R. P. J. Town, and B. Yaakobi, "Laser-Uniformity and Hydrodynamic-Stability Experiments at the OMEGA Laser Facility," to be published in *Laser and Particle Beams*.

D. P. Butler, Z. Celik-Butler, and R. Sobolewski, "Y-Ba-Cu-O as an Infrared Radiation Sensing Material," to be published in the *Handbook of Advanced Electronic and Photonic Materials* (Academic Press, NY).

J. L. Chaloupka and D. D. Meyerhofer, "Characterization of a Tunable Single-Beam Ponderomotive-Optical Trap," to be published in the *Journal of the Optical Society of America B*.

T. J. B. Collins, H. L. Helfer, and H. M. VanHorn, "Oscillations of Accretion Disks and Boundary Layers in Cataclysmic Variables: I. Unperturbed, Steady-Flow Models," to be published in *Astrophysical Journal*.

T. J. B. Collins, H. L. Helfer, and H. M. VanHorn, "Oscillations of Accretion Disks and Boundary Layers in Cataclysmic Variables: II. A Local, Linear Stability Analysis of Accretion Disk Boundary Layers," to be published in *Astrophysical Journal*.

F. Dahmani, A. W. Schmid, J. C. Lambropoulos, and S. J. Burns, "Lifetime Prediction of Laser-Pre-cracked Fused Silica Subjected to Subsequent Cyclic Laser Pulses," to be published in the *Journal of Materials Science*.

F.-Y. Fan, J. C. Mastrangelo, D. Katsis, and S.-H. Chen, "Novel Glass-Forming Liquid Crystals: V. Nematic and Chiral-Nematic Systems with an Elevated Glass Transition Temperature," to be published in *Liquid Crystals*.

V. N. Goncharov, S. Skupsky, P. W. McKenty, J. A. Delettrez, R. P. J. Town, and C. Cherfils-Cl  rouin, "Stability Analysis of Directly Driven OMEGA and NIF Capsules," to be published in the *Proceedings of the 1999 Inertial Fusion Sciences and Applications Conference, Bordeaux, France, 12–17 September 1999*.

V. N. Goncharov, S. Skupsky, P. W. McKenty, R. P. J. Town, T. R. Boehly, D. D. Meyerhofer, and O. V. Gotchev, "A Model of Laser Imprinting," to be published in *Physics of Plasmas* (invited).

S. R. Gorodkin, W. I. Kordonski, E. V. Medvedeva, Z. A. Novikova, A. B. Shorey, and S. D. Jacobs, "A Method and

Device for Measurement of a Sedimentation Constant of Magnetorheological (MR) Fluids," to be published in the *Review of Scientific Instruments*.

K. Green and R. Sobolewski, "Extending the S-Parameter Approach to Linear Time-Varying Microwave Devices: Part I. Analysis," to be published in *IEEE Microwave Theory and Techniques*.

M. J. Guardalben and N. Jain, "Phase-Shift Error Due to Molecular Alignment Distortions in the Liquid Crystal Point-Diffraction Interferometer," to be published in *Optics Letters*.

K. S. Il'in, M. Lindgren, M. Currie, A. D. Semenov, G. N. Gol'tsman, R. Sobolewski, S. I. Cherednichenko, and E. M. Gershenzon, "Picosecond Hot-Electron Energy Relaxation in NbN Superconducting Photodetectors," to be published in *Applied Physics Letters*.

P. A. Jaanimagi, R. Boni, and R. L. Keck, "Neutron-Induced Background in CCD Detectors," to be published in the *Review of Scientific Instruments*.

S. D. Jacobs and A. B. Shorey, "Magnetorheological Finishing: New Fluids for New Materials," to be published in the *Optical Fabrication and Testing Technical Digest (OSA)*.

I. A. Kozhinova, S. D. Jacobs, S. R. Arrasmith, and L. L. Gregg, "Corrosion in Aqueous Cerium Oxide Magnetorheological Fluids," to be published in the *Optical Fabrication and Testing Technical Digest (OSA)*.

C. K. Li, D. G. Hicks, F. H. S  guin, J. A. Frenje, R. D. Petrasso, J. M. Soures, P. B. Radha, V. Yu. Glebov, C. Stoeckl, J. P. Knauer, R. Kremens, F. J. Marshall, D. D. Meyerhofer, S. Skupsky, S. Roberts, C. Sorce, T. C. Sangster, T. W. Phillips, M. D. Cable, and R. J. Leeper, "D-<sup>3</sup>He Proton Spectra for Diagnosing Shell  $\rho R$  and Fuel  $T_i$  of Imploded Capsules on OMEGA," to be published in *Physics of Plasmas*.

F. J. Marshall, J. A. Delettrez, R. Epstein, V. Yu. Glebov, D. R. Harding, P. W. McKenty, D. D. Meyerhofer, P. B. Radha, W. Seka, S. Skupsky, V. A. Smalyuk, J. M. Soures, C. Stoeckl, R. P. J. Town, B. Yaakobi, C. K. Li, F. H. S  guin, D. G. Hicks, and R. D. Petrasso, "Direct-Drive, High-Convergence-Ratio Implosion Studies on the OMEGA Laser System," to be published in the *May 2000 Special Issue of Physics of Plasmas*.

- R. L. McCrory, R. E. Bahr, T. R. Boehly, T. J. B. Collins, R. S. Craxton, J. A. Delettrez, W. R. Donaldson, R. Epstein, V. N. Goncharov, R. Q. Gram, D. R. Harding, P. A. Jaanimagi, R. L. Keck, J. P. Knauer, S. J. Loucks, F. J. Marshall, P. W. McKenty, D. D. Meyerhofer, S. F. B. Morse, O. V. Gotchev, P. B. Radha, S. Regan, W. Seka, S. Skupsky, V. A. Smalyuk, J. M. Soures, C. Stoeckl, R. P. J. Town, M. D. Wittman, B. Yaakobi, J. D. Zuegel, R. D. Petrasso, D. G. Hicks, and C. K. Li, "OMEGA Experiments and Preparation for Direct-Drive Ignition on the National Ignition Facility," to be published in the Proceedings of the 1999 Inertial Fusion Sciences and Applications Conference, Bordeaux, France, 12–17 September 1999.
- P. W. McKenty, M. D. Wittman, and V. N. Goncharov, "Characterization of Thick Cryogenic Fuel Layers Using Convergent-Beam Interferometry: A Numerical Investigation," to be published in the Journal of Applied Physics.
- P. B. Radha, S. Skupsky, R. D. Petrasso, and J. M. Soures, "A Novel Charged-Particle Diagnostic for Compression in ICF Targets," to be published in Physics of Plasmas.
- S. P. Regan, J. A. Marozas, J. H. Kelly, T. R. Boehly, W. R. Donaldson, P. A. Jaanimagi, R. L. Keck, T. J. Kessler, D. D. Meyerhofer, W. Seka, S. Skupsky, and V. A. Smalyuk, "Experimental Investigation of Smoothing by Spectral Dispersion," to be published in the Journal of the Optical Society of America B.
- J. D. Schnittman and R. S. Craxton, "Three-Dimensional Modeling of Capsule Implosions in OMEGA Tetrahedral Hohlräume," to be published in Physics of Plasmas.
- F. H. Séguin, C. K. Li, D. G. Hicks, J. A. Frenje, R. D. Petrasso, J. M. Soures, V. Yu. Glebov, C. Stoeckl, P. B. Radha, D. D. Meyerhofer, S. Roberts, C. Sorce, T. C. Sangster, and M. D. Cable, "Diagnostic Use of Secondary D-<sup>3</sup>He Proton Spectra for D-D OMEGA Targets," to be published in Physics of Plasmas.
- A. B. Shorey and S. D. Jacobs, "Nanohardness of Abrasive Particles Used in Magnetorheological Finishing (MRF)," to be published in Optical Fabrication and Testing Technical Digest (OSA).
- A. B. Shorey, K. M. Kwong, K. M. Johnson, and S. D. Jacobs, "Nanoindentation Hardness of Particles Used in Magnetorheological Finishing (MRF)," to be published in Applied Optics.
- R. W. Short, "Stability of Self-Focused Filaments in Laser-Produced Plasmas," to be published in Physical Review Letters.
- M. D. Skeldon, "A High-Bandwidth Electrical-Waveform Generator Based on an Aperture-Coupled Stripline," to be published in the Review of Scientific Instruments.
- M. D. Skeldon, "An Optical Pulse-Shaping System Based on an Electro-Optic Modulator Driven by an Aperture-Coupled-Stripline Electrical Waveform Generator," to be published in Optics Letters.
- D. J. Smith, J. A. Warner, N. E. LeBarron, T. J. Kessler, and S. LaDelia, "The Development of Ion-Etched Phase Plates," to be published in Applied Optics.
- R. Sobolewski, "Time-Resolved Nonequilibrium Phenomena in High-Temperature Superconductors," to be published in the Proceedings of the International Workshop on Superconductivity, Magneto-Resistive Materials, and Strongly Correlated Quantum Systems, Hanoi, Vietnam, June 1999 (invited).
- F.-Y. Tsai, E. L. Alfonso, S.-H. Chen, and D. R. Harding, "Mechanical Properties and Gas Permeability of Polyimide Shells Fabricated by the Vapor Deposition Method," to be published in Fusion Technology.
- B. Yaakobi, V. A. Smalyuk, J. A. Delettrez, F. J. Marshall, D. D. Meyerhofer, and W. Seka, "Measurement of  $\rho\Delta R$  Modulation of Laser-Imploded Shells through K-Edge Imaging," to be published in Physics of Plasmas.
- B. Yaakobi, V. A. Smalyuk, J. A. Delettrez, R. P. J. Town, F. J. Marshall, V. Yu. Glebov, R. D. Petrasso, J. M. Soures, D. D. Meyerhofer, and W. Seka, "Spherical Implosion Experiments on OMEGA: Measurements of the Cold, Compressed Shell," to be published in the Proceedings of the 1999 Inertial Fusion Sciences and Applications Conference, Bordeaux, France, 12–17 September 1999.
- B. Yaakobi, C. Stoeckl, T. R. Boehly, D. D. Meyerhofer, and W. Seka, "Measurement of Preheat Due to Fast Electrons in Laser Implosions," to be published in Physics of Plasmas.

---

## Conference Presentations

---

J. D. Schnittman and R. S. Craxton, "Three-Dimensional Modeling of Capsule Implosions in OMEGA Tetrahedral Hohlräume," Israel Plasma Science Technology Association, Beer Sheva, Israel, 9 February 2000.

---

A. V. Okishev, M. D. Skeldon, R. L. Keck, and W. Seka, "All-Solid-State Optical Pulse Shaper for the OMEGA Laser Fusion Facility," Advanced Solid-State Lasers 15th Topical Meeting, Davos, Switzerland, 13–16 February 2000.

---

A. B. Shorey, K. M. Kwong, and S. D. Jacobs, "Revealing Hardness Variations in Optical Polishing Abrasives," MTS Nano Instrument Users' Meeting, Albany, NY, 22 February 2000.

The following presentations were made at the 12th APS Topical Conference on Atomic Processes in Plasmas, Reno, NV, 19–23 March 2000:

S. P. Regan, J. A. Delettrez, B. Yaakobi, D. K. Bradley, R. E. Bahr, M. Millecchia, D. D. Meyerhofer, and W. Seka, "Spectroscopic Analysis of Electron Temperature in Laser-Driven Burnthrough Experiments."

V. A. Smalyuk, B. Yaakobi, F. J. Marshall, and D. D. Meyerhofer, "X-Ray Spectroscopic Measurements of Areal Density and Modulations in Areal Density of Cold Compressed Shells in Implosion Experiments on OMEGA."

---

J. P. Knauer, T. J. B. Collins, A. Frank, and E. Blackman, "Generation of Collimated Flows by Intense Irradiation with Applications to Astrophysical Phenomena," 3rd International Conference on Laboratory Astrophysics with Intense Lasers, Rice University, Houston, TX, 30 March–1 April 2000.

UNIVERSITY OF  
ROCHESTER